PREDICTING NANOSTRUCTURES AND PHOTONIC PROPERTIES OF BLOCK COPOLYMER DERIVED MATERIALS

A Dissertation
Presented to the Faculty of the Graduate School
of Cornell University
In Partial Fulfillment of the Requirements for the Degree of
Doctor of Philosophy

by
Kahyun Hur
January 2013

PREDICTING NANOSTRUCTURES AND PHOTONIC PROPERTIES OF BLOCK COPOLYMER DERIVED MATERIALS

Kahyun Hur, Ph.D.

Cornell University 2013

Bottom up type block copolymer (BCP) self-assembly and co-assembly are expected to provide facile routes to nanostructured materials for various, e.g. energy related and photonics, applications. In many of these experimental systems, chemical building blocks are complex organic/inorganic hybrid molecules such as ligand-stabilized NPs. In particular, for complex multicomponent systems involving assembly of nanoparticles (NPs) and macromolecules, limited understanding of the role of such key factors has severely hampered progress.

Despite progress in simulations and theories, structure prediction of self-assembled materials beyond simple model systems remain challenging. To this end, an efficient theoretical framework that unifies polymer field theory and density functional theory into a single method was presented in order to incorporate complex molecular details with key physical interactions. The method harnesses the efficiency of self-consistent field theories and the flexibility of density functional theory and a generalized propagator method enabling the description of different types of components and interactions, i.e. it allows a level of complexity usually reserved to more costly molecular simulation treatments. Utilizing the method, design criteria for controlling a range of NP based nanomaterial structures were studied.

As an application of BCP derived materials, their photonic properties were studied. Metamaterials, engineered metallic materials, offer new functionalities such as super-resolution imaging and cloaking. Despite considerable progress, finding efficient pathways towards 3-dimensionally isotropic metamaterials remains challenging thus hampering their practical applications. To this end, the photonic properties of 3-dimensionally isotropic metallic nanomaterials with the cubic double gyroid and the alternating gyroid morphologies were calculated. These materials can be obtained by block copolymer self-assembly with a unit cell significantly smaller than the free space wavelength of visible light. For double gyroid metamaterials, the materials parameters and design principles for negative-refractive index materials in the visible and near infrared spectrum were specifically identified.

Lastly surface plasmon resonance phenomena of novel metamaterials were investigated. Especially, 3-dimensionally continuous metamaterials with the diamond cubic structure display both negative refractive index as well as complete surface plasmon band gaps in 3-dimensions. Results suggest further design criteria and in-depth understandings for metamaterials exhibiting unusual optical properties.

BIOGRAPHICAL SKETCH

Kahyun Hur was born on June 23rd, 1978 in Seoul, Korea to Joong Gi Hur and Bok Soon Kim. He has two older sisters, Joo Yeon and Geum Yeon.

In 1985, he joined Sang Myung elementary school, a private school in Seoul, and spent four and half years before moving to Sin Ga elementary school in Seoul due to his family's moving. In 1991, he joined Seok Chon middle school in Seoul and spent three years. In 1994, he joined Joong San high school in Seoul and chose the division of science and engineering.

In 1997, he started school in the Division of Natural Sciences at Seoul National University and decided to major in Chemistry two years later. During the period he enjoyed underwater exploration in a SCUBA (self contained underwater breathing apparantus) diving team at Seoul National University. In his senior year, he met his former advisor, Prof. Do Y. Yoon, and decided to join his group for studying polymer physics.

In 2002, he started the Master of Science degree program in Chemistry Department at Seoul National University. His research topic was molecular dynamics study on ring polymer dynamics.

In 2004, he joined Iljin Display as a research engineer instead of two-year mandatory military service. He developed novel high temperature polycrystalline silicon liquid crystal display panels for various projector applications. During the period he thought that materials research is one of the most important researches for many device applications and decided to study materials for his PhD.

In August 2007, he retired from the engineering job in Iljin Display and was preparing applications to PhD programs of US universities. Meanwhile he came back to Prof. Do Y. Yoon's group as a visiting scientist for continuing his MS research. He accepted an offer to attend graduate school in the Department of Materials Science and

Engineering at Cornell University and joined Wiesner group in 2008 for studying block copolymer. In 2011, he passed his A exam and continued his research for completion of his PhD.

To my family

ACKNOWLEDGMENTS

There are many persons that I would like to thank for their support. First I would like to thank my advisors, Prof. Uli Wiesner, Prof. Fernando A. Escobedo and Prof. Richard G. Hennig. Uli has been a great mentor to guide me in a right direction for my research and career. I cannot thank him enough for his support during my PhD. Fernando and Richard have been great advisors and very supportive.

Next I would like to thank my research group members for fruitful discussions or just being there. These include Chris Orilall, Hitesh Arora, Morgan Stefik, Hiroaki Sai, Zihui (Cathy) Li, Michele Chavis, Srikant Iyer, Rachel Dorin, Juho Song, Kwan Wee Tan, Yao Sun, Jenni Drewes, Christina Cowman, Kai Ma, Spencer Robbins, Tom Swisher, Yibei Gu, Joerg Werner and Xian Shi.

Credit for those who contributed monetary funds for the research found in this dissertation is given at the end of the publications used as the basis of each chapter.

TABLE OF CONTENTS

Biological Sketch.......iii

Dedication.......v

Acknowledgements.......vi

Table of Contents.......vii

List of Figures.......ix

List of Tables.......xii

Chapter 1 - Introduction.......1

References.......13

Chapter 2 - Mesoscopic Structure Prediction of Nanoparticle Assembly and Co-Assembly : Theoretical foundation.......16

References.......61

Chapter 3 - Predicting Chiral Nanostructures, Lattices and Superlattices in Complex Multi-Component Nanoparticle Self-Assembly.......65

Appendix A.......83

References.......89

Chapter 4 - Three-dimensionally Isotropic Negative Refractive Index Materials from Block Copolymer Self-assembled Chiral Gyroid Networks.......92

Appendix B.......108

References 115

Chapter 5 - Complete surface plasmon band gaps in 3-dimensional hierarchical metamaterials 122

Appendix C.. 138

References 143

LIST OF FIGURES

Figure 1.1 Theoretical phase-diagram of di-block copolymers and schematics of predicted morphologies 8

Figure 1.2 Various computational approaches and computational budgets of simulated system size or timescale........ 9

Figure 1.3 Novel optical applications initiated by recent advances of nano-photonics 10

Figure 1.4 Plasmons are an oscillation of free electron density in a metal 11

Figure 1.5 Surface plasmon resonance phenomena of nanoscale metallic materials. 12

Figure 2.1 The general schematic procedure and key equations of the present approach 54

Figure 2.2 Multi-component molecule representations with the linear configuration for flexible monomers and HS particles with flexible molecules 55

Figure 2.3 Comparison of particle density profiles in the lamellar morphology of BCP/NP self-assembly varying the excess HS free energy functional ... 56

Figure 2.4 Density profiles of positively charged and negatively charged HS particles as a function of distance from a positively charged flat wall with different surface charge densities 57

Figure 2.5 Density profiles of NPs and local volume fractions of BCPs for self-assembly of two chemically distinct HS particles connected by a homopolymer molecule within BCPs ... 58

Figure 2.6 Comparison of the bead-spring model and SCFT ... 59

Figure 2.7 Self-assembly of BCPs, NPs with charged ligands, and CAs, illustrating the effect of NP Coulomb repulsions on enhancing the regular dispersion of NPs ... 60

Figure 3.1 The single molecular partition functions of simulated species ... 78

Figure 3.2 Poly(isoprene-b-styrene-b-ethylene oxide) (PI-b-PS-b-PEO) / ligand-stabilize NP composite forms alternating Gyroid morphology ... 79

Figure 3.3 Coulomb interactions induce lattice formation of NPs. a, Green color represents regions occupied by NPs ... 80

Figure 3.4 Coulomb interactions between NPs control lamellar morphology and above a critical Coulomb interaction strength induce superlattice formation of NPs within one dimensional (lamellar) BCP lattices ... 81

Figure 4.1 Schematic routes to 3-dimensionally co-continuous metamaterials with cubic symmetry and expected optical behavior ... 103

Figure 4.2 Results of band structure calculations using an eigensolver approach for D-GYR metamaterials made of a Drude metal and the plasma frequency of gold ... 104

Figure 4.3 Results of finite element-based calculations using COMSOL ... 106

Figure 4.4 The photonic band structure of a hollow D-GYR metamaterial shows a lower onset frequency of the negative refraction than D-GYR metamaterials 107

Figure 5.1 Photonic crystal and metamaterials with 3-dimensionally continuous diamond cubic structure varying substructure and their photonic band structures 132

Figure 5.2 Energy flux of positive and negative refraction bands for the diamond cubic metamaterial with double gyroid substructures........................... 133

Figure 5.3 Magnetic field distributions of the acoustic band in the metamaterial and the photonic crystal with the diamond cubic structure show distinct field strengths 134

Figure 5.4 Photonic band structures of diamond cubic photonic crystals and hierarchical diamond cubic metamaterials with a disconnected double gyroid substructure and connected majority of double gyroid substructure 135

Figure 5.5 Photonic band structure and losses of diamond cubic metamaterial with a coaxial geometry for gold 136

Figure 5.6 Photonic band structures of the photonic crystal and the hierarchical metamaterial with alternating gyroid structure 137

LIST OF TABLES

Table 2.1 Flory-Huggins parameters for the simulation of HS particle self-assembly within BCPs 52

Table 2.2 Flory-Huggins parameters for the simulation of self-assembly of two chemically distinct HS particles connected by a homopolymer molecule within BCPs 52

Table 2.3 Flory-Huggins parameters for the self-assembly of BCPs and NPs with charged ligands 53

CHAPTER 1

INTRODUCTION

Materials research is one of the key scientific topics in modern science due to its growing importance for improving performances of various, e.g. energy related, biological or photonic, devices. Device performance is highly correlated with materials properties such as durability, conductivity, band gap and permittivity. Since materials properties are dependent on composition and structure, controlling the nanostructure of novel materials can overcome known limitations of existing devices such as solar cells. Much effort has been devoted during the last decade to the control of nanostructures but adaptation of research results into real devices still remains challenging. One of the most promising techniques for nanostructure control is block copolymer self-assembly. This bottom-up approach techniques allows molecular architecture to be used to control composition and nanostructure in cost-effective ways. In this thesis structure prediction of block copolymer derived materials and their photonic properties are detailed. In Chapters 2 and 3, a novel theoretical approach that enables structure prediction of materials self-assembled from block copolymers as structure-directing agents is developed and examples of novel nanoparticle-block copolymer nanostructures predicted by the theory are shown. In Chapter 4 and 5, photonic/plasmonic properties of block copolymer derived metallic materials are studied theoretically thereby developing an in-depth understanding of their unusual optical behavior.

1.1. Block copolymers as structure-directing agents

1.1.1. Block copolymer self-assemblies and co-assemblies

Block copolymer self-assembly provides a unique platform enabling control morphologies down to the nanoscale regime [1]. The typical length scale of block copolymer phase separation is tens of nanometers, which is useful for various device applications. Moreover, morphologies including 3-dimensionally continuous structures can be obtained from tuning the block composition as shown in Fig. 1.1. However, block copolymers themselves usually have no functions or robustness for device applications, e.g. semi-conducting materials for generating exitons in solar cells. In order to add functionality to nanostructured materials derived from block copolymer self-assembly, additional treatments such as selective etching and functional material deposition are thus required. As an alternative, one can synthesize a material through block copolymer co-assembly, where other functional materials like functional nanoparticles or metal oxides are structure directed by the block copolymers. The co-assembly strategy has been successfully applied to platinum nanoparticles [2]. The biggest advantage of this approach is that it provides a modular pathway to multicomponent materials synthesis with a one pot strategy. Combining various functional materials with block copolymers, an unlimited variation of functional materials can be obtained with simultaneous nanostructure control. Experimentally a variety of system parameters such as nanoparticle ligand chemical structure, polymer length, and particle size affect the final nanostructure. Huge parameter space is one of the biggest hurdles to the effective use of co-assembly strategies. In order to explore this parameter space and provide guidance for materials design, reliable theoretical and simulation studies of co-assembly systems are desirable that could elucidate critical factors in the assembly and predict final structures quantitatively.

1.1.2. Structure prediction

Depending on the specific materials system, various simulation methodologies exist as shown in Fig. 1.2. All of the approaches have advantages and disadvantages. Atomistic or particle-based modeling such as molecular dynamics and Monte Carlo simulations [4] can readily incorporate different molecular details but are computationally more expensive than theoretical approaches; furthermore, they require specialized methods to measure or impose chemical potentials and an analysis of finite system-size effects to ensure that structures are obtained at thermodynamic equilibrium (e.g., some morphological features can be frustrated by a lack of geometric commensurability with the box dimensions) [5]. Alternatively, the morphologies of block copoolymer self-assembly have been successfully studied and predicted by self-consistent field theory (SCFT) [6], a field theoretic description of chemical fields exploiting the mean-field approximation. The SCFT approach is very efficient and powerful, but the conventional SCFT approach is not a simulation approach that can incorporate various components with complex molecular structure like ligand stabilized nanoparticles due to its inability to describe all atomistic interactions from hard particle to long-range interactions. To overcome these limitations, in this thesis a new theoretical approach is suggested exploiting advantages of both, theoretical approaches (efficiency) and atomistic simulations (molecular details). The approach unifies density functional theory and SCFT and enables efficient simulations of complex molecular systems, usually reserved to more expensive atomistic simulations. In Chapter 2, the theoretical foundation of the approach is introduced and benchmarked with existing computation results. Chapter 3 mainly demonstrates the applications of the theory to complex molecular systems predicting known and unknown nanostructures.

1.2. Nanophotonics applications of block copolymer derived materials

1.2.1. Plasmonics and metamaterials

Explosive growth of *nano-photonics* research is transforming our understanding of photonic applications and stimulating work in various scientific communities ranging from physical sciences to chemistry and biology. Light is an excellent medium for imaging and signal transfer, but has a fundamental limitation for miniaturization due to the 'diffraction limit' of light [8]. Recent advances of nano-photonics are moving various photonic applications to sub-diffraction-limited length-scales. Some novel research areas of nano-photonics are shown in Fig. 1.3 such as metamaterials and plasmonics. A *metamaterial* is an engineered material that exhibits unusual optical phenomena that may not be found in nature. Metamaterials are usually made of structured metals so as to utilize unique properties of this materials class (see the examples of metamaterials in Fig. 1.3a and b). One of the unusual phenomena is the negative refractive index of a material, which has attracted much attention due to the potential of unlimited resolution imaging [9]. In a similar context, utilizing metamaterial one can make an invisibility cloak to hide any object inside of the cloak (see Fig. 1c and invisibility cloaks in '*Harry Potter*' movie series) [10]. Plasmonics is a scientific subject that treats interactions between light and nano-scale metallic materials. The applications of plasmonic materials, *i.e.* nano-scale metallic materials, to therapeutics [11] and solar cells [12] are being extensively studied.

All of these unusual phenomena originate from '*plasmon*' motions, where the suffix '*-on*' respresents its bosonic character. Plasmon is an oscillation of free electron density in a metal (see Fig. 1.4). Although the name '*plasmon*' implies that it is a quantum mechanical object, it is a classical one described by Maxwell's equations [13]. While the optical behavior of a plasmon has similarities with that of a photon, there are fundamental differences between the two. First of all, the wavelength of a plasmon can be much smaller than that of a photon at the same frequency (note that $\lambda=h/2\pi p$ and the momentum, p, of a moving electron is usually much bigger than the value of a photon). In order to generate optical modulations dielectric material usually has to have a comparable lattice dimension to the wavelength of a photon, *e.g.* photonic crystals [14]. Plasmonic materials barely have such limitations leading to manipulation of light with much bigger wavelength than the material size. In the process of interaction between light and matters, plasmonic materials can transform electro-magnetic energy into processes on the nanoscale, so called surface plasmon polaritons, in the terahertz regime. Due to severe ohmic losses of a metal in the terahertz regime, a plasmon inside a metal usually has a very short lifetime while a plasmon on the surface of the metal can be alive for a longer time. Therefore, the plasmon existing on the surface of a metal is more important in the terahertz regime and is separately referred to as a surface plasmon. In other words, surface plasmons are surface electromagnetic waves at the interface between a dielectric material and a metal [15]. Interestingly, human beings have utilized these effects without any knowledge of surface plasmon resonances for a long time such as in stained-glass windows shown in Fig. 1.5a. Small particles made of metallic salts are incorporated into the glass, and they absorb and scatter light giving colors to the glass.

1.2.2. Metamaterials fabrication challenge

In 1999, Pendry predicted that specifically engineered artificial materials, *i.e.* metamaterials, would have unusual magnetic responses, *e.g.* negative permeability [7]. Following his work, much effort has been devoted to metamaterials design and fabrication for obtaining interesting optical properties, including unlimited imaging and cloaking. However, since current metamaterials fabrication techniques rely highly on top-down lithographic approaches [16], the fabrication of three-dimensional metamaterials, e.g. structures shown in Fig. 1.3b, is still challenging thus hampering their practical applications. For overcoming fabrication challenges, novel fabrication technologies beyond lithography techniques are demanding. Bottom-up type approaches to metamaterials fabrication are promising for their potential to enable large-scale materials synthesis. Especially, to obtain interesting optical properties in the visible regime, the unit dimension of materials need to be approximately smaller than 100 nm. Since block copolymer phase separation typically occurs on the tens of nanometer scale, block copolymer self-assembly provides a promising path towards novel optically active materials.

1.2.3. Block copolymer derived metamaterials

Block copolymers can provide facile routes for controlling morphologies with structural length scales down to the nanometer scale. Morphologies include 3-dimensionally isotropic morphologies like the Gyroid structure [17]. Our strategy for metamaterials fabrication is to utilize block copolymers as templates. Selective etching of nanostructured block copolymers yields porous templates and metals can be deposited into the porous templates using known deposition approaches, e.g. electro, electroless and atomic layer deposition. However, optical properties of such materials have not been extensively studied to date. For obtaining targeted properties of metamaterials, theoretical predictions are critically required but often lacking. To this end, optical properties of block copolymer derived metamaterials are studied numerically in Chapter 4. Further in-depth understanding of the optical behavior of such metamaterials as well as novel metamaterials with novel and unusual properties are described in Chapter 5.

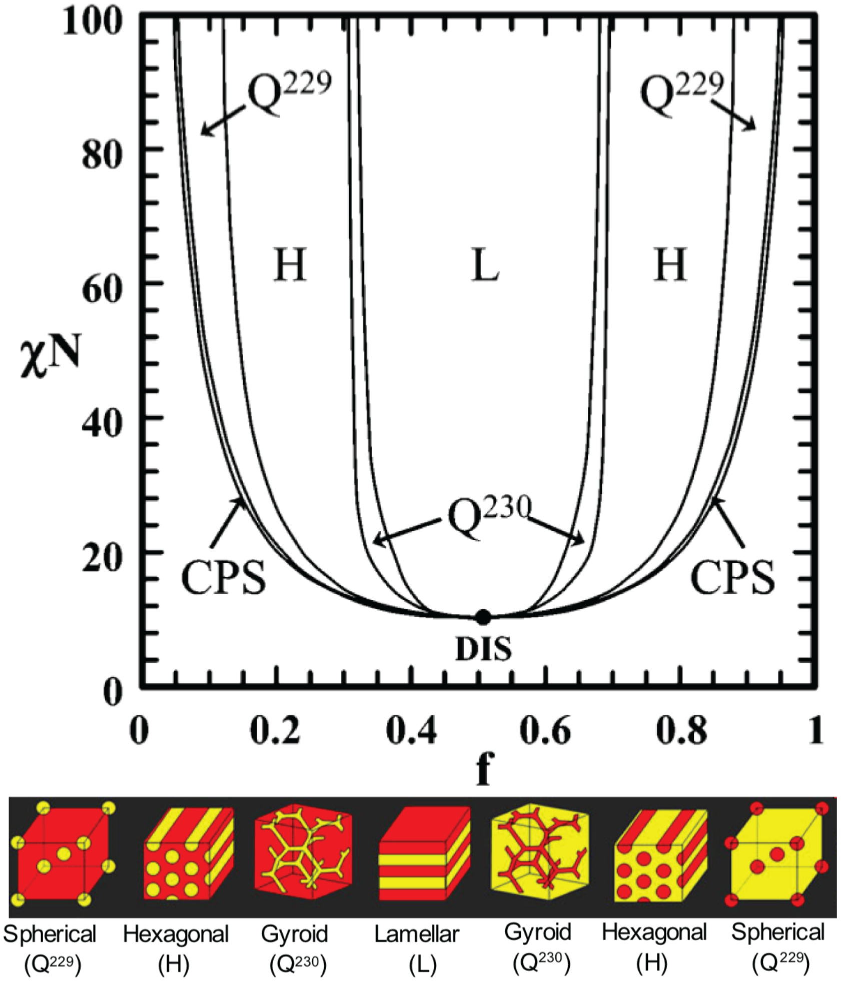

Figure 1.1. Theoretical phase-diagram of di-block copolymers [3] and schematics of predicted morphologies

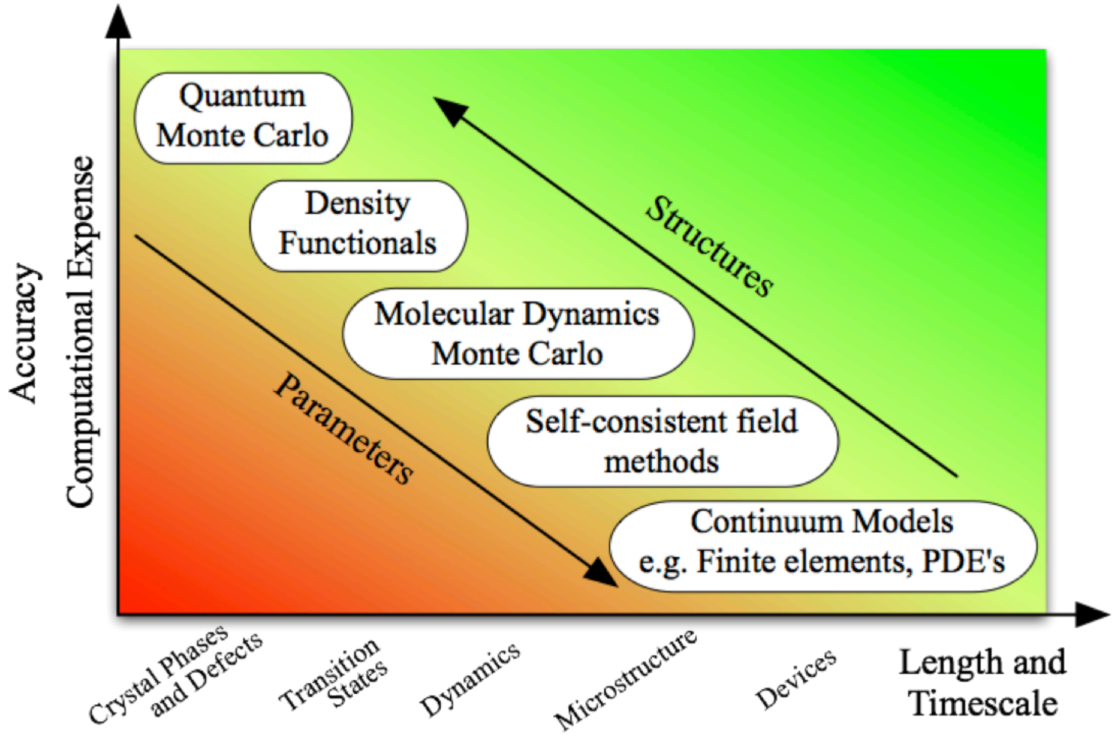

Figure 1.2. Various computational approaches and computational budgets of simulated system size or timescale.

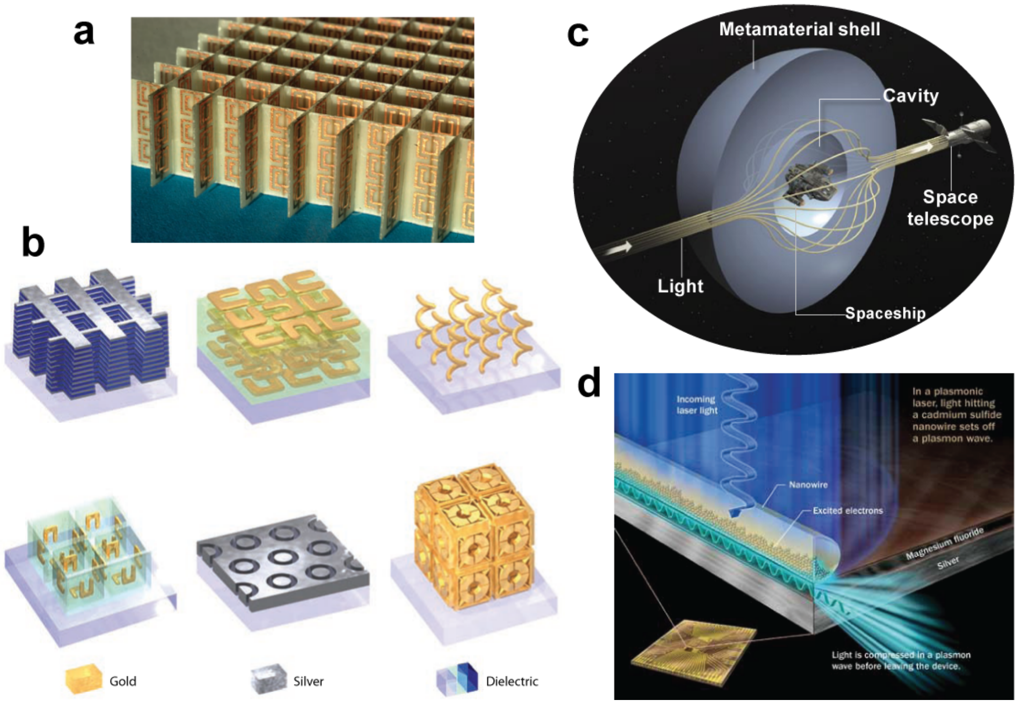

Figure 1.3. Novel optical applications initiated by recent advances of nano-photonics. **a**, A negative refractive index metamaterial composed of split ring resonators by Pendry [7]. Negative refractive index metamaterials enable us to overcome the diffraction limit of light for an optical apparatus. **b**, Various metamaterial structures exhibiting unusual optical phenomena including negative refraction and circular dichroism **c**, Hiding any objects inside of a metamaterial shell, *i.e.* an invisibility cloak composed of metamaterials. **d**, An imaginative plasmonic computing device.

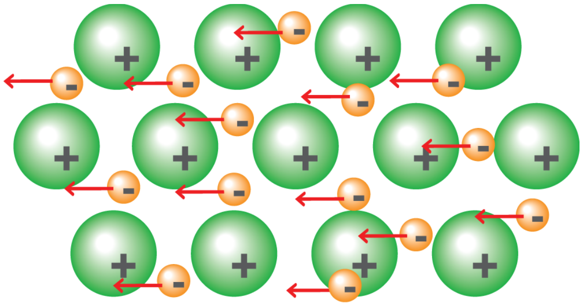

Figure 1.4. Plasmons are an oscillation of free electron density in a metal.

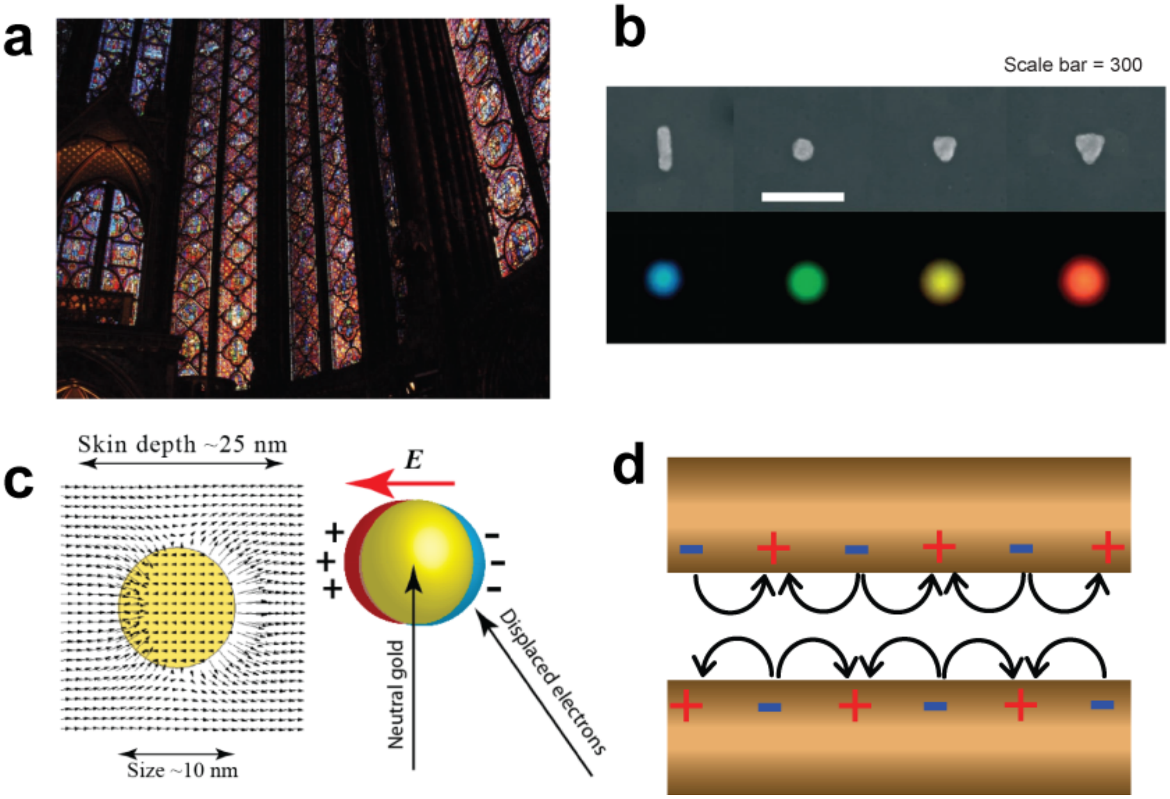

Figure 1.5. Surface plasmon resonance phenomena of nanoscale metallic materials **a**, A stained-glass window is an old example of surface plasmon applications, where suspended metallic nanoparticles in the glass absorb and scatter light giving colors to the window. **b**, Scanning electron microscope and dark field optical microscope images of metallic nanoparticles exhibiting the optical behavior of surface plasmons with the variation of their size and shape. **c**, The near electric fields and the electron motion of the surface plasmon resonance of a spherical metallic nanoparticle. **d**, A metal/dielectric/metal surface plasmon waveguide and surface plasmon polaritons on the waveguide.

REFERENCES

[1] M. Kamperman, U. Wiesner, *Bioinspired Block Copolymer-Based Hybrid Materials in "The Supramolecular Chemistry of Organic-Inorganic Hybrid Materials"*. The Supramolecular Chemistry of Organic-Inorganic Hybrid Materials (John Wiley & Sons, Inc., 2010), pp. 599-636.

[2] S. C. Warren, L. C. Messina, L. S. Slaughter, M. Kamperman, Q. Zhou, S. M. Gruner, F. J. DiSalvo, U. Wiesner, Ordered mesoporous materials from metal nanoparticle-block copolymer self-assembly. *Science* **320** (5884), 1748-1752 (Jun 27, 2008).

[3] E. W. Cochran, C. J. Garcia-Cervera, G. H. Fredrickson, Stability of the Gyroid Phase in Diblock Copolymers at Strong Segregation. *Macromolecules* **39** (7), 2449-2451 (2006/04/01, 2006).

[4] D. Frenkel, B. Smit, *Understanding molecular simulation : from algorithms to applications*. Computational science, from theory to applications ; v. 1 (Academic Press, San Diego, ed. 2nd, 2002), pp. xxii, 638 p.

[5] Y. Bohbot-Raviv, Z.-G. Wang, Discovering New Ordered Phases of Block Copolymers. *Physical Review Letters* **85** (16), 3428 (2000).

[6] M. W. Matsen, M. Schick, Stable and unstable phases of a diblock copolymer melt. *Physical Review Letters* **72** (16), 2660 (1994).

[7] J. B. Pendry, A. J. Holden, D. J. Robbins, W. J. Stewart, Magnetism from conductors and enhanced nonlinear phenomena. *Microwave Theory and Techniques, IEEE Transactions on* **47** (11), 2075-2084 (1999).

[8] L. Novotny, B. Hecht, *Principles of nano-optics*. (Cambridge University Press, Cambridge, 2006).

[9] J. B. Pendry, Negative Refraction Makes a Perfect Lens. *Physical Review Letters* **85** (18), 3966 (2000).

[10] J. B. Pendry, D. Schurig, D. R. Smith, Controlling Electromagnetic Fields. *Science* **312** (5781), 1780-1782 (2006).

[11] D. P. O'Neal, L. R. Hirsch, N. J. Halas, J. D. Payne, J. L. West, Photo-thermal tumor ablation in mice using near infrared-absorbing nanoparticles. *Cancer Letters* **209** (2), 171-176 (2004).

[12] H. A. Atwater, A. Polman, Plasmonics for improved photovoltaic devices. *Nat Mater* **9** (3), 205-213 (2010).

[13] N. W. Ashcroft, N. D. Mermin, *Solid state physics*. (Holt, New York,, 1976), pp. xxi, 826 p.

[14] J. D. Joannopoulos, *Photonic crystals : molding the flow of light*. (Princeton University Press, Princeton, ed. 2nd, 2008), pp. xiv, 286 p.

[15] S. A. Maier, *Plasmonics : fundamentals and applications*. (Springer, New York, ed. 1st, 2007), pp. xxiv, 223 p.

[16] C. M. Soukoulis, M. Wegener, Past achievements and future challenges in the development of three-dimensional photonic metamaterials. *Nat Photon* **5** (9), 523-530 (2011).

[17] A. H. Schoen, *Infinite periodic minimal surfaces without self-intersections*. (National Aeronautics and Space Administration; [for sale by the

Clearinghouse for Federal Scientific and Technical Information, Springfield, Va.], Washington, 1970).

CHAPTER 2

Mesoscopic Structure Prediction of Nanoparticle Assembly and Co-Assembly : Theoretical foundation[1]

ABSTRACT

In this work, we present a theoretical framework that unifies polymer field theory and density functional theory in order to efficiently predict ordered nanostructure formation of systems having considerable complexity in terms of molecular structures and interactions. We validate our approach by comparing its predictions with previous simulation results for model systems. We illustrate the flexibility of our approach by applying it to hybrid systems composed of block copolymers and ligand coated nanoparticles. We expect that our approach will enable the treatment of multi-component self-assembly with a level of molecular complexity that approaches experimental systems.

---

[1] Reproduced with permission from: Kahyun Hur, Richard G. Hennig, Fernando A. Escobedo, and Ulrich Wiesner, *J. Chem. Phys.* **133** (19), 194108-12. Copyright 2010 American Institute of Physics.

2.1. Introduction

Nanoparticle (NP) assembly and co-assembly are topics of significant current scientific interest due to their potential impact on the engineering of new materials. Recent advances in synthesis allow the growth of monodisperse NPs from a wide range of solids, *e.g.* metals, semiconductors, and insulators [1-5]. This control enables ordered crystal formation, including binary superlattices at the mesoscopic scale (1 to 1000 *nm*), thus providing powerful modular pathways to the design of 'metamaterials' that should ultimately result in devices with programmable chemical and physical properties [6-9]. NP formation and assembly has also been found to play a critical role in natural biomineralization processes. It recently has been shown that amourphous calcium carbonate (ACC) NPs nucleate in solution and assemble at an ordered template of macromolecules thus challenging classical crystallization theories [10-11]. Similar NP assembly behavior is currently utilized in the field of synthetic porous solids [12]. Aside from oxide structures mesoporous bulk metals are formed from block copolymer (BCP) / metal NP self-assembly through careful tailoring of particle-polymer-solvent and particle-particle interactions [13]. In many of these experimental systems, chemical building blocks are complex organic/inorganic hybrid molecules such as ligand-stabilized NPs. Furthermore, Coulomb or dipolar long-range particle-particle interactions are believed to play an essential role in their assembly. In particular for complex multi-component systems involving assembly of NPs and macromolecules, limited understanding of the role of such key factors has severely hampered progress. Clearly, better predictive theoretical and simulation methods are needed.

To this end, we present an efficient theoretical framework that unifies polymer field theory and density functional theory (DFT) into a single method in order to incorporate complex molecular details with key physical interactions. Atomistic or particle-based modeling such as molecular dynamics and Monte Carlo (MC) simulations can readily incorporate different molecular details but are computationally more expensive than field-theoretical approaches. Furthermore, they require specialized methods to measure or impose chemical potentials and an analysis of finite system-size effects to ensure that structures at thermodynamic equilibrium are obtained (*e.g.*, some morphological features can be frustrated by a lack of geometric commensurability with the box dimensions) [14-18]. Alternatively, the morphologies of BCP self-assembly have been successfully studied and predicted by self-consistent field theory (SCFT) [14, 19-23], a field theoretic description of chemical fields exploiting the mean-field approximation [21]. Shi *et al.* [56] and Wang *et al.* [57] proposed SCFT approaches to simulate polyelectrolyte by incorporating Coulomb interactions between polymer segments. The SCFT approach is very efficient and powerful, but the original SCFT approach is not readily applicable to systems beyond BCP self-assemblies due to its inability to describe the interactions associated with NPs. A combined approach of atomistic and field theoretic modeling as well as a novel MC approach have been suggested for simulation of BCP/NP self-assembly [24], but they have the same or similar limitations found in atomistic simulations. Meanwhile, DFT approaches were suggested for different molecular systems [25-27], but their applications were limited to local structure prediction. Thompson *et al.* introduced a new numerical scheme of combining SCFT with DFT [28-29]. The

SCFT/DFT approach seems quite promising for investigating the equilibrium properties of BCP/NP composites, but its application has been limited to simple mixture systems of BCPs and hard sphere (HS) particles [28-30]. Due to the difficulties in describing arbitrary types of molecular structures and interactions, applications of field theoretic approaches to more complex molecular systems such as those systems with charged NPs or ligand-stabilized NPs remain a significant challenge.

In order to overcome such limitations of existing theories, we extend the Green function propagator to hard particles and incorporate key physical interactions in the form of direct correlation functions for complex molecular systems. The Green function propagator approach has been used to describe polymer configurations in polymer field theory, but their applications have been limited to polymers. By using this propagator we introduce a theoretical framework that enables us to integrate not only discrete but also continuous segments into a molecule. The framework offers greater flexibility to incorporate complex molecules composed of soft and hard chemical species than existing SCFT, SCFT/DFT, and other polymer DFT approaches.[27,46] The direct correlation functions are widely used in well-established DFT approaches.[31] Atomistic interactions such as Coulomb [32-34], Yukawa [33], dipole [34], and Lennard-Jones interactions [33, 35] can be incorporated in this context. Therefore, our approach enables us to incorporate the complexity of molecular structures and their interactions while taking advantage of the efficiency of field theories for sampling phase space of molecular systems. We demonstrate the validity of our approach by first comparing its predictions with previous results [28] and then applying it to a hybrid materials system consisting of multi-component molecules with NPs. Further applications of our approach will be presented elsewhere [36].

2.2. Theoretical and numerical procedures

2.2.1. Overview

Our field-theoretic approach is based on the minimization of the Helmholtz free energy functional, $F\left[\rho, w\right]$, of a system with respect to variations of the density functions, ρ, and chemical fields, w. The general schematic procedure and key equations are summarized in Fig. 2.1. In Sections 2.2.2 and 2.2.3, F is obtained from the particle-based partition function, where interactions are added to the excess free energy functional, F^{ex}, in a functional form. Various interactions can be incorporated following Eq. (11). The process is similar to that of incorporating different force field terms in particle-based simulations. The most general form of F for the present work is given as Eqs. (9) and (13). In Sections 2.2.3 and 2.2.4, the chemical fields, w, given in Eqs. (14) and (18) are obtained from the functional derivative of F with respect to ρ. In Section 2.2.5, the density functions, ρ, are obtained from the functional derivative of F with respect to w, see Eq. (40). It is shown that ρ can be calculated from the single molecular partition function Q and the segment distribution functions, q and $q^{\dagger}$. To obtain Q, q and $q^{\dagger}$, we introduce the Green's function, G, that propagates from one segment to another as i to $i+1$ in Fig. 2.2. The density distribution functions q and $q^{\dagger}$ for each segment are calculated from their convolution with G via Eqs. (34) and (35) with the boundary conditions given by Eqs. (37) and (38). In Section 2.2.6, q, $q^{\dagger}$, and G are formulated for continuous segments, see Eqs. (44), (47), and (48). For each step in the calculations outlined in Fig. 2.1, w and ρ are updated iteratively until changes of $\rho(\mathbf{r})$ and $w(\mathbf{r})$ become sufficiently small. Finally, in Section 2.2.7, field theories beyond the mean-field approximation in Section 2.2.7 are considered.

2.2.2. Helmholtz free energy functional

For clarity, we only present the equations derived for a homogeneous system with one type of molecule; the extension to inhomogeneous mixture systems is straightforward. The configurational partition function of the canonical ensemble is given by

$$Z = \frac{1}{n!}\int d\mathbf{r}^n P\left(\mathbf{r}^n\right) E\left(\mathbf{r}^n\right) R\left(\mathbf{r}^n\right) \exp\left[-U\left(\mathbf{r}^n\right)/k_B T\right], \tag{1}$$

where n is the number of molecules, $R\left(\mathbf{r}^n\right)$ is the incompressibility constraint term, $U\left(\mathbf{r}^n\right)$ is the interaction potential, and $k_B T$ is the Boltzmann constant multiplied by the temperature (note that we neglect unimportant constant terms such as the de Broglie thermal wavelength). The term $P\left(\mathbf{r}^n\right)$ accounts for the molecular configuration of multi-component molecules such as polymers or hybrid molecules (see discussion in Section 2.2.5). For hard particle interactions, the excluded volume constraint, $E\left(\mathbf{r}^n\right)$, is included. For multi-component molecules, we specify each monomer species with a parameter, i. The density operator of the ith monomer species, $\hat{\rho}_i\left(\mathbf{r}\right)$, for multi-component molecules is given by

$$\hat{\rho}_i\left(\mathbf{r}\right)=\sum_j^n \delta\left[\mathbf{r}-\mathbf{r}_i^j\right], \tag{2}$$

where $\mathbf{r}_i^j$ is the positional vector of the monomer species i of molecule j. Consequently, $U\left(\mathbf{r}^n\right)$ is given by

$$U\left(\mathbf{r}^n\right)=\frac{1}{2}\sum_{i,j}\iint d\mathbf{r}d\mathbf{r}'\hat{\rho}_i\left(\mathbf{r}\right)u_{ij}\left(\mathbf{r},\mathbf{r}'\right)\hat{\rho}_j\left(\mathbf{r}'\right), \tag{3}$$

where $u_{ij}\left(\mathbf{r},\mathbf{r}'\right)$ is a pair potential function describing the interaction between monomer species i at $\mathbf{r}$ and j at $\mathbf{r}'$. For example, $u_{ij}\left(\mathbf{r},\mathbf{r}'\right)$ for Coulomb interactions between point charges is given by $u_{ij}\left(\mathbf{r},\mathbf{r}'\right)=Z_iZ_j/4\pi\varepsilon\left|\mathbf{r}-\mathbf{r}'\right|$, where Z_i and Z_j are charges of species i and j respectively, and ε is the permittivity. The 2nd order direct correlation function defined by $C_{ij}\left(\mathbf{r},\mathbf{r}'\right)=-1/k_BT\cdot D^2F^{ex}/D\rho_i\left(\mathbf{r}\right)D\rho_j\left(\mathbf{r}'\right)$ in Sections 2.2.3 and 2.2.4 has a meaning consistent with $-u_{ij}\left(\mathbf{r},\mathbf{r}'\right)/k_BT$, where $F^{ex}\left[\rho\right]$ is the ‘excess’ free energy functional and the free energy contributions of pair-wise interactions between particles (noting that $DF/D\rho$ denotes the functional derivative of the functional $F[\rho]$). Higher order direct correlation functions than 2nd order can be neglected for slowly varying potentials such as the Coulomb potential without significant loss of accuracy [33], since they are related to multi-body interactions. The excluded volume constraint $E(\mathbf{r}^n)$ in Eq. (1) is also included in the excess free energy functional form as in Section 2.2.4. Therefore, particle-particle interactions including enthalpic interactions and purely entropic excluded volume interactions are given in the form of the excess free energy functional. In field theoretic approaches, the partition function Z is re-expressed in terms of local densities, $\rho(\mathbf{r})$, and chemical potential fields, $w(\mathbf{r})$, using the identities for the delta functional [20, 37],

$$\int D\rho_i \delta\left[\rho_i - \hat{\rho}_i\right] = 1 \tag{4}$$

and

$$\delta\left[\rho_i - \hat{\rho}_i\right] = \int Dw_i \exp\left[\int d\mathbf{r} w_i(\mathbf{r})\left\{\rho_i(\mathbf{r}) - \hat{\rho}_i(\mathbf{r})\right\}\right], \tag{5}$$

where D represents the functional integral. Then Z for the field theoretic description takes the form

$$\begin{aligned} Z = \frac{C}{n!}\int D\xi\left(\prod_i^N D\rho_i Dw_i \exp\left\{\int d\mathbf{r} w_i(\mathbf{r})\rho_i(\mathbf{r})\right\}\right) \\ \times Q^n\left[\{w\}\right]\exp\left\{\int d\mathbf{r}\xi(\mathbf{r})\left[1-\sum_i^N \varphi_i(\mathbf{r})\right]\right\}\exp\left[-\frac{1}{k_B T}F^{ex}\right] \end{aligned} \tag{6}$$

where C is the normalization constant, N is the number of monomer species in one molecule, and Q is the single molecular partition function discussed in Section 2.2.5. The excess free energy functional F^{ex} details interactions between particles as $U\left(\mathbf{r}^n\right)$ in Eq. (1) and will be discussed more detail in Section 2.2.3. The incompressibility term, $R\left(\mathbf{r}^n\right)$, in Eq. (1) is given in a functional form,

$$\delta\left(1-\sum_i^N \varphi_i\left(\mathbf{r}\right)\right)=\int D\xi \exp\left\{\int d\mathbf{r}\xi\left(\mathbf{r}\right)\left[1-\sum_i^N \varphi_i\left(\mathbf{r}\right)\right]\right\}, \tag{7}$$

satisfying the incompressibility condition,

$$\sum_i^N \varphi_i\left(\mathbf{r}\right)=1, \tag{8}$$

where $\varphi_i\left(\mathbf{r}\right)$ is the local volume fractional functional of the i th monomer species, obtained from its density function, $\rho_i\left(\mathbf{r}\right)$, by convolution with its shape function, $S_i\left(\mathbf{r}\right)$, defined as $S_i\left(\mathbf{r}\right)=\rho_0^{-1}\delta\left(\left|\mathbf{r}\right|\right)$ for point-like monomer species, and $S_i\left(\mathbf{r}\right)=H\left(R_i-\left|\mathbf{r}\right|\right)$ for spherical monomer species, where ρ_0^{-1} is the reference volume for point-like monomer species, $\delta\left(x\right)$ is the Dirac delta function, $H(x)$ is the Heaviside step function, and R_i is the radius of the spherical monomer species i. The $\xi\left(\mathbf{r}\right)$ is a Lagrange multiplier function that needs to be chosen to satisfy Eq. (8).

The Helmholtz free energy functional, F, is given as

$$F\left[\rho, w\right] = F^0\left[\rho, w\right] + F^{ex}\left[\rho\right], \tag{9}$$

where F^0 describes the mixing and conformational entropy as well as the pressure energy, and is obtained from

$$\begin{aligned} F^0 / k_B T = -n \ln Q\left[\{w\}\right] - \sum_i \left\{\int d\mathbf{r} w_i(\mathbf{r}) \rho_i(\mathbf{r})\right\} \\ - \int d\mathbf{r} \xi(\mathbf{r})\left[1 - \sum_i \varphi_i(\mathbf{r})\right] \end{aligned}, \tag{10}$$

where we neglect unimportant constant terms for clarity. When the incompressibility condition is satisfied, the last term of Eq. (10) vanishes.

2.2.3. The excess free energy functional

F^{ex} in Eq. (9) primarily contains the enthalpic interactions between all species but also includes purely entropic hard sphere (HS) interaction terms (hence the notation of ‘excess’ instead of ‘enthalpic’); in its most general form it is given by:

$$F^{ex} = F^{\chi} + F^{HS} + F^{C} + F^{Dipole} + F^{Yukawa} + \cdots. \tag{11}$$

The conventional SCFT approach [14, 19-23, 38-39] only includes the first term describing short range enthalpic interactions, F^{χ}. A combined SCFT/DFT approach was recently developed to also implement short range HS interactions, F^{HS}, in addition to F^{χ} [28-30]. In order to describe more realistic experimental systems, long range interactions such as Coulomb, F^{C}, dipole, F^{Dipole}, and screened Coulomb interactions, F^{Yukawa}, have to be included. By choosing Coulomb interactions as an example, here we introduce our strategy to implement such long range interactions. The excess free energy functional is obtained as

$$\begin{aligned} F^{ex}/k_BT &= \sum_{i<j}\rho_0\chi_{ij}\iint d\mathbf{r}d\mathbf{r}'\varphi_i(\mathbf{r})\varphi_j(\mathbf{r}')+\int d\mathbf{r}\Phi^{HS}\left[\{\rho\};\mathbf{r}\right] \\ &-\frac{1}{2}\sum_{ij}\iint d\mathbf{r}d\mathbf{r}'\rho_i(\mathbf{r})C_{ij}^{C}(\mathbf{r},\mathbf{r}')\rho_j(\mathbf{r}') \end{aligned}, \qquad (12)$$

where the first term represents F^{χ}, the second term F^{HS}, and the last term F^{C}. Here C_{ij}^{C} is the direct correlation function for Coulomb interactions [33]. By combining Eqs. (10) and (12), the Helmholtz free energy functional, F, is obtained as

$$\begin{aligned} F/k_BT &= -n\ln Q\left[\{w\}\right]-\sum_i\left\{\int d\mathbf{r}w_i(\mathbf{r})\rho_i(\mathbf{r})\right\} \\ &-\int d\mathbf{r}\xi(\mathbf{r})\left[1-\sum_i\varphi_i(\mathbf{r})\right] \\ &+\sum_{i<j}\rho_0\chi_{ij}\iint d\mathbf{r}d\mathbf{r}'\varphi_i(\mathbf{r})\varphi_j(\mathbf{r}')+\int d\mathbf{r}\Phi^{HS}\left[\{\rho\};\mathbf{r}\right] \\ &-\frac{1}{2}\sum_{ij}\iint d\mathbf{r}d\mathbf{r}'\rho_i(\mathbf{r})C_{ij}^{C}(\mathbf{r},\mathbf{r}')\rho_j(\mathbf{r}') \end{aligned}, \qquad (13)$$

where the first three terms in the right hand side represent the entropic part, F^{0}, and the last three terms represent the excess part, F^{ex}, for short-range enthalpic, HS, and long-range Coulomb interactions, respectively. The Helmholtz free energy functional, F, is not directly used in the self-consistent iteration process, but is evaluated for obtaining the system with the lowest free energy as shown in Fig. 2.1. Applying the mean-field approximation [21, 38], the average chemical potential field felt by the i th monomer, $w_i(\mathbf{r})$, is obtained at saddle points of F, where $DF / D\rho_i(\mathbf{r}) = 0$, and is given by

$$w_i(\mathbf{r}) = \left[\mu_i^{\chi}(\mathbf{r}) + \mu_i^{HS}(\mathbf{r}) + \mu_i^{C}(\mathbf{r})\right] / k_B T + \Xi_i(\mathbf{r}). \tag{14}$$

where $\mu_i^{\chi}(\mathbf{r})$, $\mu_i^{HS}(\mathbf{r})$, and $\mu_i^{C}(\mathbf{r})$, are the chemical potential fields of short range enthalpic, short range HS, and long range Coulomb interactions, respectively, and $\Xi_i(\mathbf{r})$ is the pressure field for monomer i. As in the conventional SCFT, short range enthalpic interactions between distinct chemical species are described by dimensionless Flory-Huggins interaction parameters, χ_{ij}, and the first term in Eq. (14), $\mu_i^{\chi}(\mathbf{r})$, is given by

$$\mu_i^{\chi}(\mathbf{r}) / k_B T = \frac{\rho_0}{N} \int d\mathbf{r}' S_i(\mathbf{r}' - \mathbf{r}) \sum_{i \neq j} \chi_{ij} N \varphi_j(\mathbf{r}'). \tag{15}$$

Here we use χ_{ij} parameters for the short range enthalpic interactions, since experimental solubility parameters can be directly applied as simulation parameters. We utilize the fundamental measure theory (FMT) approach [39] for short range HS interactions described by the second term, $\mu_i^{HS}(\mathbf{r})$ in Eq. (14), as outlined in Ref. [33] and repeated in Section 2.2.4. The third term in Eq. (14), $\mu_i^{C}(\mathbf{r})$, describes the long-range Coulomb interactions and is obtained from the direct correlation function as

$$\mu_i^C(\mathbf{r})/k_BT = -\sum_j \int d\mathbf{r}' C_{ij}^C(\mathbf{r},\mathbf{r}')\rho_j(\mathbf{r}'), \tag{16}$$

The non-negligible contribution of the long range Coulomb potential tail on the chemical field is efficiently computed via the Ewald summation technique [31]. Thus, long range interactions can be incorporated into the theory by using direct correlation functions and the Ewald summation technique, which is discussed in Section 2.2.4. Other long-range interactions such as screened Coulomb [33], dipole [34], and Lennard-Jones interactions [33, 35] can be included in the theory in the same way as the Coulomb interaction case exemplified here. Finally, the last term in Eq. (14), $\Xi_i(\mathbf{r})$, is given by

$$\Xi_i(\mathbf{r}) = \frac{\rho_0}{N}\int d\mathbf{r}' \xi(\mathbf{r}') S_i(\mathbf{r}'-\mathbf{r}). \tag{17}$$

Combining Eqs. (15), (16), and (17) yields the chemical fields felt by monomer species i

$$\begin{aligned} w_i(\mathbf{r}) = {} & \frac{\rho_0}{N}\int d\mathbf{r}' \left[\sum_j \chi_{ij} N \varphi_j(\mathbf{r}') + \xi(\mathbf{r}') \right] S_i(\mathbf{r}'-\mathbf{r}) \\ & + \mu_i^{HS}(\mathbf{r})/k_B T - \sum_j \int d\mathbf{r}' C_{ij}^{C}(\mathbf{r},\mathbf{r}')\rho_j(\mathbf{r}') \end{aligned} . \qquad (18)$$

2.2.4. Density Functional Form

To account for excluded volume interactions in our field theoretic approach, we include the excluded volume constraint, $E\left(\mathbf{r}^n\right)$, in Eq. (1) that particles cannot concurrently occupy the same space. In contrast to other interactions, hard-particle interactions are purely entropic. Unfortunately, there is no exact analytic solution for 3-dimensional systems. Instead, Percus obtained an exact result for the free energy density of 1-dimensional hard rods [40]. Although the 1-dimensional result is not widely useful in itself, it is an important starting point for evaluating other hard-particle interactions [41]. The FMT method pioneered by Rosenfeld for hard-particle interactions in 3 dimensions is based on Percus' result [39]. In the present work, we utilize the FMT since it is the most advanced hard particle DFT for inhomogeneous hard body systems [41]. The FMT was originally developed for inhomogeneous mixture systems of HSs. It supersedes other approaches in (i) providing flexibility for incorporating inhomogeneous hard particle mixtures, and in (ii) providing accurate predictions for dense packing behaviors, *e.g.* liquid to solid transitions, of hard particles [41-42]. The excess free energy functional is given as

$F^{HS}/k_BT = \int d\mathbf{r}\Phi^{HS}(\mathbf{r})$, where the excess free energy density, Φ^{HS}, is obtained from

$$\begin{aligned}\Phi^{HS}(\mathbf{r}) &= -n_0\ln(1-n_3)+n_1n_2/(1-n_3)+n_2^3/(1-n_3)^2/(24\pi)\\ &-\mathbf{n}_{V1}\cdot\mathbf{n}_{V2}/(1-n_3)-n_2(\mathbf{n}_{V1}\cdot\mathbf{n}_{V2})/(1-n_3)^2/(8\pi)\end{aligned}. \qquad (19)$$

Φ^{HS} is a function of the weighted densities, n_α, which are given by

$$n_\alpha(\mathbf{r}) = \sum_i\int d\mathbf{r}'\rho_i(\mathbf{r}')W_i^{(\alpha)}(\mathbf{r}-\mathbf{r}'), \qquad (20)$$

where the weighting functions are $W_i^{(3)}(\mathbf{r}) = H(R_i-|\mathbf{r}|)$, $W_i^{(2)}(\mathbf{r}) = \delta(R_i-|\mathbf{r}|)$, $\mathbf{W}_i^{(V2)}(\mathbf{r}) = \frac{\mathbf{r}}{|\mathbf{r}|}\delta(R_i-|\mathbf{r}|)$, $W_i^{(1)}(\mathbf{r}) = W_i^{(2)}(\mathbf{r})/4\pi R_i$, $W_i^{(0)}(\mathbf{r}) = W_i^{(2)}(\mathbf{r})/4\pi R_i^2$, and $\mathbf{W}_i^{(V1)}(\mathbf{r}) = \mathbf{W}_i^{(V2)}(\mathbf{r})/4\pi R_i$ and R_i is the radius of HS particle i. The excess chemical potential functional is obtained as

$$\mu_i^{HS}(\mathbf{r})/k_BT = \int d\mathbf{r}'\sum_\alpha \mu_\alpha W_i^{(\alpha)}(\mathbf{r}'-\mathbf{r}), \qquad (21)$$

where $\mu_\alpha = \partial\Phi^{HS}/\partial n_\alpha$ and

$$\begin{aligned}
&\mu_0 = -\ln\left(1-n_3\right), \\
&\mu_1 = n_2 / \ln\left(1-n_3\right), \\
&\mu_2 = n_1 / \left(1-n_3\right) + \left(1/8\pi\right) n_2^2 / \left(1-n_3\right)^2 \\
&-\left(1/8\pi\right) \mathbf{n}_{V2} \cdot \mathbf{n}_{V2} / \left(1-n_3\right)^2, \\
&\mu_3 = n_0 / \left(1-n_3\right) + n_1 n_2 / \left(1-n_3\right)^2 \\
&-\left(1/12\pi\right) n_2^3 / \left(1-n_3\right)^3 - \mathbf{n}_{V1} \cdot \mathbf{n}_{V2} / \left(1-n_3\right)^2 \\
&-\left(1/4\pi\right) n_2 \mathbf{n}_{V2} \cdot \mathbf{n}_{V2} / \left(1-n_3\right)^3, \\
&\mu_{V1} = -\mathbf{n}_{V2} / \left(1-n_3\right), \\
&\mu_{V2} = -\mathbf{n}_{V1} / \left(1-n_3\right) - \left(1/4\pi\right) n_2 \mathbf{n}_{V2} / \left(1-n_3\right)^2
\end{aligned} \quad . \tag{22}$$

The direct correlation function for the Coulomb potential, $V(\mathbf{r})/k_B T = \Gamma Z_i Z_j / |\mathbf{r}|$, was obtained based on the mean-spherical approximation [42]. The direct correlation function, C_{ij}^C, for charged HS particles can be interpreted as the effective interaction between two spherical cavities with the radii, R_i and R_j, where charges are uniformly distributed [33]. Blum's theory for C_{ij}^C is also based on interactions between two spherical charged cavities with radii increased as much as the capacitance length [32, 43-44]. In this work, we use Rosenfeld's formulation of the direct correlation function [42] which is given by

$$C_{ij}^C\left(\mathbf{r}_i, \mathbf{r}_j\right) = -Z_i Z_j \Gamma \iint d\mathbf{r}' d\mathbf{r}'' W_i^{(2)}\left(\mathbf{r}_i - \mathbf{r}'\right) W_j^{(2)}\left(\mathbf{r}_j - \mathbf{r}''\right) / \left|\mathbf{r}' - \mathbf{r}''\right| \tag{23}$$

and

$$\frac{-C_{ij}^{C}\left(\mathbf{r},\mathbf{r}'\right)}{Z_i Z_j \Gamma} = \begin{cases} 2B_0\left(R_i + R_j - \tau_{ij}\right), \text{ if } \left|\mathbf{r}-\mathbf{r}'\right| < \tau_{ij} \\ 2B_0\left(R_i + R_j - \tau_{ij}\right) - B_0\left(\left|\mathbf{r}-\mathbf{r}'\right| - \tau_{ij}\right)^2 \dfrac{1}{\left|\mathbf{r}-\mathbf{r}'\right|}, \text{if } \tau_{ij} < \left|\mathbf{r}-\mathbf{r}'\right| < R_i + R_j \\ \dfrac{1}{\left|\mathbf{r}-\mathbf{r}'\right|}, \text{ if } R_i + R_j < \left|\mathbf{r}-\mathbf{r}'\right| \end{cases} ,$$

(24)

where $\tau_{ij} = \left|R_i - R_j\right|$ and $B_0 = 2\pi\left(4\pi R_i R_j\right)/\left(4\pi R_i^2\right)\left(4\pi R_j^2\right)$. The Coulomb potential decays slowly and long-range contributions to the free energy in a periodic system are not negligible. The Ewald summation technique is widely used to calculate the long-range contributions efficiently [31]. In this work, the Ewald summation technique is not applied to the Coulomb potential. Instead, since long-range contributions are very important in the formation of ordered nanostructure [36], we introduce our approach to apply the Ewald summation technique in the context of the direct correlation function. The chemical potential from the Ewald summation is separately calculated and the direct correlation function is modified as

$$\begin{aligned} \mu_i^C\left(\mathbf{r}\right)/k_B T &= -\sum_j \int d\mathbf{r}' C_{i,j}^{C}\left(\mathbf{r},\mathbf{r}'\right)\rho_j\left(\mathbf{r}'\right) \\ &= -\sum_j \int d\mathbf{r}' C_{i,j}^{C\,\prime}\left(\mathbf{r},\mathbf{r}'\right)\rho_j\left(\mathbf{r}'\right) + \mu_i^{C,ew}\left(\mathbf{r}\right) \end{aligned} \qquad (25)$$

and

$$C_{ij}^{C'}(\mathbf{r},\mathbf{r}') = C_{ij}^{C}(\mathbf{r},\mathbf{r}') + \frac{Z_i Z_j \Gamma}{|\mathbf{r}-\mathbf{r}'|} erf\left(\sqrt{\alpha}|\mathbf{r}-\mathbf{r}'|\right), \tag{26}$$

where the positive constant α in the error function $erf(x)$ determines the width of the Gaussian compensating charge distribution. The reciprocal space contribution, $\mu_i^{C,ew}(\mathbf{r})$ to the chemical potential from the Ewald summation is calculated by

$$\mu_i^{C,ew}(\mathbf{r})/k_B T = Z_i \Gamma \mathbf{FT}^{-1}\left[\frac{4\pi}{|\mathbf{k}|^2}\tilde{\rho}(\mathbf{k})\exp\left(-|\mathbf{k}|^2/4\alpha\right)\right], \tag{27}$$

where $\tilde{\rho}(\mathbf{k}) = \mathbf{FT}\left[\sum_j Z_j \rho_j(\mathbf{r})\right]$, $\mathbf{FT}$ and $\mathbf{FT}^{-1}$ are the Fourier and the inverse Fourier transformations. Since $1/|\mathbf{k}|^2$ is singular at $|\mathbf{k}| = 0$, $\tilde{\rho}(\mathbf{0})$ should be zero, *i.e.* the charge neutrality condition should be met. In an infinitely periodic system, the boundary condition at infinity affects the system free energy due to long-range Coulomb interactions and the resulting polarization energy should be considered [31]. Eq. (27) is valid for a system embedded in materials with infinite dielectric constant, *i.e.* metals. For a vacuum boundary condition, the polarization energy needs to be included and the chemical potential field and the free energy become

$$\mu_i^{C,ew'}(\mathbf{r})/k_B T = \mu_i^{C,ew}(\mathbf{r})/k_B T + \frac{4\pi Z_i \Gamma}{3V}\left(\sum_j Z_j \int d\mathbf{r}'\mathbf{r}'\rho_j(\mathbf{r}')\right)\cdot\mathbf{r} \tag{28}$$

and

$$F^{ex\prime} = F^{ex} + \frac{2\pi\Gamma}{3V}\left|\sum_i Z_i \int d\mathbf{r}\mathbf{r}\rho_i\left(\mathbf{r}\right)\right|^2 . \tag{29}$$

2.2.5. Single molecular partition function

Here we discuss the single molecular partition function, Q, for the discrete limit and the linear configuration of monomer species as shown in Fig. 2.2. The extension to the continuous monomer segments as in SCFTs and configurations other than linear is discussed in Section 2.2.6. Q is given by

$$Q = \int d\mathbf{r}_1 \cdots d\mathbf{r}_N K\left(\mathbf{r}_1, \cdots, \mathbf{r}_N\right) \exp\left\{-\sum_i^N w_i\left(\mathbf{r}_i\right)\right\}, \tag{30}$$

where K is the product of constraints between neighboring monomers

$$K\left(\mathbf{r}_1, \cdots, \mathbf{r}_N\right) = \prod_i^{N-1} P_i\left(\mathbf{r}_i, \mathbf{r}_{i+1}\right). \tag{31}$$

The bond length between neighboring monomers of polymers is usually approximated to follow a Gaussian distribution [45] and the constraint for the polymer configuration shown in Fig. 2.2A is given by

$$P_i(\mathbf{r},\mathbf{r}') = \left(\frac{3}{2\pi a_i^2}\right)^{3/2} \exp\left\{-\frac{3}{2a_i^2}(\mathbf{r}'-\mathbf{r})^2\right\}, \tag{32}$$

where a_i is the average distance between neighboring monomers, *i.e.* the Kuhn length. If the i th monomer is a HS as shown in Fig. 2.2B, the constraint is given by

$$P_i(\mathbf{r},\mathbf{r}') = \delta\left(|\mathbf{r}'-\mathbf{r}|-R\right)/4\pi R^2, \tag{33}$$

where R is the radius of the HS. To calculate Q, we introduce the segment distribution functions, $q_i(\mathbf{r})$ and $q_i^\dagger(\mathbf{r})$, defined as

$$q_{i+1}(\mathbf{r}) = \int d\mathbf{r}' G_i(\mathbf{r}',\mathbf{r}) q_i(\mathbf{r}') \tag{34}$$

and

$$q_i^\dagger(\mathbf{r}) = \int d\mathbf{r}' G_i(\mathbf{r},\mathbf{r}') q_{i+1}^\dagger(\mathbf{r}'), \tag{35}$$

where G_i is physically interpreted as the propagator from the i th monomer to the $i+1$ th one toward the right in Fig. 2.2. The propagator, G_i is given by

$$G_i(\mathbf{r},\mathbf{r}') = \exp\{-w_i(\mathbf{r})/2\} P_i(\mathbf{r},\mathbf{r}') \exp\{-w_{i+1}(\mathbf{r}')/2\}. \tag{36}$$

Eqs. (34) and (35) can be numerically obtained from convolution of the distribution functions, q and $q^\dagger$, respectively, with the propagator, G, if boundary conditions are given such as,

$$q_1(\mathbf{r}) = \exp\left\{-w_1(\mathbf{r})/2\right\} \tag{37}$$

and

$$q_N^\dagger(\mathbf{r}) = \exp\left\{-w_N(\mathbf{r})/2\right\}. \tag{38}$$

Therefore, the distribution functions, q and $q^\dagger$, are obtained from the chemical potential fields, w, as shown in Fig. 2.1. Finally, Q is given as

$$Q = \int d\mathbf{r} q_i(\mathbf{r}) q_i^\dagger(\mathbf{r}), \tag{39}$$

where i can be arbitrarily chosen, since Eq. (39) is equal to Eq. (30) regardless of i. Physically, $q_i(\mathbf{r})$ and $q_i^\dagger(\mathbf{r})$ have the meaning of distribution functions of species i propagated from the free ends, $i = 1$ and $i = N$, respectively. The density function of monomer species i is obtained from Eq. (10) with the condition, $DF/Dw_i(\mathbf{r}) = 0$, as

$$\rho_i(\mathbf{r}) = \frac{n}{Q} q_i(\mathbf{r}) q_i^{\dagger}(\mathbf{r}). \tag{40}$$

Although we only introduced two kinds of constraint functions, one for polymers in Eq. (32), and the other for hard particles in Eq. (33), this formulation can be generalized to other constraints such as the continuous-segments propagator relevant for SCFTs (see Section 2.2.6) as well as to other monomer species such as non-isotropic Janus NPs. Furthermore, the approach can be applied to the mixed case of continuous and discrete segments as needed for ligand-stabilized NPs [36]. Such flexibility in the choice of monomer species and constraints clearly highlights the advantages and versatility of the proposed approach compared with previous SCFT, SCFT/DFT, and other polymer DFT approaches [27, 46], and allows us to simulate complex multi-component systems.

2.2.6. Numerical implementation

Eqs. (34) and (35) can be numerically evaluated using the convolution theorem as

$$\begin{aligned} q_{i+1}(\mathbf{r}) &= \exp\left\{-w_{i+1}(\mathbf{r})/2\right\} \\ &\times \mathbf{FT}^{-1}\left[\tilde{P}_i(\mathbf{k})\mathbf{FT}\left[\exp\left\{-w_i(\mathbf{r})/2\right\} q_i(\mathbf{r})\right]\right] \end{aligned} \tag{41}$$

and

$$
\begin{aligned}
&q_i^{\dagger}(\mathbf{r}) = \exp\left\{-w_i(\mathbf{r})/2\right\} \\
&\times \mathbf{FT}^{-1}\left[\tilde{P}_i(-\mathbf{k})\mathbf{FT}\left[\exp\left\{-w_{i+1}(\mathbf{r})/2\right\}q_{i+1}^{\dagger}(\mathbf{r})\right]\right],
\end{aligned}
\tag{42}
$$

where $\tilde{P}_i(\mathbf{k}) = \mathbf{FT}\left[P_i(\mathbf{r})\right]$. However, in SCFTs, the propagator is modified for the continuous case and the parameter, i, becomes a continuous parameter. For clarity, we use s for the continuous parameter. The constraint function, $P_{i\leftrightarrow j}(\mathbf{r},\mathbf{r}')$, becomes

$$
P_{i\leftrightarrow j}(\mathbf{r},\mathbf{r}') \propto \exp\left\{-\int_i^j ds \frac{3}{2a^2(s)}\left(\frac{d\mathbf{r}}{ds}\right)^2\right\}
\tag{43}
$$

and the propagator is given by the path integral

$$
G_{i\leftrightarrow j}(\mathbf{r},\mathbf{r}') = \int \mathrm{D}\mathbf{r}'' \exp\left\{-\int_i^j ds\left[\frac{3}{2a^2(s)}\left(\frac{d\mathbf{r}''}{ds}\right)^2 + w_s(\mathbf{r}'')\right]\right\}
\tag{44}
$$

so that $q_s(\mathbf{r}) = \int d\mathbf{r}' G_{0\leftrightarrow s}(\mathbf{r}',\mathbf{r})$ and $q_s^{\dagger}(\mathbf{r}) = \int d\mathbf{r}' G_{s\leftrightarrow N}(\mathbf{r},\mathbf{r}')$. The molecular partition function Q can be obtained from $Q = \int d\mathbf{r} q_s(\mathbf{r}) q_s^{\dagger}(\mathbf{r})$, where s has any value between 0 and N. From the boundary conditions, $q_0(\mathbf{r}) = 1$ and $q_N^{\dagger}(\mathbf{r}) = 1$, one can obtain $q_s(\mathbf{r})$ and $q_s^{\dagger}(\mathbf{r})$ from the modified diffusion equations [20-21, 45, 47-49]

$$\frac{\partial q_s(\mathbf{r})}{\partial s} = \left\{ \frac{a(s)^2}{6} \nabla^2 - w_s(\mathbf{r}) \right\} q_s(\mathbf{r}) \tag{45}$$

and

$$-\frac{\partial q_s^\dagger(\mathbf{r})}{\partial s} = \left\{ \frac{a(s)^2}{6} \nabla^2 - w_s(\mathbf{r}) \right\} q_s^\dagger(\mathbf{r}). \tag{46}$$

In this work, we utilize this functional form in order to account for the conformational entropy of polymers and ligands. Solving the diffusion equation is usually the most time consuming step in the iterations. The computation time required for the calculation is proportional to M^2, where M is the number of spatial grid points. Matsen *et al.* proposed a spectral method where $q_s(\mathbf{r})$ and $q_s^\dagger(\mathbf{r})$ are a linear combination of symmetry-adopted basis functions [20]. The method reduces the computational load dramatically but requires knowledge of the exact symmetry of the expected morphologies. Alternatively, the real space approach doesn't need such information and structures are obtained without any restriction of symmetry [19] but then the computational cost of calculating the partition function becomes extremely large. We adopt the real space approach but minimize the computational effort by implementing a recently developed algorithm, called the 'split step algorithm' [49], which extensively utilizes the Fast Fourier Transform (FFT). The basic scheme is given as

$$
\begin{aligned}
q_{s+ds}\left(\mathbf{r}\right) = \exp\left\{-\frac{ds}{2}w_s\left(\mathbf{r}\right)\right\}\exp\left[\frac{a^2}{6}ds\nabla^2\right] \\
\times\exp\left\{-\frac{ds}{2}w_s\left(\mathbf{r}\right)\right\}q_s\left(\mathbf{r}\right)
\end{aligned}
\tag{47}
$$

and

$$
\begin{aligned}
q^{\dagger}_{s-ds}\left(\mathbf{r}\right) = \exp\left\{-\frac{ds}{2}w_s\left(\mathbf{r}\right)\right\}\exp\left[\frac{a^2}{6}ds\nabla^2\right] \\
\times\exp\left\{-\frac{ds}{2}w_s\left(\mathbf{r}\right)\right\}q^{\dagger}_s\left(\mathbf{r}\right)
\end{aligned}
.
\tag{48}
$$

These equations can be numerically implemented as

$$
\begin{aligned}
q_{s+ds}\left(\mathbf{r}\right) = \exp\left\{-\frac{ds}{2}w_s\left(\mathbf{r}\right)\right\} \\
\times\mathbf{FT}^{-1}\left[\exp\left\{-\frac{a\left(s\right)^2}{6}ds\left|\mathbf{k}\right|^2\right\}\mathbf{FT}\left[\exp\left\{-\frac{ds}{2}w_s\left(\mathbf{r}\right)\right\}q_s\left(\mathbf{r}\right)\right]\right]
\end{aligned}
\tag{49}
$$

and

$$
\begin{aligned}
q^{\dagger}_{s-ds}\left(\mathbf{r}\right) = \exp\left\{-\frac{ds}{2}w_s\left(\mathbf{r}\right)\right\} \\
\times\mathbf{FT}^{-1}\left[\exp\left\{-\frac{a\left(s\right)^2}{6}ds\left|\mathbf{k}\right|^2\right\}\mathbf{FT}\left[\exp\left\{-\frac{ds}{2}w_s\left(\mathbf{r}\right)\right\}q^{\dagger}_s\left(\mathbf{r}\right)\right]\right]
\end{aligned}
\tag{50}
$$

(note that Eq. (49) is identical to Eq. (41), if the constraint function is given by Eq. (32)). Up to now, we have limited the discussion to the case of chains with a linear configuration. The extension to more complex configurations is identical to that reported for other polymer systems such as branched polymers [47-48] and is not repeated here. Since, in our work, monomer species can be soft molecules and hard molecules, multi-component molecular structures can be readily described by defining the monomer-monomer connectivity and specifying monomers with a parameter, i or s.

We adapted a numerical algorithm called the combinatorial screening technique by Drolet *et al.* [19] to iteratively solve Eqs. (8), (39), (34), (35), (40), and (14). The algorithm is illustrated in Fig. 2.1 and operates as follows. In the first step, we generate trial configurations of all species, $\rho(\mathbf{r})$, and obtain $w(\mathbf{r})$ from $\rho(\mathbf{r})$ using Eqs. (8) and (14). In the next step, new $\rho(\mathbf{r})$ are calculated from $w(\mathbf{r})$ of the previous step using Eqs. (39), (34), (35), and (40). Following this way, each step generates values for $w(\mathbf{r})$ and $\rho(\mathbf{r})$ from results of the previous step. This process is iterated until changes of $\rho(\mathbf{r})$ and $w(\mathbf{r})$ become sufficiently small. Since the free energy strongly depends on the box dimensions, we also minimize the system's free energy by varying the system size between iterations [14]. This procedure yields different solutions depending on the initial configurations. Thus, we perform these calculations with various initial configurations and choose the solution with the lowest free energy as the likely equilibrium phase.

2.2.7. Beyond the mean-field approximation

As shown in the previous sections, the numerical implementation is drastically simplified by the mean-field approximation, which is generally accurate for dense molecular systems. By limiting configurations to saddle points, the mean-field approximation greatly reduces the numerical complexity of the calculations. However, to properly describe dilute systems composed of small molecules, for example, a more advanced approach than the mean-field approach is required. In general, the chemical fields, w, and density functions, ρ, are complex (noting that w in Eq. (14) is a real function due to the mean-field approximation, see also relevant discussions in Refs. [50-51]). Therefore, they cannot be calculated with the numerical procedure given in Section 2.2.6. For such calculations, Ganesan *et al.* applied a complex Langevin dynamics for thermodynamic sampling [50-51]. We expect that such sampling method can be applied to our approach, since DFTs do not assume the mean-field approximation. Validation of these ideas is left for future work.

2.3. Simulation Results

2.3.1 HS Particle Behavior within BCPs

To test our theory for HS interactions, we compare our 1-dimensional predictions with the results obtained by Thompson *et al.* [28] using the DFT approach by Tarazona [52] for the same parameters. In this study, BCP composition is set to $f_A = 0.35$ and a typical value of 0.4655 is assigned for $N\rho_0^{-1}R_g^{-3}$, a parameter that specifies the volume of BCP relative to that of NPs. The radius of gyration of unperturbed BCPs, R_g, is the basic length unit in this work. The Flory-Huggins χN parameters are summarized in Table 2.1. We utilize the original form of the FMT approach and its hyper-netted chain (HNC) approximation form [33, 39, 42], so that the $\mu_i^{HS}(\mathbf{r})/k_BT$ term in Eq. (14) becomes $-\sum_j \int d\mathbf{r}' C_{ij}^{HS}(\mathbf{r},\mathbf{r}')\rho_j(\mathbf{r}')$, where $C_{ij}^{HS}(\mathbf{r},\mathbf{r}')$ is the direct correlation function of the excess HS interaction free energy functional [39]. We examine two cases: large NPs, $R_p = 0.735\ R_g\ (= 0.3\ R_0)$, with a small volume fraction, $\phi_p = 0.03$ (Fig. 2.3A), and small NPs, $R_p = 0.490\ R_g\ (= 0.2\ R_0)$, with an intermediate volume fraction $\phi_p = 0.15$ (Fig. 2.3B), where R_0 is the unperturbed chain end-to-end distance of BCPs equal to $\sqrt{6}R_g$. For the case near the dilute limit, $\phi_p = 0.03$, all of the DFT approaches yield consistent results as shown in Fig. 2.3A. This is expected because both, the DFT by Tarazona [52] as well as the FMT approach, utilize virial expansions of the excess chemical potential corresponding to pair exclusions at the dilute limit, and the HNC approximation is generally accurate if the density functional has small deviations from the reference state [33, 39, 52]. However, at the intermediate volume fraction of NPs, $\phi_p = 0.15$, shown in Fig. 2.3B, the results given by Thompson *et al.* [28] are in between those of the FMT and its HNC approximation form in terms of its shape and lamellar spacing. Compared with the FMT approach, the HS interactions of the DFT method by Tarazona [52] and HNC approximation are more repulsive. The discrepancy originates from the different functional forms of the excess free energy for HS interactions. A detailed discussion for those approaches can be found in Refs.

[41-42].

2.3.2. Binary Mixture of Charged HS Particles near a Charged Hard Wall

To benchmark the accuracy of HS and Coulomb interactions in our approach, we calculate the double layer formation of HS particles with opposite charge to the surface charge of a hard wall and compare to results of previous simulations [53-54]. We study a binary mixture of charged HS particles near a charged hard wall. We add positively $(+)$ and negatively $(-)$ charged HS particles near a positively charged flat wall. The charges are fixed at $Z_+ = 1$ and $Z_- = -1$, and the Bjerrum length is set to $\Gamma = 19.8145\ d_0$ for the Coulomb potential, $\Phi(\mathbf{r}) / k_B T = \Gamma Z_i Z_j / |\mathbf{r}|$, where d_0 is the diameter of particles and the basic length unit in these simulations. The overall volume fractions of particles are set to $\phi_+ = 0.0462$ and $\phi_- = 0.0462$. The surface charge densities are given by $\sigma^* = 0.25$, 0.42, 0.55, and $0.7\ d_0^{-2}$. Figure 2.4 shows the formation of the double layer formation of negatively charged HS particles at high surface charge densities. This is consistent with previous exact Monte Carlo simulations for $\sigma^* = 0.7\ d_0^{-2}$, shown as the open red circles in Fig. 2.4 [53]. Results are further compared to a previous DFT study [55] that used the same surface charge densities, shown in the inset of Fig. 2.4. Our 1-dimensional simulation results correctly predict the position of the correlation peak but overestimate the particle density relative to the exact Monte Carlo simulation data. Deviations between these simulation and theoretical results are expected and are due to the different levels of approximations involved. The deviations between the predictions of the two theories arise from the different functional forms adopted for HS and long-range Coulomb interactions.

2.3.3. Self-assembly of two chemically distinct HS particles connected by a homopolymer molecule within BCPs

As an example of the Green function propagator for the mixed case of the continuous and discrete segments, we introduce two chemically distinct HS particles, p1 and p2, connected with a homopolymer, H, as well as A-B di-BCPs. We want to determine how the HS particle distribution in the A and B regions of the di-BCP depends on the length of the homopolymer H. For this molecule, the single molecular partition function is given by

$$\begin{aligned} Q \equiv & \int d\mathbf{r}_{p1} \exp\left\{-w_{p1}\left(\mathbf{r}_{p1}\right)\right\} \int d\mathbf{r}_0 d\mathbf{r}_{N_h} \frac{\delta\left(\left|\mathbf{r}_{p1}-\mathbf{r}_0\right|-R\right)}{4\pi R^2} G_H\left(\mathbf{r}_0, \mathbf{r}_{N_h}\right) \\ & \times \int d\mathbf{r}_{p2} \frac{\delta\left(\left|\mathbf{r}_{N_h}-\mathbf{r}_{p2}\right|-R\right)}{4\pi R^2} \exp\left\{-w_{p2}\left(\mathbf{r}_{p2}\right)\right\} \end{aligned} . \qquad (51)$$

where G_H is the continuous propagator for the homopolymer H defined by Eq. (44). To obtain Q, we introduce the segment distribution functions, $q_i(\mathbf{r})$ and $q_i^\dagger(\mathbf{r})$ in Eqs. (34) and (35). The numerical calculation is performed using the equations,

$$q_{p1} = \exp\left\{-w_{p1}(\mathbf{r})\right\} \qquad (52)$$

and

$$q_0(\mathbf{r}) = \mathbf{FT}^{-1}\left[\tilde{\delta}(\mathbf{k})\mathbf{FT}\left[q_{p1}(\mathbf{r})\right]\right], \tag{53}$$

where $\tilde{\delta}(\mathbf{k}) = \mathbf{FT}\left[\delta(|\mathbf{r}| - R)/4\pi R^2\right]$ and $q_0(\mathbf{r})$ is the segment distribution function of one end of the homopolymer propagated from the particle p1. The segment distribution functions of the homopolymer from $q_0(\mathbf{r})$ to $q_{N_h}(\mathbf{r})$ are calculated utilizing Eq. (45). The segment distribution $q_{p2}(\mathbf{r})$ is obtained from

$$q_{p2}(\mathbf{r}) = \exp\left\{-w_{p2}(\mathbf{r})\right\}\mathbf{FT}^{-1}\left[\tilde{\delta}(\mathbf{k})\mathbf{FT}\left[q_{N_h}(\mathbf{r})\right]\right]. \tag{54}$$

and the $q_i^{\dagger}(\mathbf{r})$ for the opposite direction from p2 to p1 are obtained using the same equations by replacing p1 with p2. To segregate p1 HS particle into block A and the p2 HS particle into block B, we set the χN parameters as shown in Table 2.2 (noting that for this simulation the χN parameters between the homopolymer and the two blocks were set equal to zero in order to clearly monitor the homopolymer size dependence). The radii of HS particles are fixed at $R_{p1} = R_{p2} = 0.735\ R_g$, *i.e.* identical to the simulation described in Fig. 2.3A for single NPs in only one block and the overall volume fraction of p1 and p2 particles in the system is set to $\phi_{p1} = \phi_{p2} = 0.03$. We assign a typical value of 0.4655 for $N\rho_0^{-1}R_g^{-3}$. For comparison, Fig. 2.4A shows the results of the simulations for HS particles without homopolymers. When a long homopolymer with the size, $N_h / N = 0.5$, bridges two HS particles, the HS particles are slightly segregated to the edge of the blocks, *i.e.* towards the interface. In case of a short homopolymer bridge, $N_h / N = 0.1$, the segregation becomes significantly more pronounced. These results are physically reasonable, since shorter homopolymers are expected to bring two HS particles closer due to the smaller end-to-end chain length.

2.3.4. Ligand-stabilized NP / BCP self-assembly: bead-spring model of polymers and charged ligand effect on NP self-assembly behavior

In order to demonstrate flexibility of our methodology for incorporating complex molecular structures and interactions, we introduce NPs with charged ligands and BCPs represented by a bead-spring model where the BCP monomers have a hard-sphere core as shown in Fig. 2.6A. Firstly, we compare our bead-spring model with a comparable model system without hard-sphere cores, for which the system parameters are set to $f_A = 0.4$ and $\chi_{AB}N = 45$. For the hard spheres BCPs, A and B, we chose $N_A = 40$ and $N_B = 60$, equivalent to $f_A = 0.4$. The radius of a monomer is set to $R = 0.106R_g$, where $R_g = \sqrt{Na^2 / 6}$ and a is the Kuhn length set to $a = 0.245R_g$. The short-range interaction parameter is given by $\chi_{AB} / (4\pi R^3 / 3) = 80$ and the overall system volume fraction is given by 0.4. Fig. 2.6B shows the normalized volume fractions of monomers A and B. The overall shape of the lamellar self-assembly behavior is very similar. However, compared with SCFT, the bead-spring model of BCPs yields a larger lamellar spacing. This is due to the more extended conformations of the polymers represented by the bead-spring model arising from excluded volume interactions between monomer units, compared to those for unperturbed polymer models, as expected theoretically [45]. Having established our bead-spring model, we add NPs with charged ligands and counter anions (CAs) satisfying the charge neutrality condition. The overall volume fraction of ligand-stabilized NPs and CAs is set to 0.08, while the value of BCPs is set to 0.32. The radius of NPs is given by $R_{NP} = 0.530$ and the number of ligands per NP is set to $n_{Ligand} = 20$. The ligands are composed of 5 HSs with the radius equal to that of the BCP monomers and the terminal HSs have a positive charge $Z_{+} = 1$ as shown in Fig. 2.7A. CAs have a negative charge $Z_{-} = -1$. As discussed in Section 2.2.4, the boundary condition at infinity affects the overall system energy in case of the long-range Coulomb potential. In our simulation, the vacuum boundary condition was assumed. The interaction parameters are summarized in Table 2.3. The single molecular partition function of the ligand-stabilized NPs shown in Fig. 2.7A is given by

$$Q \equiv \int d\mathbf{r}_{NP} \exp\left\{-w_{NP}\left(\mathbf{r}_{NP}\right)\right\}\left[\int d\mathbf{r}_i d\mathbf{r}_{N_{Ligand}} \frac{\delta\left(\left|\mathbf{r}_{NP}-\mathbf{r}_i\right|-R_{NP}-R\right)}{4\pi\left(R_{NP}+R\right)} G_{Ligand}\left(\mathbf{r}_i,\mathbf{r}_{N_{Ligand}}\right)\right]^{n_{Ligand}}, \tag{55}$$

where $G_{Ligand}\left(\mathbf{r}_i,\mathbf{r}_{N_{Ligand}}\right)$ is the propagator from one ligand chain end i to the other end N_{Ligand}. The first step is to obtain $q_i^{\dagger}\left(\mathbf{r}\right)$ for the ligand monomer i in Fig.

2.7A from the boundary condition, $q^{\dagger}_{N_{Ligand}}(\mathbf{r}) = \exp\left\{-w_{N_{Ligand}}(\mathbf{r})/2\right\}$ using Eq. (36) with the Gaussian constraint given in Eq. (32). Then $q^{\dagger}_{NP}(\mathbf{r})$, $q_{NP}(\mathbf{r})$, and $q_i(\mathbf{r})$ are calculated using the following equations,

$$q^{\dagger}_{NP}(\mathbf{r}) = \exp\left\{-w_{NP}(\mathbf{r})/2\right\}\left\{\mathbf{FT}^{-1}\left[\tilde{\delta}(\mathbf{k})\mathbf{FT}\left[q^{\dagger}_{i}(\mathbf{r})\right]\right]\right\}, \tag{56}$$

$$q_{NP}(\mathbf{r}) = \exp\left\{-w_{NP}(\mathbf{r})/2\right\}\mathbf{FT}^{-1}\left[\tilde{\delta}(\mathbf{k})\mathbf{FT}\left[q^{\dagger}_{i}(\mathbf{r})\right]\right]^{n_{Ligand}-1}, \tag{57}$$

and

$$q_i(\mathbf{r}) = \exp\left\{-w_i(\mathbf{r})/2\right\}\mathbf{FT}^{-1}\left[\tilde{\delta}(\mathbf{k})\mathbf{FT}\left[q_{NP}(\mathbf{r})\right]\right], \tag{58}$$

where $\tilde{\delta}(\mathbf{k}) = \mathbf{FT}\left[\delta\left(|\mathbf{r}| - R_{NP} - R\right)/4\pi\left(R_{NP}+R\right)^2\right]$. Finally, other ligand components, $q_{i+1}\cdots q_{N_{Ligand}}$, can be calculated using Eq. (36) with the Gaussian constraint. Two different conditions are studied: (i) no Coulomb interactions, *i.e.* $\Gamma = 0$ and (ii) Coulomb interaction with $\Gamma = 7.0R_g$, which corresponds to a typical dielectric constant of a polymeric materials with $R_g = 5\ nm$ at room temperature of $\varepsilon_r = 20$. In the absence of Coulomb interactions ($\Gamma = 0$), NPs are highly localized within block A as shown in Fig. 2.7B due to a very weak entropic driving force of mixing (noting that the volume ratio of NPs to BCPs is 2.25). When the Coulomb potential is applied by setting $\Gamma = 7.0R_g$, the NP-NP repulsion forces become stronger and NPs are more dispersed (compare Fig. 2.7D and 2.7E). Such repulsive interactions between ligands can lead to an enhanced dispersion of NPs when they are mixed with BCPs [13, 58]. The density profile of CAs are shown in Fig. 2.7F and Fig. 2.7G. Due to the long-range Coulomb interactions, CAs and NPs form an ordered structure where CAs localize between NPs to screen the Coulombic repulsive force among NPs. Such ordered NP localization in BCPs has not been experimentally observed to date and is intriguing. Future work will include a full study of this phenomenon.

2.4. Conclusion

We presented a theoretical framework that unifies polymer self-consistent field theory and density functional theory that incorporates the complexity of hybrid molecular structures and their interactions. The Green function propagator was extended to hard particles for describing multi-component molecules composed of soft and hard chemical species. Furthermore, direct correlation functions used in DFTs were utilized to describe key physical interactions including long-range Coulomb and HS interactions. To validate our approach, we compared our results with two previous simulation studies: (i) the NP segregation behavior within BCPs and (ii) the double layer formation of charged HS particles near a charged wall. In both cases, we obtained good agreement with previously reported results on these systems. We then applied our approach to demonstrate the self-assembly of two chemically distinct NPs connected by a polymer molecule within the phase-separated BCPs. Finally, we investigated a model system for the self-assembly of BCPs and NPs with charged ligands. Due to sampling efficiency of phase space and descriptive power of molecular structures and interactions, we expect that our approach will vastly improve our ability to simulate large complex systems without loss of molecular details. Our approach is based on the mean-field approximation. To overcome the limitations of the mean-field approximation such as the neglect of thermal fluctuations, we expect that our method can be combined with a recent field theoretic approach[50] that goes beyond the mean-field approximation. Future research will include systems with dipole interactions between NPs and various polymeric systems with unique architectures.

Acknowledgements

We gratefully acknowledge support by the KAUST-Cornell (KAUST-CU) Center for Energy and Sustainability. The calculations have been performed using computational resources of the Computational Center for Nanotechnology Innovation (CCNI) at Rensselaer Polytechnic Institute.

TABLE 2.1. Flory-Huggins χN parameters for the simulation of HS particle self-assembly within BCPs.

χN	B	P
A	20	0
B		20

TABLE 2.2. Flory-Huggins χN parameters for the simulation of self-assembly of two chemically distinct HS particles connected by a homopolymer molecule within BCPs

χN	B	p1	p2	H
A	20	0	20	0
B		20	0	0
p1			20	0
p2				0

TABLE 2.3. Flory-Huggins χ parameters for the self-assembly of BCPs and NPs with charged ligands

$\chi / (4\pi R^3 / 3)$	B	NP	Ligand	CA
A	80	0	0	0
B		80	80	80
NP			0	0
Ligands				0

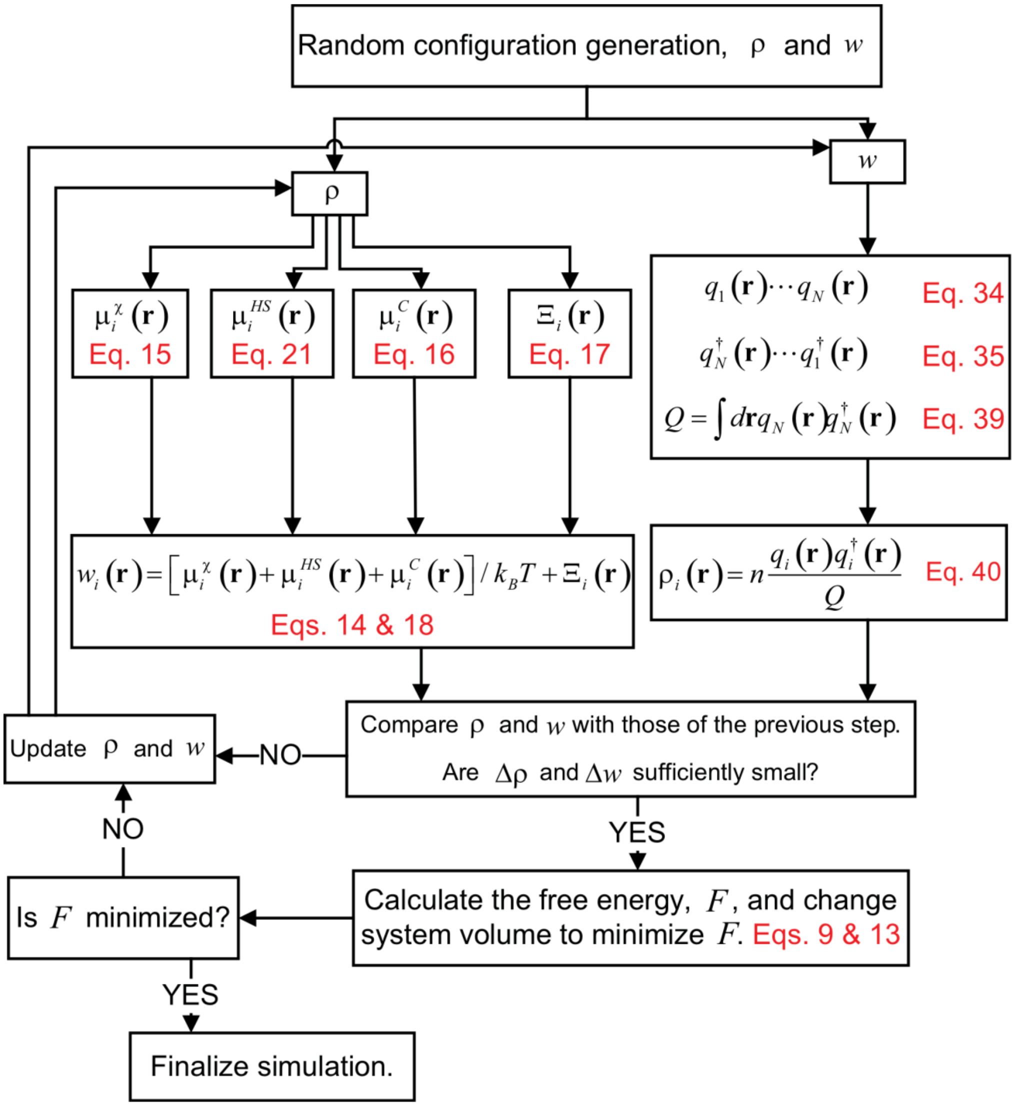

Figure 2.1. The general schematic procedure and key equations of the present approach for a homogeneous system of n molecules composed of N monomers specified as i.

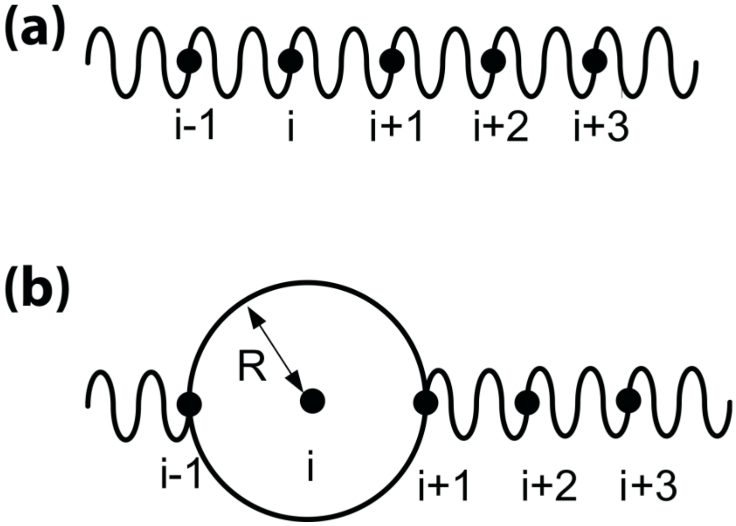

Figure 2.2. Multi-component molecule representations with the linear configuration for **(a)** flexible monomers and **(b)** HS particles with flexible molecules

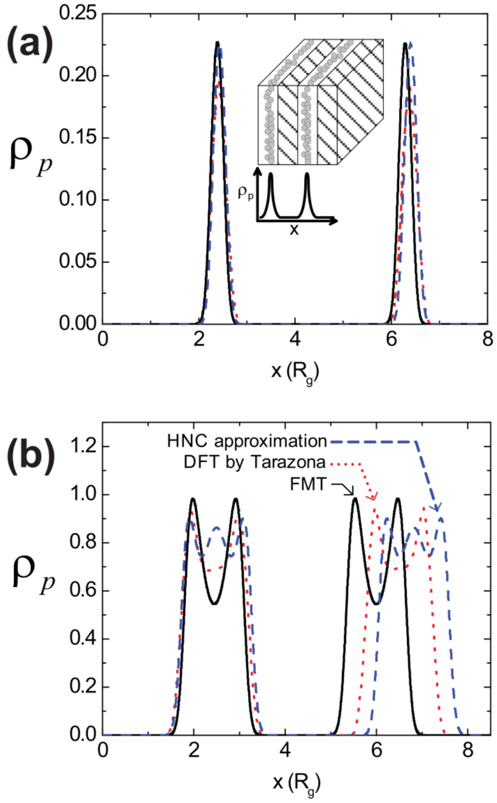

Figure 2.3. Comparison of particle density profiles, ρ_p, in the lamellar morphology of BCP/NP self-assembly varying the excess HS free energy functional. We verify our approach by comparing with results of previous calculations [28]. Black solid lines are results applying the FMT, blue dashed lines results from the HNC approximation form of the FMT, and red dotted lines results from applying the DFT by Tarazona, see Ref. [28]. **(a)** Large particles at the dilute condition ($R_p = 0.735\ R_g$, $\phi_p = 0.03$). **(b)** Small particles with intermediate volume fraction ($R_p = 0.490\ R_g$, $\phi_p = 0.15$). Compared with the FMT approach, the HS interactions of the DFT approach by Tarazona [52] and HNC approximation are more repulsive. The discrepancy originates from different functional forms of the excess free energy for HS interactions.

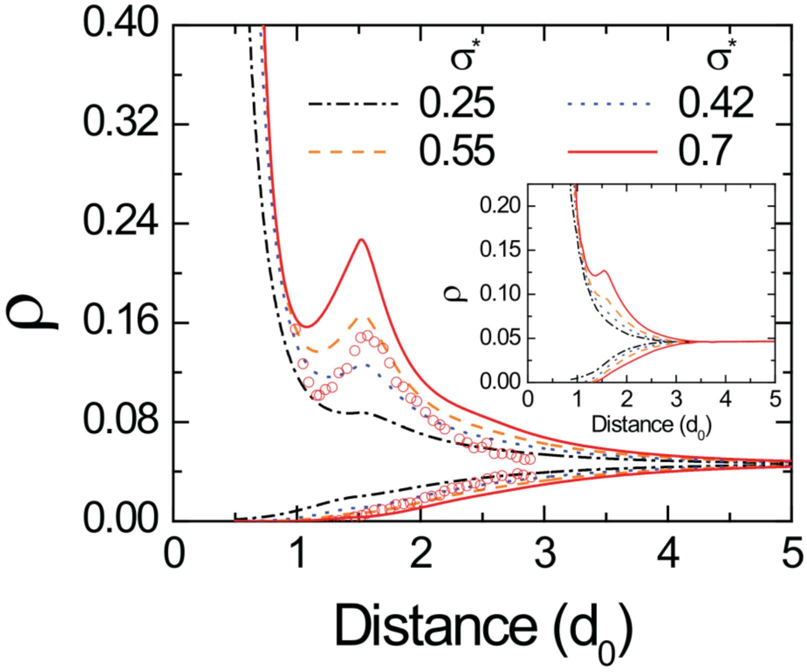

Figure 2.4. Density profiles of positively charged, ρ_+, and negatively charged HS particles, ρ_-, as a function of distance from a positively charged flat wall with different surface charge densities, $\sigma^* = 0.25$, 0.42, 0.55, and $0.7\ d_0^{-2}$ (bottom to top for ρ_- and top to bottom for ρ_+), where d_0 is the diameter of HS particles. Open red circles are Monte Carlo simulation results of Ballone *et al*. at $\sigma^* = 0.7\ d_0^{-2}$ [53]. The inset displays results from R. Groot [55]. The double layer formation is observed at high surface charge densities.

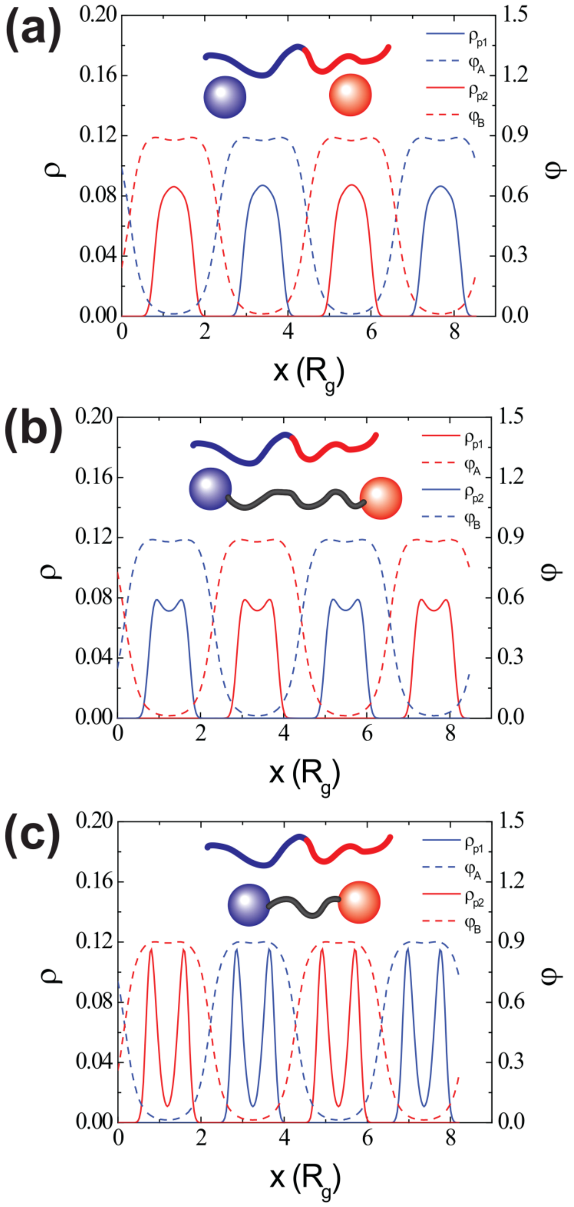

Figure 2.5. Density profiles of NPs, ρ, and local volume fractions of BCPs, φ. The solid blue lines depict ρ of the p1-type NPs and the solid red lines show ρ of the p2-type NPs. The dotted blue lines represent φ of block A and the red lines show φ of block B. **(a)** Free NPs. **(b,c)** NPs connected by a homopolymer molecule with size **(b)** $N_h / N = 0.5$ and **(c)** $N_h / N = 0.1$.

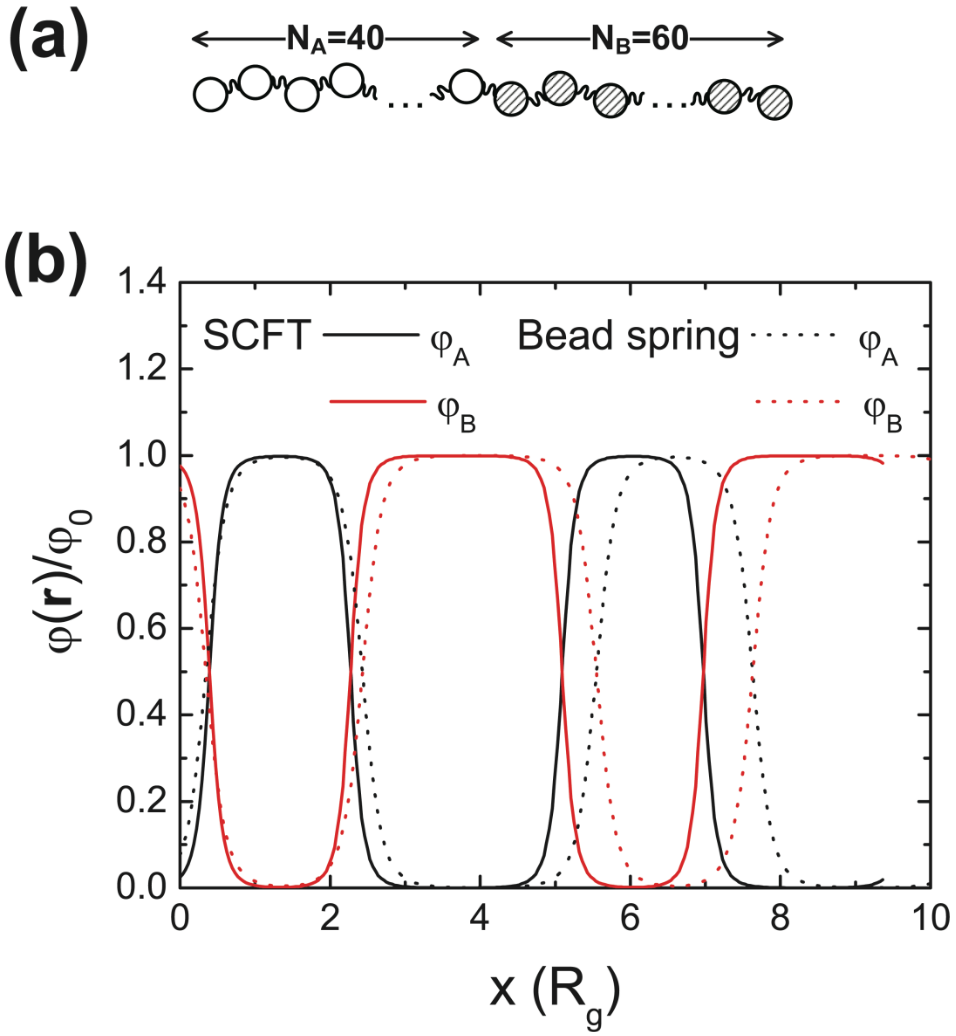

Figure 2.6. Comparison of the bead-spring model and SCFT. The bead-spring model exhibits a larger lamellar spacing due to excluded volume interactions between monomer units. **(a)** Illustration of the bead-spring representation of a BCP. **(b)** Normalized local volume fractions of block A (black) and block B (red). The solid lines are results of SCFT and the dotted lines are those of the bead-spring model.

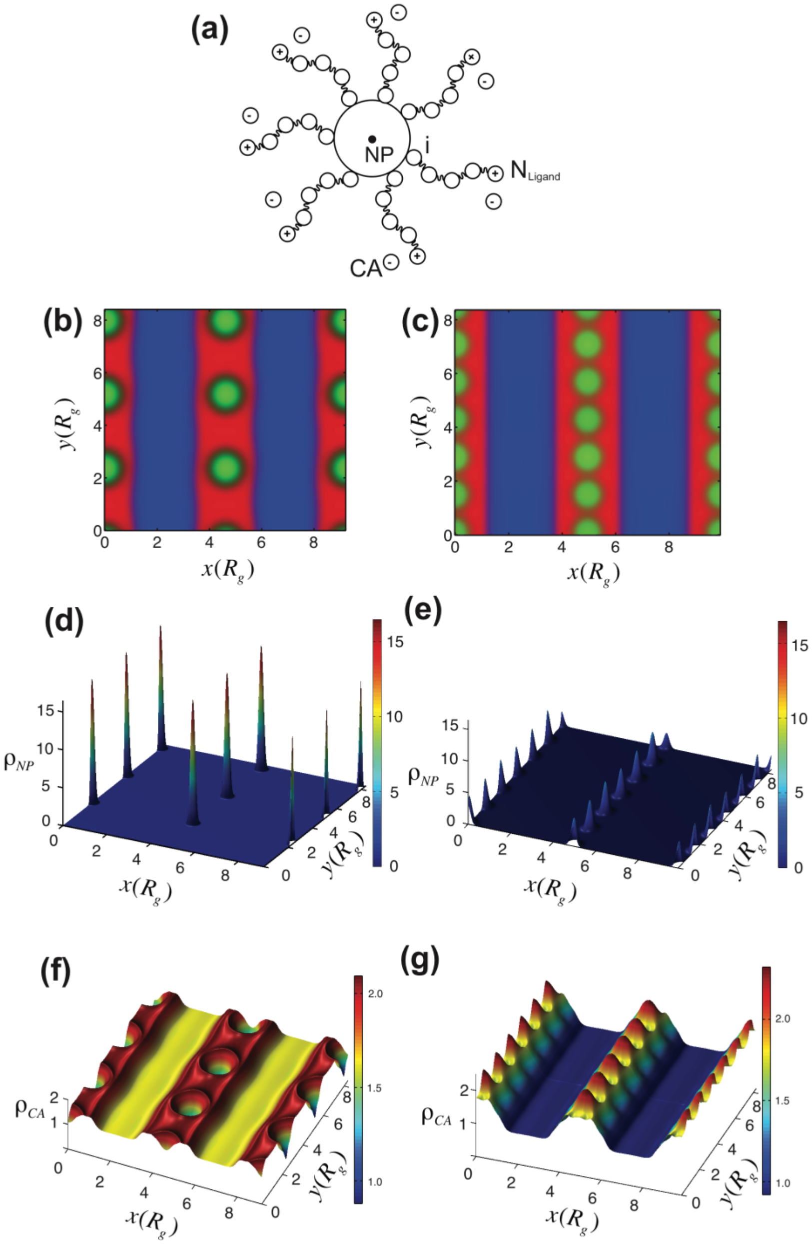

Figure 2.7. Self-assembly of BCPs, NPs with charged ligands, and CAs, illustrating the effect of NP Coulomb repulsions on enhancing the regular dispersion of NPs. **(a)** Illustration of NPs with charged ligands and CAs. **(b,c)** Red color represents block A, blue color block B, and green color NPs with ligands. Density profiles of **(d,e)** NPs and **(f,g)** CAs. Two different conditions are studied by varying the parameter Γ:

(b,d,f) $\Gamma = 0$, **(c,e,g)** $\Gamma = 7.0 R_g$.

REFERENCES

[1] D. J. Norris, A. L. Efros, and S. C. Erwin, *Science* **319** (5871), 1776 (2008).

[2] T. Hyeon, S. S. Lee, J. Park, Y. Chung, and H. B. Na, *J. Am. Chem. Soc.* **123** (51), 12798 (2001).

[3] V. F. Puntes, K. M. Krishnan, and A. P. Alivisatos, *Science* **291** (5511), 2115 (2001).

[4] H. Zheng, R. K. Smith, Y.-w. Jun, C. Kisielowski, U. Dahmen, and A. P. Alivisatos, *Science* **324** (5932), 1309 (2009).

[5] M. L. Steigerwald, A. P. Alivisatos, J. M. Gibson, T. D. Harris, R. Kortan, A. J. Muller, A. M. Thayer, T. M. Duncan, D. C. Douglass, and L. E. Brus, *J. Am. Chem. Soc.* **110** (10), 3046 (1988).

[6] I. Gur, N. A. Fromer, M. L. Geier, and A. P. Alivisatos, *Science* **310** (5747), 462 (2005).

[7] F. X. Redl, K. S. Cho, C. B. Murray, and S. O'Brien, *Nature* **423** (6943), 968 (2003).

[8] E. V. Shevchenko, D. V. Talapin, N. A. Kotov, S. O'Brien, and C. B. Murray, *Nature* **439** (7072), 55 (2006).

[9] M. A. Noginov, G. Zhu, A. M. Belgrave, R. Bakker, V. M. Shalaev, E. E. Narimanov, S. Stout, E. Herz, T. Suteewong, and U. Wiesner, *Nature* **460** (7259), 1110 (2009).

[10] D. Gebauer, A. Volkel, and H. Colfen, *Science* **322** (5909), 1819 (2008).

[11] E. M. Pouget, P. H. H. Bomans, J. A. C. M. Goos, P. M. Frederik, G. de With, and N. A. J. M. Sommerdijk, *Science* **323** (5920), 1455 (2009).

[12] S. C. Warren, F. J. DiSalvo, and U. Wiesner, *Nature Mater.* **6** (2), 156 (2007).

[13] S. C. Warren, L. C. Messina, L. S. Slaughter, M. Kamperman, Q. Zhou, S. M. Gruner, F. J. DiSalvo, and U. Wiesner, *Science* **320** (5884), 1748 (2008).

[14] Y. Bohbot-Raviv and Z.-G. Wang, *Phys. Rev. Lett.* **85** (16), 3428 (2000).

[15] F. J. Martínez-Veracoechea and F. A. Escobedo, *Macromolecules* **42** (5), 1775 (2009).

[16] F. J. Martínez-Veracoechea and F. A. Escobedo, *Macromolecules* **40** (20), 7354 (2007).

[17] F. J. Martínez-Veracoechea and F. A. Escobedo, *J. Chem. Phys.* **125** (10), 104907 (2006).

[18] T. Dotera, *Phys. Rev. Lett.* **89** (20), 205502 (2002).

[19] F. i. Drolet and G. H. Fredrickson, *Phys. Rev. Lett.* **83** (21), 4317 (1999).

[20] M. W. Matsen and M. Schick, *Phys. Rev. Lett.* **72** (16), 2660 (1994).

[21] E. Helfand, *J. Chem. Phys.* **62** (3), 999 (1975).

[22] C. A. Tyler, J. Qin, F. S. Bates, and D. C. Morse, *Macromolecules* **40** (13), 4654 (2007).

[23] Z. Guo, G. Zhang, F. Qiu, H. Zhang, Y. Yang, and A.-C. Shi, *Phys. Rev. Lett.* **101** (2), 028301 (2008).

[24] S. W. Sides, B. J. Kim, E. J. Kramer, and G. H. Fredrickson, *Phys. Rev. Lett.* **96** (25), 250601 (2006).

[25] A. Bymaster, S. Jain, and W. G. Chapman, *J. Chem. Phys.* **128** (16), 164910 (2008).

[26] S. Jain, P. Jog, J. Weinhold, R. Srivastava, and W. G. Chapman, *J. Chem. Phys.*

128 (15), 154910 (2008).

[27] S. Tripathi and W. G. Chapman, *Phys. Rev. Lett.* **94** (8), 087801 (2005).

[28] R. B. Thompson, V. V. Ginzburg, M. W. Matsen, and A. C. Balazs, *Science* **292** (5526), 2469 (2001).

[29] R. B. Thompson, V. V. Ginzburg, M. W. Matsen, and A. C. Balazs, *Macromolecules* **35** (3), 1060 (2002).

[30] L. Zhang, J. Lin, and S. Lin, *Macromolecules* **40** (15), 5582 (2007).

[31] D. Frenkel and B. Smit, *Understanding molecular simulation : from algorithms to applications*, 2nd ed. (Academic Press, San Diego, 2002).

[32] K. Hiroike, *Mol. Phys.* **33** (4), 1195 (1977).

[33] Y. Rosenfeld, *J. Chem. Phys.* **98** (10), 8126 (1993).

[34] Y. Rosenfeld and L. Blum, *J. Chem. Phys.* **85** (3), 1556 (1986).

[35] S. M. Foiles and N. W. Ashcroft, *J. Chem. Phys.* **75** (7), 3594 (1981).

[36] K. Hur, R. G. Hennig, F. Escobedo, and U. Wiesner, *Nano Lett.* **12** (6), 3218-3223 (2012).

[37] K. M. Hong and J. Noolandi, *Macromolecules* **14** (3), 727 (1981).

[38] G. H. Fredrickson, *Soft Matter* **3** (11), 1329 (2007).

[39] Y. Rosenfeld, *Phys. Rev. Lett.* **63** (9), 980 (1989).

[40] J. K. Percus, *J. of Stat. Phys.* **15** (6), 505 (1976).

[41] P. Tarazona, J. A. Cuesta, and Y. Martinez-Raton, *Lect. Notes Phys*. **753**, 247 (2008).

[42] J. P. Hansen and I. R. McDonald, *Theory of simple liquids*, 2nd. ed. (Academic Press, London ; Orlando, 1986).

[43] L. Blum, *Mol. Phys.* **30** (5), 1529 (1975).

[44] L. Blum and Y. Rosenfeld, *J. of Stat. Phys.* **63** (5-6), 1177 (1991).

[45] M. Doi and S. F. Edwards, *The theory of polymer dynamics*. (Clarendon Press ; Oxford University Press, Oxford [Oxfordshire] New York, 1986).

[46] Y.-X. Yu and J. Wu, *J. Chem. Phys.* **117** (5), 2368 (2002).

[47] G. M. Grason, B. A. DiDonna, and R. D. Kamien, *Phys. Rev. Lett.* **91** (5), 058304 (2003).

[48] G. M. Grason and R. D. Kamien, *Phys. Rev. E* **71** (5), 051801 (2005).

[49] G. Tzeremes, K. Rasmussen, T. Lookman, and A. Saxena, *Phys. Rev. E* **65** (4), 041806 (2002).

[50] G. H. Fredrickson, V. Ganesan, and F. Drolet, *Macromolecules* **35** (1), 16 (2001).

[51] V. Ganesan and G. H. Fredrickson, *Europhys. Lett.* **55** (6), 814 (2001).

[52] P. Tarazona, *Mol. Phys.* **52** (1), 81 (1984).

[53] P. Ballone, G. Pastore, and M. P. Tosi, *J. Chem. Phys.* **85** (5), 2943 (1986).

[54] G. M. Torrie and J. P. Valleau, *Chem. Phys. Lett.* **65** (2), 343 (1979).

[55] R. D. Groot, *Phys. Rev. A* **37** (9), 3456 (1988).

[56] A.-C. Shi and J. Noolandi, *Macromol. Theory and Simul.* **8** (3), 214 (1999).

[57] Q. Wang, T. Taniguchi, and G. H. Fredrickson, *J. Phys. Chem. B* **108** (21), 6733 (2004).

[58] S. Warren, M. Banholzer, L. Slaughter, E. Giannelis, F. DiSalvo, and U. Wiesner. *J. Am. Chem. Soc.* **128** (37), 12074 (2006).

CHAPTER 3

Predicting Chiral Nanostructures, Lattices and Superlattices in Complex Multi-Component Nanoparticle Self-Assembly[2]

ABSTRACT

‘Bottom up’ type nanoparticle (NP) self-assembly is expected to provide facile routes to nanostructured materials for various, e.g. energy related applications. Despite progress in simulations and theories, structure prediction of self-assembled materials beyond simple model systems remains challenging. Here we utilize a field theory approach for predicting nanostructure of complex and multicomponent hybrid systems with multiple types of short- and long-range interactions. We propose design criteria for controlling a range of NP based nanomaterial structures. In good agreement with recent experiments the theory predicts that ABC triblock terpolymer directed assemblies with ligand-stabilized NPs can lead to chiral NP network structures. Furthermore, we predict that long-range Coulomb interactions between NPs leading to simple NP lattices, when applied to NP/block copolymer (BCP) assemblies, induce NP superlattice formation within the phase separated BCP nanostructure, a strategy not yet realized experimentally. We expect such superlattices to become of increasing interest to communities involved in research on, e.g., energy generation and storage, metamaterials, as well as microelectronics and information storage.

---

[2] Reproduced with permission from: Kahyun Hur, Richard G. Hennig, Fernando A. Escobedo, and Ulrich Wiesner, *Nano Lett.* **12** (6), 3218-3223 (2012). Copyright 2012 American Chemical Society.

3.1. Introduction

Nanoparticle (NP) assembly and co-assembly is currently one of the key topics in materials science due to its broad relevance, ranging from fundamental aspects to technological applications in energy production and conversion, drug delivery, and tissue growth [1-13].For efficient materials design, predictive theoretical approaches that can quickly explore the associated vast parameter space are highly desirable, but are often lacking. This is particularly true for multicomponent soft materials systems. Here we utilize and further develop a recently developed field theory method detailed elsewhere [14] that harnesses the efficiency of self-consistent field theories (SCFTs) [15, 16] and the flexibility of density functional theory and a generalized propagator method. The method [14] enables the description of different types of components and interactions, *i.e.*, it allows a level of complexity usually reserved to more costly molecular simulation treatments [17]. Via the prediction of both known and unknown structures, we elucidate key factors governing self-assembly with resolution down to the near-molecular level, a step that may ultimately help to move theory closer to the realm of experiments.

The fundamental idea of field theory is to use chemical potential fields to represent the *n*-dimensional molecular phase space; *i.e.*, the position vector space of *n* particles. The correlated motion of the interacting particles is replaced with the motion of non-interacting particles moving in the field. Since the computational budget is independent of *n*, large molecular systems can be simulated efficiently. In this context, soft materials such as polymers have been successfully studied by SCFT [15, 16, 18-21], a mean-field theory employing the 'Gaussian model' for polymers [15].

Limitations of the mean-field approximation to polymers were later overcome by Ganesan *et al.* [22]. For polymer and NP mixtures, Thompson *et al.* developed a combined approach of SCFT and DFT for capturing hard sphere (HS) interactions [23]. Despite all these advances, major challenges remain in applications of field theories to multi-component/hybrid soft materials systems. Most importantly, not enough molecular detail in terms of structures and interactions could be incorporated in previous methods to make them general prediction tools of more realistic materials systems. Simulation approaches were suggested to overcome some of these limitations for hybrid systems [24, 25]. However, they have similar drawbacks as those of particle-based simulations such as finite system size effects on morphologies [18, 26] and significant computational budgets for large systems.

In order to overcome these limitations, we recently developed a field theoretical framework that provides substantially greater flexibility in the choice of molecular detail and interactions [14]. In most experiments of NP assembly and co-assembly, systems encompass multiple components such as sols, block copolymers, or ligand-stabilized NPs with multiple types of short- and long-range interactions including van der Waals, hard-particle and Coulomb interactions. For simulating such complex molecular systems, two separate approaches, density-functional theory (DFT) and polymer field theory, are unified into one method to exploit their combined descriptive power. Furthermore, the Green-function propagator approach used in polymer-field theory is extended to particles with different architectures including ligand-stabilized NPs (see Fig. 3.1). Key physical interactions such as long-range Coulomb interactions are incorporated in the context of DFT.

For the case of block copolymer directed nanoparticle self-assembly, the theory [14] enables us to find numerical solutions for the hybrid phase behavior without *a priori* knowledge of the ordered phase symmetries. This is made possible by the use of non-symmetrized basis sets in the numerical calculations, similar to other SCFT approaches to block copolymer mesophases [20, 38]. While the non-symmetrized approaches are advantageous for studying phase behavior in unexplored molecular hybrid systems, symmetry-adopted approaches [16] requiring the symmetry of the ordered phase as input provide more accurate free energies, needed for identifying the most stable structure, *e.g.* at phase boundaries between competing morphologies. While for the case of non-symmetrized basis sets real space as well as reciprocal (Fourier) space methods have been developed [20, 38], symmetrized basis sets have only been employed in reciprocal space [16]. However, such a symmetry-adopted reciprocal space approach [16] is not appropriate for systems with non-linear interactions such as hard-particle interactions. Here we therefore propose a symmetry-adopted real-space approach that can be applied to systems with any combination of interactions. To accurately identify the phase behavior of complex nanoparticle-block copolymer systems, both non-symmetrized[14] and symmetrized real space approaches are then utilized. The applications to be discussed henceforth exemplify the degree of experimental complexity that can be captured with this theory.

In the engineering of soft hybrid materials containing nanoparticles and block copolymers one important goal involves attaining precise control of ordered structures and spatial distributions of the polymeric components, the nanoparticles, or both. In this context, the use of special chemistries to create suitable enthalpic driving forces toward spatial order is essential to compensate entropic forces that typically favor more uniformly mixed states. Here we explore the use of ionic interactions as well as favorable van der Waals interactions in the NP design as a means to create suitable self-assembled nanostructures.

3.2. Results and Discussion

The first example for the application of our theory is the study of a realistic hybrid system with NPs and block copolymers (BCPs). In real experiments, NPs are typically complex hybrids themselves composed of hard inorganic cores and organic ligands. We want to incorporate such molecular features of the NP architecture in our calculations in order to investigate a synthetic route to chiral triblock terpolymer based composite network structures involving ligand-stabilized NPs. To the best of our knowledge, a theoretical or simulation study of such complex hybrid systems has not been attempted before. To illustrate that such systems may be experimentally feasible, it is instructive to take a look at the literature. Recently, mesoporous metals were synthesized using BCPs as structure directing agents for ligand-stabilized metal NPs [11]. On the block copolymer side Epps *et al.* synthesized poly(isoprene-*b*-styrene-*b*-ethylene oxide) (PI-*b*-PS-*b*-PEO) triblock terpolymers and obtained various network phases in a wide range of phase space [27]. Later, Tyler *et al.* studied the theoretical terpolymer phase diagram consistent with the experimental one applying SCFT [21]. One of the interesting network phases found by these authors is the alternating Gyroid, which is a cubic phase with space group 214 ($I4_132$, also denoted Q^{214}). Due to the lack of mirror symmetry through the two chemically distinct interweaving networks, such materials are chiral [27]. Indeed, the first oxide NP/triblock terpolymer composites with such chiral structures have been very recently described [28]. For predicting the structures of such NP/BCP composites we assume 10 vol.% of ligand stabilized NPs in a PI-*b*-PS-*b*-PEO triblock terpolymer, where the NPs preferentially segregate into the PEO block. The composition of the BCPs is set to $f_{PI} = 0.28$, $f_{PS} = 0.57$, and $f_{PEO} = 0.15$, which is very close to the lamellar/alternating Gyroid phase boundary for pure PI-*b*-PS-*b*-PEO block terpolymers [27]. For simulating ligand stabilized NPs, we introduce HS particles with 20 ligand molecules, where one ligand chain end is attached to the particle surface. The HS diameter is $d_0 = 0.4\, R_g$. We incorporate the Gaussian chain weight term to approximately account for the ligand conformation entropy, as outlined in Fig. 3.1e. We utilize the interaction parameters of block terpolymers introduced by Tyler *et al.* [21]. Other system parameters are summarized in Appendix A. Introducing exothermic mixing between ligands and PEO blocks, we obtain the alternating Gyroid morphology, where one of the two chiral networks is composed of the PEO block plus the NPs represented by the green isosurface in Fig. 3.2. In cases like metal NPs, synthesis often requires a ligand coverage of the NP to increase solubility/misability [11]. Careful ligand molecule design can realize such exothermic mixing. Figure 3.2b shows the NP distribution inside the alternating Gyroid network with slightly elevated densities for the triple Gyroid nodes as compared to the struts. We further calculated the phase diagram of competing morphologies as shown in Fig. 3.2c utilizing the symmetry-adopted real space approach introduced in Appendix A in order to obtain an accurate phase diagram. Interestingly, morphological changes occur for relatively dilute amounts of NPs with increasing the NP content (note that the core-shell double Gyroid morphology is observed at $\phi_{PEO} + \phi_p + \phi_{Ligand} \approx 0.3$ for the composite but at $\phi_{PEO} \approx 0.7$ for the neat block terpolymers shown in Ref. [21]).

To elucidate the effect of the NP cores on the phase behavior, we also simulated the case of the triblock terpolymers mixed with free ligands, *i.e.*, without any NP cores (see Fig. 3.2d). For this comparison the ligands are replacing the total volume that the ligand-grafted NPs were occupying in the previous case; this essentially preserves the enthalpic interactions since in both cases the terpolymer blocks only have direct contact with the ligands (with the NP cores mainly occupying a concealed space). The phase diagram for this reference system (Fig. 3.2d) is very different from that of the ligand-stabilized NP system (Fig. 3.2c). In particular, the lamellar and double Gyroid morphologies are missing (being mostly replaced by the O^{70} phase), and disordered mixtures of polymers and ligands are observed at high ϕ_{Ligand} values. Such large differences indicate that a more complex interplay of physical and chemical interactions of polymers and NPs, beyond those associated with minimal interface formation, governs nanostructure formation in complex multi-component self-assemblies. Indeed, in contrast to the case of free-ligands which blend uniformly within the PEO-rich domains, in the ligand-stabilized NP system the packing of PEO blocks around NPs favors a higher concentration of NPs in the centers of the PEO-rich domains (away from the interfaces, as shown in Fig. 3.2b), consistent with recent tomographic reconstruction data on networked oxide sol NP/triblock terpolymer composites [28]. This entropic "packing effect" becomes more pronounced as ϕ_p+ϕ_{Ligand} increases, promoting the formation of phases with thicker PEO domains than those attainable in the competing O^{70} phase. This analysis illustrates that even when enthalpic interactions are equivalent in two systems, differences in the architecture of the secondary component can create entropic effects that strongly modulate self-assembly.

These theoretical results are in good agreement with some of the results of recent experiments by Stefik *et al.* [28] for PI-*b*-PS-*b*-PEO triblock terpolymer/metal oxide NP self-assembly with similar polymer composition. In these experiments, hybrids with 5 vol.% of oxide NPs lead to the formation of an alternating Gyroid network phase, in agreement with the theoretical predictions (see Fig. 3.2c and d). In the range of 10~16 vol.% oxide NPs, a different network phase was observed experimentally, most likely the O^{70} phase; this phase exhibits broad peaks in the small angle x-ray scattering patterns, suggestive of structural heterogeneity within the samples. Such morphological inhomogeneity may arise from both the polydispersity of the size and shape of the oxide NPs and the slow structure formation dynamics in systems of higher inorganic material content. Polydispersity in the oxide NPs would induce spatial variations of packing entropy in the hybrids, potentially leading to the formation of a heterogeneous phase with alternating Gyroid and O^{70} domains; this could explain the experimental results.

Next we elucidate long-range interaction effects in NP self-assembly. For studying the effects of Coulomb interactions on NP self-assembly in 2-dimensions, we introduce positively charged (+) NPs and negatively charged (–) counter anions. The diameter of counter anions is $d_- = 0.2041\, d_+$, where d_+ is the NP diameter. The system consists of only NPs and counter anions with the overall volume fraction, $\phi_+ + \phi_- = 0.25$, embedded in a homogeneous dielectric medium. The charges of NPs and counter anions are set to $Z_+ = 10$ and $Z_- = -1$, respectively, and the charge neutrality condition is considered in the overall composition. The Coulomb interaction strength is controlled by the Bjerrum length, Γ, in the Coulomb potential, $V(\mathbf{r}) / k_B T = \Gamma Z_i Z_j / |\mathbf{r}|$. Without long-range Coulomb interactions (Γ=0), NPs are homogeneously dispersed without any ordered alignments. Fig. 3.3 shows the formation of a closed-packed hexagonal lattice of NPs for the Coulomb interaction strength of $\Gamma = 0.158\ d_+$. The region occupied by NPs is shown in green in Fig. 3.3a. The calculated density profiles of NPs (+) and counter anions (–) are depicted in Fig. 3.3b and 3.3c, respectively. The NPs are arranged on a hexagonal lattice and surrounded by counter anions. Such NP packing is related to recent observations of NP self-assembly into crystal lattices [8, 29-31]. This self-assembly of NPs was attributed to long-range Coulomb or dipole interactions between NPs. Our simulation demonstrates that charges can induce lattice formation for mono-dispersed NPs. The hexagonal packing represents the densest packing for spherical particles in 2-dimensional systems. Poly-disperse mixtures of NPs with incompatible NP sizes are known to lead to disordered packing [32]. The mono-disperse nature of the NPs in our simulations [14] is an important factor in the hexagonal lattice formation.

Having established NP lattice formation in a pure NP system, we move on to study the effect of Coulomb interaction strength on NP/BCP composite systems. BCPs composed of two chemically distinct blocks, A and B, are added to the pure NP system. The overall volume fraction of NPs and counter anions is reduced to $\phi_+ + \phi_- = 0.15$ while the BCPs constitute the rest of the system. The BCP composition is given by the portion of block A, $f_A = 0.35$, and the BCP radius of gyration is set to $R_g = 1.02\ d_+$. NPs and counter anions are repulsive to block B and preferentially segregate into block A. Other system parameters for these calculations are summarized in Appendix A. Figure 3.4 shows the result for the NP/BCP composite system as a function of Coulomb interaction strength. Without Coulomb interactions (Γ=0), the NPs preferentially assemble inside the lamellae of block A with a slight preference towards the edge of the lamellae (red in Fig. 3.4a). For a weak Coulomb interaction with $\Gamma = 0.031\ R_g$, the edge-assembly of NPs becomes more pronounced, as shown in Fig. 3.4b. Since the Coulomb repulsion between the NPs is in addition to the HS repulsions, the segregation of NPs to the lamellae interface is enhanced. When the Coulomb interaction is further increased to $\Gamma = 0.145\ R_g$, some of the NPs as well as block A segments are now mixed with block B. This occurs because the Coulomb interaction is strong enough to overcome the mixing enthalpy penalty of NPs and block B, *i.e.*, the positive χ_{B+} value. Interestingly, only a slight further increase of the Coulomb interaction strength, to $\Gamma = 0.161\ R_g$, triggers the formation of a NP superlattice within the phase separated BCPs. Fig. 3.4d shows regularly arranged NPs in a lamellar block copolymer nanostructure (i.e. a NP superlattice in a 1D lamellar BCP lattice). The density profile of NPs shown in Fig. 3.4e clearly illustrates the lattice formation of NPs within block A. The transition from disordered to ordered NP formation is discontinuous and the critical Coulomb strength is expected to depend on the interactions with the BCPs. However, a considerable amount of NPs locate in block B and also arrange regularly as seen in Fig. 3.4e. To completely segregate NPs within block A and arrange them on a lattice, a strong segregation of NPs from block B, *i.e.*, a high χ_{B+} value, is required. Fig. 3.4f shows the effect of the interaction parameter, $\chi_{AB}N = \chi_{B+}N = \chi_{B-}N$, on the critical Γ value for which lattice formation occurs. The critical Coulomb interaction strength Γ for lattice formation increases with increasing χ. Therefore, strong Coulomb interactions between NPs are needed for superlattice formation in the case of strong segregation, *i.e.*, at high χ values. We further studied the effect of NP volume fraction on the Coulomb interaction strength for lattice formation. Denser NPs form a lattice with weaker Coulomb interaction strength as shown in Fig. 3.4f. Due to stronger NP confinement effects in denser NP distributions, the lattice formation is triggered with smaller Γ values. Consequently, higher NP loading in NP/BCP co-assemblies is more effective in driving lattice formation. Altogether, these results indicate that NP superlattice formation in BCP based polymer lattices depends on the interplay of multiple parameters including the interaction parameter χ, the Coulombic strength and NP loading.

To further highlight the significance of Coulombic interactions in the preceding results, we studied as a reference case a NP/BCP system lacking Coulombic forces. The interaction parameter between the NPs and block A, $\chi_{A+}N$, was assumed to give exothermic mixing to avoid macro-phase separation. We obtained an accurate phase diagram as a function of NP volume fraction, ϕ_{+}, and $\chi_{A+}N$ (see Fig. 3.4g) utilizing the symmetry-adopted real space approach. The increase of ϕ_+ (for fixed $\chi_{A+}N$) leads to the morphology progression: Lamellae → double Gyroid → hexagonal cylinders. The morphology is weakly sensitive to changes in $\chi_{A+}N$ (for fixed ϕ_+), at least for the range of $\chi_{A+}N$ considered here. Such morphology changes (Fig. 3.4g) are not observed for the systems with Coulomb interactions discussed before (upon variation of Γ and ϕ_+). The difference arises mainly from the fact that such interactions drive the spatial distribution of charged NPs to spread out with the most regular interparticle spacings allowable leading to the formation of a higher symmetry structure and a reduction of the interfacial curvature. These results illustrate how different types of enthalpic interactions can be utilized to design widely different morphologies in otherwise identical NP/BCP composites.

In summary, we presented results of a field-theory approach for predicting nanostructure of self-assembled NP based materials. Our approach offers the flexibility to (i) include complex multi-component molecules including ligand-stabilized NPs and to (ii) incorporate various types of interactions. The propagator approach was utilized to incorporate complex molecular details of soft/hard multi-component molecules/NPs. HS and Coulomb interactions between NPs were implemented to describe NP self-assembly. For identifying accurate phase behavior of complex NP-BCP systems, a symmetry-adopted real space approach was introduced. As an application of the approach, insights into the formation of chiral ligand-stabilized NP/triblock terpolymer network structures were provided. For a system of charged NPs and counter ions, the formation of a hexagonal lattice in two dimensions was predicted. The same strategy was transferred to NP/BCP assemblies to arrange

NPs on a superlattice within the phase separated BCP structure. Such NP/BCP superlattices may be of interest for energy generation and storage, metamaterials, as well as microelectronics and information storage. Based on the breadth of examples discussed, our approach is expected to provide insights into various mesoscopic systems and to elucidate key factors that govern the physics of the respective bottom-up type self-assembly. Furthermore, its efficiency in sampling phase space and its ability to incorporate molecular details may eventually enable simulations for molecular systems of unprecedented size and complexity, including biological systems, with resolution down to the molecular level.

Acknowledgements

This publication is based on work supported in part by Award No. KUS-C1-018-02, made by King Abdullah University of Science and Technology (KAUST). This work was further supported by a single investigator award of the National Science Foundation (DMR-1104773). The calculations were performed using computational resources of the Computational Center for Nanotechnology Innovation (CCNI) at Rensselaer Polytechnic Institute.

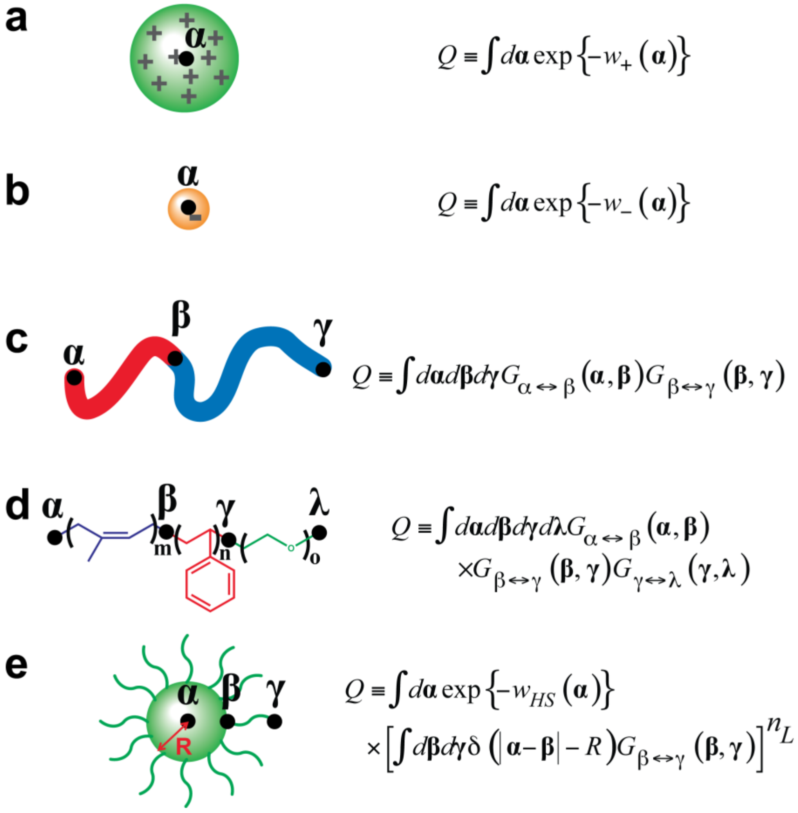

$$Q \equiv \int d\boldsymbol{\alpha} \exp\{-w_{+}(\boldsymbol{\alpha})\}$$

$$Q \equiv \int d\boldsymbol{\alpha} \exp\{-w_{-}(\boldsymbol{\alpha})\}$$

$$Q \equiv \int d\boldsymbol{\alpha} d\boldsymbol{\beta} d\boldsymbol{\gamma} G_{\alpha \leftrightarrow \beta}(\boldsymbol{\alpha}, \boldsymbol{\beta}) G_{\beta \leftrightarrow \gamma}(\boldsymbol{\beta}, \boldsymbol{\gamma})$$

$$Q \equiv \int d\boldsymbol{\alpha} d\boldsymbol{\beta} d\boldsymbol{\gamma} d\boldsymbol{\lambda} G_{\alpha \leftrightarrow \beta}(\boldsymbol{\alpha}, \boldsymbol{\beta}) \times G_{\beta \leftrightarrow \gamma}(\boldsymbol{\beta}, \boldsymbol{\gamma}) G_{\gamma \leftrightarrow \lambda}(\boldsymbol{\gamma}, \boldsymbol{\lambda})$$

$$Q \equiv \int d\boldsymbol{\alpha} \exp\{-w_{HS}(\boldsymbol{\alpha})\} \times \left[\int d\boldsymbol{\beta} d\boldsymbol{\gamma} \delta\left(|\boldsymbol{\alpha}-\boldsymbol{\beta}| - R\right) G_{\beta \leftrightarrow \gamma}(\boldsymbol{\beta}, \boldsymbol{\gamma})\right]^{n_L}$$

Figure 3.1. The single molecular partition functions Q of simulated species. **a**, positively charged NP. **b**, negatively charged counter anion. **c**, di-BCP. **d**, Poly(isoprene-b-styrene-b-ethylene oxide) tri-BCP. **e**, ligand-stabilized NP composed of a hard sphere (HS) and n_L ligand molecules. Bold Greek letters represent positional vectors that correspond to black dots in molecular representations and $\delta(x)$ is the Dirac delta function. The chemical potential fields, w, and the propagators, G, are discussed in Appedix A.

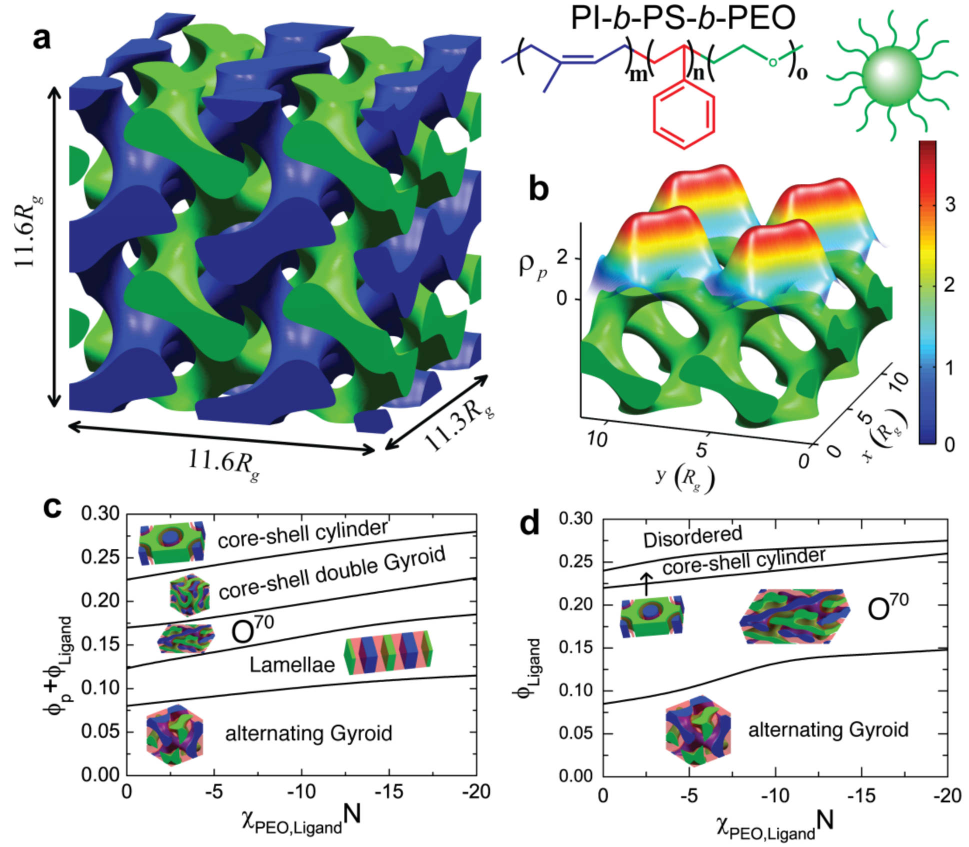

Figure 3.2. Poly(isoprene-*b*-styrene-*b*-ethylene oxide) (PI-*b*-PS-*b*-PEO) / ligand-stabilize NP composite forms alternating Gyroid morphology. Ligand-stabilized NPs embedded in the green struts form a chiral network structure directed by the BCP self-assembly.Isosurfaces of local volume fractions equal to 0.5 are shown in distinct colors for each components. **a**, The blue isosurface represents isoprene and the green one ethylene oxide with ligand stabilized NPs. **b**, The density profile of ligand stabilized NPs, ρ_p, superimposed on a cross section parallel to a [001] plane of the PI-*b*-PS-*b*-PEO / ligand stabilized NP composite with alternating Gyroid morphology. For clear visualization of the struts, some areas of ρ_p with small NP densities are set to be transparent. A slightly elevated density of NPs is observed for the nodes as comparedto the struts. **c**, The phase diagram of the ligand-stabilized NP composite for varying composition and interaction parameter between PEO block and ligands. **d**, The phase diagram of the block terpolymers and free ligands without the NP cores (shown for comparison).

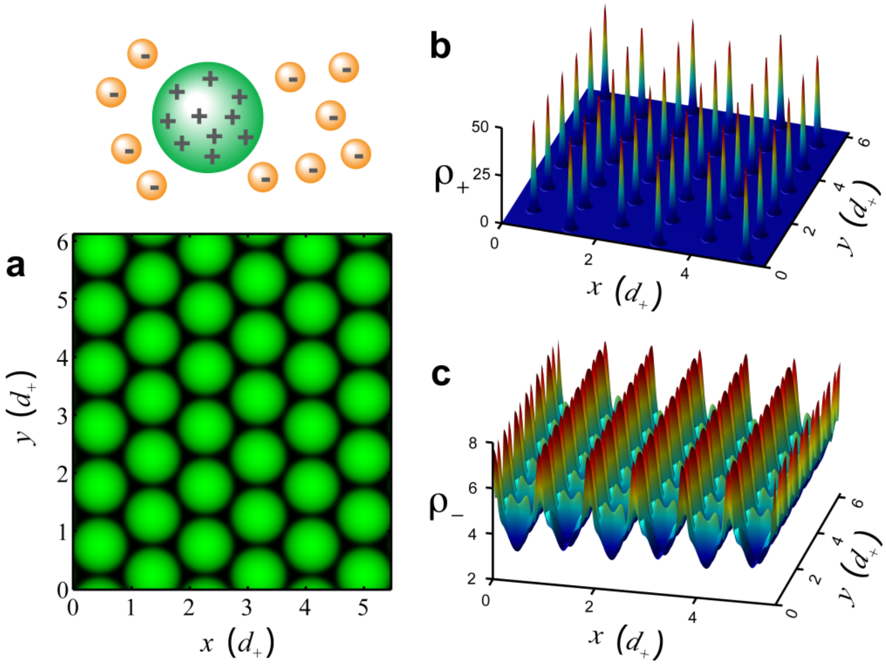

Figure 3.3. Coulomb interactions induce lattice formation of NPs. **a**, Green color represents regions occupied by NPs. **b**, The density profile of positively charged (+) NPs, ρ_+. **c**, the density profile of negatively charged (-) counter anions, ρ_-.

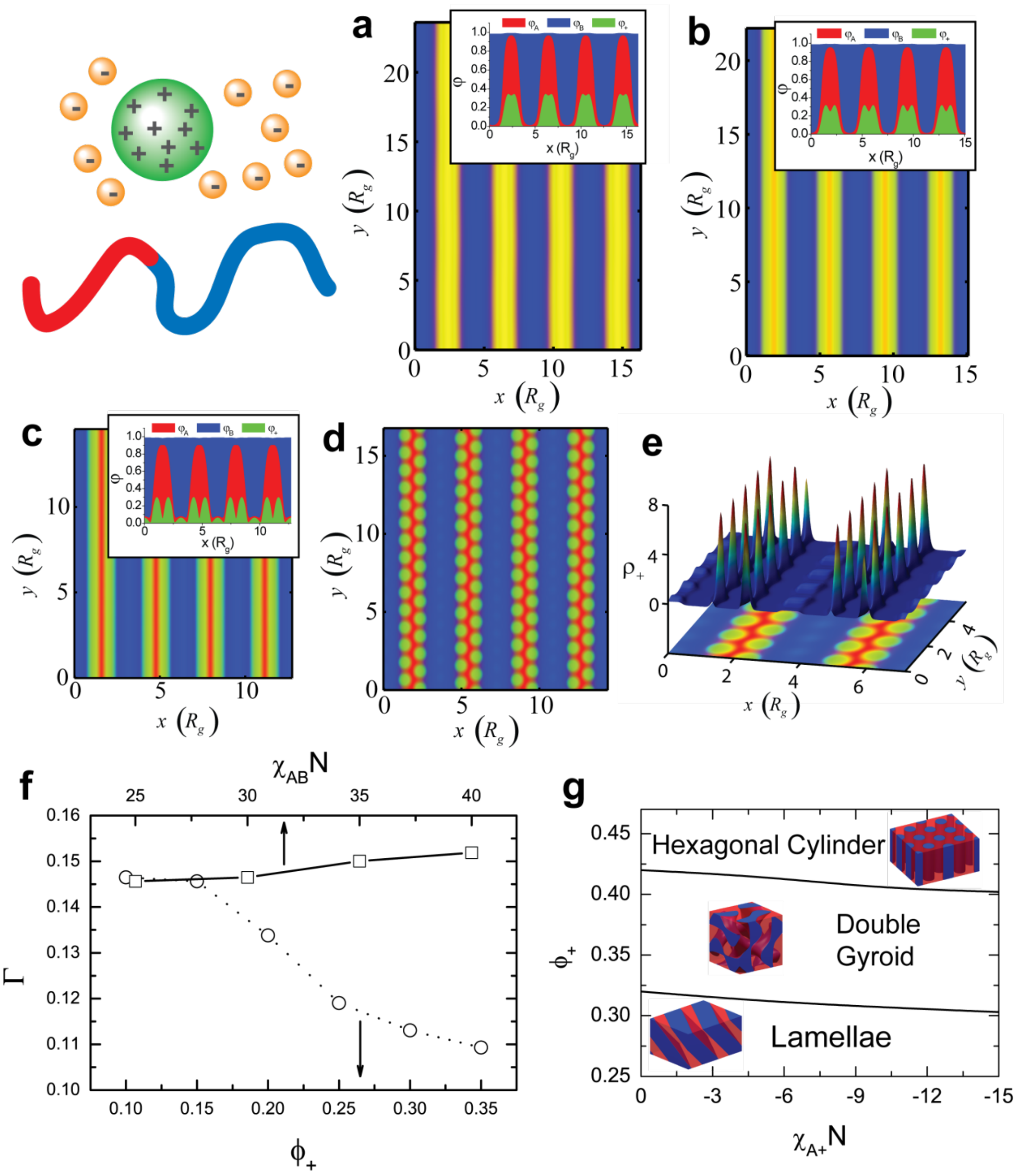
a
b
c
d
e
f
g
φ_A φ_B φ_+
φ
x (R_g)
y (R_g)
ρ_+
χ_AB N
Γ
φ_+
χ_A+ N
Hexagonal Cylinder
Double Gyroid
Lamellae

Figure 3.4. Coulomb interactions between NPs control lamellar morphology and above a critical Coulomb interaction strength induce superlattice formation of NPs within one dimensional (lamellar) BCP lattices. Red color represents block A, blue color block B, and green color represents the NPs. The insets demonstrate the cross sectional view of compositions along the *x* axis. The Coulomb interaction strength is controlled by varying Γ in the Coulomb potential, $V(\mathbf{r})/k_BT = \Gamma Z_i Z_j / |\mathbf{r}|$, with (**a**) $\Gamma = 0\ R_g$, (**b**) $\Gamma = 0.031\ R_g$, (**c**) $\Gamma = 0.145\ R_g$, and (**d**,**e**) $\Gamma = 0.161\ R_g$. **e**, The density profile ρ_+ of NPs in phase separated BCP/NP assemblies. For a comparison, the projection on the *xy* plane equivalent to **d** is shown underneath the density profile. **f**, The critical Γ values for superlattice formation shown as a function of the repulsive interaction parameter, $\chi_{AB}N$ (squares with solid lines), and as a function of the NP volume fraction, ϕ_+ (circles with dotted lines). Strong Coulomb interactions between NPs are needed for superlattice formation with increasing segregation strength, *i.e.*, at higher $\chi_{AB}N$ values, while due to the confinement effect of NPs in block A, the driving force for lattice formation decreases with increasing ϕ_+. **g**, Phase diagram for a reference non-ionic system as a function of ϕ_+ and the interaction parameter, $\chi_{A+}N$.

APPENDIX A

Simulation Methods

Here we briefly introduce basic features of our approach. A more detailed description can be found in Ref. [14]. The Helmholtz free energy in our field theory is given by

$$F = F^0 + F^\chi + F^{HS} + F^C \quad . \tag{1}$$

The first term in Eq. (1) is the conformational and mixing entropy of molecules given by $F^0 = -\sum n_i \ln Q_i - \sum \int d\mathbf{r} w_i(\mathbf{r}) \rho_i(\mathbf{r})$, where n_i is the number of molecules i in a system and Q_i is its single molecular partition function. w and ρ are chemical potential fields and densities, respectively, of monomer species composing the molecules. The molecular partition function, Q, describes the molecular structures as exemplified in Fig. 3.1 for different molecules. The implementation of Q is a key step for incorporating molecular structures and requires the most intensive computation in field theories. The Green function propagator, G, of polymer segments has been implemented for calculating Q.[15,16,33] By generalizing the propagator for other types of materials including NPs, we can simulate hybrid NPs/molecules composed of organic and inorganic materials without any loss of efficiency reserved to SCFTs. The other three terms in Eq. (1) represent the excess free energies of short-range enthalpic (F^{χ}), hard sphere (HS) (F^{HS}), and long-range Coulomb interactions (F^{C}), respectively. For NP/BCP mixtures, Thompson *et al.* implemented F^{χ} and F^{HS} for NP interactions [23]. However, due to the different physical and chemical nature of NPs, various types of interactions including long-range Coulomb interactions are required to study realistic experimental systems. To this end, the Coulomb potential is incorporated utilizing a direct correlation function [34] combined with the Ewald summation technique [35].

For enabling more accurate calculations of phase diagrams than non-symmetrized calculations, here we propose a symmetry-adopted 'real space' approach by projecting the chemical fields, w, with normalized and symmetrized basis functions, f, [36] as

$$w_i'(\mathbf{r}) = \sum_j f_j(\mathbf{r}) \int d\mathbf{r}' w_i(\mathbf{r}') f_j(\mathbf{r}') \qquad \textbf{(2)}$$

where w_i' is the symmetry-adopted chemical field of monomer species i. Other processes are identical to those outlined in Ref. [1]. This approach can be applied to systems with any combination of interactions, whereas the reciprocal space approach [16, 38] is not feasible for non-linear interactions such as HS interactions. Non-symmetrized approaches [20, 38] are advantageous for studying unexplored molecular systems while symmetrized approaches [16] provide more accurate free energy calculations of competing nanostructures. Exploiting advantages of both approaches, one can accurately identify the phase behavior of complex molecular hybrid systems.

Although reciprocal approaches [16, 38] require a much smaller number of functions, M, in the basis set than real space approaches, the computational budget scales as M^3 in reciprocal approaches, while the use of the Fast Fourier Transform and the propagator approach leads to a scaling of $M\log M$ in real space approaches [14]. Therefore, real space approaches are usually more advantageous than reciprocal approaches not only for a wider range of applications but also for more efficient computations.

Simulation parameters

Chiral self-assemblies of ligand stabilized nanoparticles (NPs) within PI-*b*-PS-*b*-PEO tri-BCPs (Fig. 3.2)

χN	PS	PEO	Ligand	HS
PI	11	45.8	45.8	45.8
PS		14.2	14.2	14.2
PEO			-15	0
Ligand				0

Table S1. χN parameters for chiral self-assemblies of ligand stabilized NPs within PI-*b*-PS-*b*-PEO tri-BCPs

To simulate ligand stabilized NPs, we incorporate the Gaussian chain weight term for ligand conformations to account for their conformational entropy. The size of one ligand molecule is given by $N_{Ligand} / N = 1/250$, which corresponds to a single Kuhn segment. The number of ligands per HS particle is set to $n_{Ligand} = 20$ and one chain end of the ligand molecules is attached to the HS particle surface. The single molecular partition function of the NPs, Q, is given in Fig. 3.1 and its calculation process is outlined in Section III.D of Ref. [14], where the continuous propagator for polymer segments is utilized for the ligands. For polymer interaction, χN, parameters, we utilize the parameters given by Tyler *et al.* due to their ability to well reproduce the experimental phase diagram [37]. χN for ligand stabilized NPs are set to drive them to segregate into the PEO block. Exothermic mixing of ligand molecules and PEO blocks is assumed and all χN parameters are summarized in Table S1 of Appendix A. The Kuhn lengths for each chemical species are set to $a_{PS} / a_{PI} = 0.917$, $a_{PEO} / a_{PI} = 1.3$, and $a_{Ligand} / a_{PI} = 1.3$ for PS, PEO, and ligand molecules, respectively. The composition of BCPs is set to $f_{PI} = 0.28$, $f_{PS} = 0.57$, and $f_{PEO} = 0.15$. The diameter of HS particles is $d_0 = 0.4\, R_g$. The volume fraction of ligand stabilized NPs is set to $\phi_p + \phi_{Ligand} = 0.1$. We assign 0.517 for $N\rho_0^{-1}R_g^{-3}$ based on the physical data of PI-*b*-PS-*b*-PEO BCPs given by Tyler *et al.* [37].

Charged NP / counter anion (CA) super lattices in self-assemblies with BCPs (Fig. 3.4)

χN	B	+	-
A	20	0	0
B		20	20
+			0

Table S2. χN parameters for the self-assembled superlattices of charged NPs and CAs within lamellar BCPs

In this work, we study charged NP self-assembly behavior within BCPs. The radius of gyration of unperturbed BCPs, R_g, is the basic length unit in this work. The diameter of NPs is given by $d_+ = 0.9798\ R_g$. Since the CA volume is expected to be small, the diameter of CAs is set to a small value, $d_- = 0.2\ R_g$, compared with the NP diameter. The overall volume fraction of NPs and CAs is set to $\phi_+ + \phi_- = 0.15$. $\chi_{ij} N$ parameters, as summarized in Table S2 of Appendix A, are set to $\chi_{AB} N = \chi_{B+} N = \chi_{B-} N = 20$, a value large enough for BCP microphase separation to occur, and $\chi_{A+} N = \chi_{A-} N = \chi_{+-} N = 0$ for particles to be segregated preferentially into A-block domains. The BCP composition is set at $f_A = 0.35$ for obtaining one-dimensional (1D) lamellar morphologies for the NP/BCP composite. The charges are fixed at $Z_+ = 10$ and $Z_- = -1$, while Γ is varied to control the Coulomb interaction strength from $\Gamma = 0\, R_g$ to $\Gamma = 0.161\, R_g$. The charge neutrality condition requires that the number of CAs be 10 times the number of NPs. We assign a typical value of 0.4655 for $N\rho_0^{-1}R_g^{-3}$.

REFERENCES

[1] D. J. Norris, A. L. Efros, S. C. Erwin, *Science* **319** (5871), 1776-1779 (2008).

[2] T. Hyeon, S. S. Lee, J. Park, Y. Chung, H. B. Na, *J. Am. Chem. Soc.* **123** (51), 12798-12801 (2001).

[3] V. F. Puntes, K. M. Krishnan, A. P. Alivisatos, *Science* **291** (5511), 2115-2117 (2001).

[4] H. Zheng, R. K. Smith, Y.-w. Jun, C. Kisielowski, U. Dahmen, A. Alivisatos, *Science* **324** (5932), 1309-1312 (2009).

[5] M. L. Steigerwald, A. P. Alivisatos, J. M. Gibson, T. D. Harris, R. Kortan, A. J. Muller, A. M. Thayer, T. M. Duncan, D. C. Douglass, L. E. Brus, *J. Am. Chem. Soc.* **110** (10), 3046-3050 (1988).

[6] I. Gur, N. A. Fromer, M. L. Geier, A. P. Alivisatos, *Science* **310** (5747), 462-465 (2005).

[7] F. X. Redl, K. S. Cho, C. B. Murray, S. O'Brien, *Nature* **423** (6943), 968-971 (2003).

[8] E. V. Shevchenko, D. V. Talapin, N. A. Kotov, S. O'Brien, C. B. Murray, *Nature* **439** (7072), 55-59 (2006).

[9] M. A. Noginov, G. Zhu, A. M. Belgrave, R. Bakker, V. M. Shalaev, E. E. Narimanov, S. Stout, E. Herz, T. Suteewong, U. Wiesner, *Nature* **460** (7259), 1110-1112 (2009).

[10] S. C. Warren, F. J. DiSalvo, U. Wiesner, *Nat Mater* **6** (2), 156-161 (2007).

[11] S. C. Warren, L. C. Messina, L. S. Slaughter, M. Kamperman, Q. Zhou, S. M.

Gruner, F. J. DiSalvo, U. Wiesner, *Science* **320** (5884), 1748-1752 (2008).

[12] D. Gebauer, A. Volkel, H. Colfen, *Science* **322** (5909), 1819-1822 (2008).

[13] E. M. Pouget, P. H. H. Bomans, J. A. C. M. Goos, P. M. Frederik, G. de With, N. A. J. M. Sommerdijk, *Science* **323** (5920), 1455-1458 (2009).

[14] K. Hur, R. G. Hennig, F. Escobedo, U. Wiesner, *J. Chem. Phys.* **133** (19), 194108-194119 (2010).

[15] E. Helfand, *J. Chem. Phys.* **162** (3), 999-1005 (1975).

[16] M. W. Matsen, M. Schick, *Phys. Rev. Lett.* **72** (16), 2660 (1994).

[17] C. L. Phillips, C. R. Iacovella, S. C. Glotzer, *Soft Matter* **6** (8), 1693–1703 (2010).

[18] Y. Bohbot-Raviv, Z.-G. Wang, *Phys. Rev. Lett.* **85** (16), 3428 (2000).

[19] G. M. Grason, B. A. DiDonna, R. D. Kamien, *Phys. Rev. Lett.* **91** (5), 058304 (2003).

[20] F. i. Drolet, G. H. Fredrickson, *Phys. Rev. Lett.* **83** (21), 4317 (1999).

[21] C. A. Tyler, J. Qin, F. S. Bates, D. C. Morse, *Macromolecules* **40** (13), 4654-4668 (2007).

[22] V. Ganesan, G. H. Fredrickson, *EPL (Europhysics Letters)* **55** (6), 814-820 (2001).

[23] R. B. Thompson, V. V. Ginzburg, M. W. Matsen, A. C. Balazs, *Science* **292** (5526), 2469-2472 (2001).

[24] S. W. Sides, B. J. Kim, E. J. Kramer, G. H. Fredrickson, *Phys. Rev. Lett.* **96** (25), [250601-4 (2006).

[25] A. Detcheverry, D. Q. Pike, P. F. Nealey, M. Muller, J. J. de Pablo, J. J.

Phys. Rev. Lett. **102** (19), 197801-4 (2009).

[26] F. J. Martínez-Veracoechea, F. A. Escobedo, *Macromolecules* **40** (20), 7354-7365 (2007).

[27] T. H. Epps, E. W. Cochran, T. S. Bailey, R. S. Waletzko, C. M. Hardy, F. S. Bates, *Macromolecules* **37** (22), 8325-8341 (2004).

[28] M. Stefik, S. Wang, R. Hovden, H. Sai, M. W. Tate, D. A. Muller, U. Steiner, S. M. Gruner, U. Wiesner, *J. Mater. Chem.* **22** (3), 1078-1087 (2012).

[29] M. E. Leunissen, C. G. Christova, A.-P. Hynninen, C. P. Royall, A. I. Campbell, A. Imhof, M. Dijkstra, R. van Roij, A. van Blaaderen, *Nature* **437** (7056), 235-240 (2005).

[30] A. M. Kalsin, M. Fialkowski, M. Paszewski, S. K. Smoukov, K. J. M. Bishop, B. A. Grzybowski, *Science* **312** (5772), 420-424 (2006).

[31] P. Bartlett, A. I. Campbell, *Phys. Rev. Lett.* **95** (12), 128302 (2005).

[32] A. Donev, I. Cisse, D. Sachs, E. A. Variano, F. H. Stillinger, R. Connelly, S. Torquato, P. M. Chaikin, *Science* **303** (5660), 990-993 (2004).

[33] G. M. Grason, R. D. Kamien, *Phys. Rev. E* **71** (5), 051801 (2005).

[34] Y. Rosenfeld, *J. Chem. Phys.* **98** (10), 8126-8148 (1993).

[35] D. Frenkel, B. Smit, *Understanding molecular simulation : from algorithms to applications*. 2nd ed.; Academic Press: San Diego, 2002; p xxii, 638 p.

[36] D. C. Tyler, D. C. Morse, *Macromolecules* **36** (10), 3764-3774 (2003).

[37] D. C. Tyler, D. C. Morse, *Macromolecules* **36** (21), 8184-8188 (2003).

[38] Z. Guo, G. Zhang, F. Qiu, H. Zhang, Y. Yang, A.-C. Shi, *Phys. Rev. Lett.* **101** (2), 028301-4 (2008).

CHAPTER 4

Three-dimensionally Isotropic Negative Refractive Index Materials from Block Copolymer Self-assembled Chiral Gyroid Networks[3]

ABSTRACT

Engineered artificial materials named metamaterials offer new functionalities such as super-resolution imaging and cloaking. Despite considerable progress, finding efficient pathways towards 3-dimensionally isotropic metamaterials remains challenging thus hampering their practical applications. Here we present calculations of the photonic properties of three-dimensionally isotropic metallic nanomaterials with the cubic double gyroid and the alternating gyroid morphologies. These materials can be obtained by block copolymer self-assembly with a unit cell significantly smaller than the free space wavelength of visible light. For double gyroid metamaterials, we specifically identify the materials parameters and design principles for negative-refractive index materials in the visible and near infrared spectrum. In alternating gyroid metamaterials, due to lack of a second minority network, a metallic band gap is predicted. Furthermore, both structures show circularly polarized light propagation originating from the intrinsic chirality of the minority gyroid networks. Results suggest efficient design criteria for self-assembly based metamaterials overcoming current fabrication challenges.

---

[3] Reproduced with permission from: Kahyun Hur, Yan Francescato, Vincenzo Giannini, Stefan A. Maier, Richard G. Hennig, and Ulrich Wiesner, *Angew. Chem. Int. Ed.* **50** (50), 11985-11989 (2011). Copyright 2011 WILEY-VCH Verlag GmbH & Co. KGaA, Weinheim.

4.1. Introduction

In 1999, Pendry predicted that specifically engineered artificial materials, *i.e.* metamaterials, would have unusual magnetic responses, *e.g.* negative permeability [1]. Following this work, much effort has been devoted to the design and fabrication of metamaterials with negative refractive index [2-6] Such negative index metamaterials have the potential, *e.g.* in the form of superlenses, to overcome the diffraction limit in imaging or to enable novel optical effects, including cloaking [7-9]. Today most metamaterial fabrication relies on top-down approaches such as lithography techniques, making efficient access to three-dimensionally (3D) isotropic metamaterials challenging thus hindering their practical applications [10, 11] Recent progress in bottom-up type self-assembly offers promise to overcome some of these limitations [12-14]. In particular block copolymer (BCP) self-assembly has emerged as a useful designer tool to create nanostructures including 3D continuous morphologies of disparate materials like ceramics and metals [15, 16] The present paper makes clear theoretical predictions for how to design 3D isotropic materials with negative refraction and circularly polarized light propagation from a class of block copolymer based self-assembled materials not yet rigorously studied in the context of metamaterials. Through theoretical understanding and guidance on materials choices, characteristic length and frequency scales, which are determined by calculations and described in detail in the manuscript, a "recipe" is provided for the synthesis, fabrication and characterization of these materials.

We present calculations of the photonic properties of 3D periodic metallic nanomaterials with co-continuous cubic morphologies as illustrated in Figure 4.1.

Such structures are experimentally accessible through self-assembly of AB diblock copolymers and ABC triblock terpolymers and are referred to as double gyroid (D-GYR) and alternating gyroid (A-GYR). Both of these structures have two 3D continuous cubic and interwoven minority networks separated by a matrix majority network. In the A-GYR the two minority networks are distinguishable leading to chirality while in the D-GYR they are not. We predict for the resulting metallic nanomaterials that the coupled surface plasmon resonance of the two minority networks of the D-GYR induces low frequency light propagation with a negative index of refraction. Due to their cubic symmetry, these materials are 3D isotropic (see Fig. 4.1e). They also show circularly polarized light propagation originating from the chirality of the gyroid networks. We further predict that by tailoring BCP synthesis one can design materials with varying refractive index and frequency at which negative refraction occurs. Finally, in contrast to D-GYR metallic nanomaterials, chiral A-GYR metallic nanomaterials are expected to exhibit a surprising metallic band gap despite their smaller metallic fraction. We conclude that these periodic structures would effectively behave like metamaterials.

A gyroid is a 3D co-continuous structure with cubic symmetry based on the triply periodic G minimal surface (see Fig. 4.1 and Ref. [17, 18] for their topological characteristics). Minimal surfaces have a mean curvature of zero everywhere. Familiar examples include surfaces of minimum area formed by soap films obtained from dipping wire frames into soap solutions. Due to characteristics of materials with cubic symmetry, metamaterials with gyroid structure are inherently isotropic in 3D and so are their optical responses19 as compared to other metamaterials [1, 4]. After the first discovery of a gyroid in BCP self-assembly, gyroid-based materials self-assembly has received significant attention and in the meantime has led to the first electronic devices [20-23]. Furthermore, such 3D isotropic gyroid structure was also in intermetallic compounds [24, 25] The D-GYR morphology is composed of two minority networks of the same monomer species obtained from AB diblock copolymers, where each network has opposite chirality and is the inversion of the other. Due to this inversion symmetry, the structure is not chiral, and belongs to the space group $Ia\overline{3}d$, denoted Q^{230} [26]. In contrast the A-GYR has two minority networks composed of different monomer species and is obtained from ABC triblock terpolymers (red and blue domains in Fig. 4.1c). Since the two minority networks are chemically distinct the structure lacks inversion symmetry and becomes chiral with space group $I4_132$, denoted Q^{214} [26]. Our metamaterials are designed by assuming selective etches of different blocks of AB diblock and ABC triblock polymer derived gyroids and deposition of metal into the resulting pores as shown in the schematic diagrams in Fig. 4.1. Recent synthetic progresses [27, 28] show that the proposed schemes are feasible for metamaterials fabrication.

Before describing the results of our calculations, it is instructive to look into what kind of optical behavior can be expected for the gyroid structures shown in Fig. 4.1. It is expected that 3D continuous metallic networks have a metallic band gap below a certain cut-off frequency due to a strong plasmon response at low frequencies [29] However, for the D-GYR morphology, the two separate gyroid networks form a capacitor leading to a different light propagation mechanism. Such light propagation originates from the coupled surface plasmon resonances on the closed loops of gyroid networks (see Fig. 4.1d-f). The gyroid capacitor becomes a metal/insulator/metal (MIM) wave guide as depicted in Fig. 4.1g. This coaxial MIM geometry [30] supports surface plasmon polariton propagation. Resulting photonic behaviors are very unique. The longest wavelength at the Brillouin zone boundary reaches $\lambda=34a$ in vacuum for a D-GYR metamaterial with unit cell size, $a=25\ nm$. Furthermore, as will be shown below, their refractive index and frequency range can be controlled by the lattice constant, *i.e.* without changing the deposited materials. Due to limitations of the unit cell size to values typically below $150\ nm$ [31], dielectric materials-based photonic applications utilizing BCP self-assembly for visible and longer wavelengths are usually challenging [32]. However, the wave-guide bands result in negative refraction in visible and near-infrared regimes. With calculations described below we confirm that in these bands the wave vector and the Poynting vector have opposite directions. Remarkably these bands exhibit very small refractive index dispersion and propagation with low losses as shown in Figure S1b of Appendix B. Our theoretical results suggest that metamaterials fabrication from bottom-up BCP self-assembly may result in interesting optical properties thus moving them closer to the realm of practical applications.

4.2. Simulation Methods

We used self-consistent field theory, one of the most powerful methods to describe BCP morphologies [33, 34], to obtain realistic representations of the D-GYR and A-GYR morphologies. We subsequently calculated the photonic band structures of three different types of metal structures as shown in Fig. 4.1, which we refer to as

D-GYR, hollow D-GYR, and A-GYR metamaterials. For the calculations, two simulation methodologies were used, an eigensolver of Maxwell's equation following Ref. [35] and finite element-based software COMSOL [36].

4.3. Results and Discussion

First, using the eigensolver approach, we calculated the band structures of the D-GYR metamaterial made of gold described by a Drude model [37] without losses with unit cell size, $a=100\ nm$, and the plasma frequency, $\omega_p=2\pi\times 2.19\times 10^{15}\ Hz$, as shown in Fig. 4.2a. The characteristic flat bands of metallic photonic crystals [35, 38] are observed within a frequency range, $0.22<\omega a/2\pi c<0.55$, the orange region in the band structure (see Fig. 4.2b). Those bands are not shown due to extremely dense populations in this regime (note that the spacing between neighboring bands is less than 10^{12} Hz.). Fig. 4.2c details the low frequency bands. Despite the high portion of metal, low frequency light propagation is observed. Interestingly, negative refraction bands are found and examples are highlighted in red (fast propagation) and orange (slow propagation) in Fig. 4.2c. For such negative refraction bands, the photonic energy flux given by the Poynting vector [39] is opposite to the momentum vector, **k**. Fig. 4.2c and d show the directions of the time-averaged local Poynting vector $\mathbf{S}=1/2\mathrm{Re}[\mathbf{E}\times\mathbf{H}^*]$ for positive and negative refraction bands. Clearly, the direction of **S** is opposite to that of **k** for negative refraction. Such negative refraction is further observed at different momentum vectors, $\mathbf{k}=[0.1,0.1,0]$ and $\mathbf{k}=[0.1,0.1,0.1]$, as shown in Figure S1 of Appendix B. Consequently, the photonic band is an all-angle negative refraction band. Since two interpenetrating networks form a metal/insulator/metal waveguide, such light propagation is allowed in D-GYR metamaterials. Fig. 2d shows the polarization velocity field [35] of a positive refraction band (blue), Re[**v**], which corresponds to a coupled surface plasmon resonance. Each minority metal gyroid network has the anti-parallel electric currents of the other network and it is this coupled surface plasmon resonance phenomenon, which induces the propagation of light. Surprisingly each chiral gyroid strut allows its own circular polarized light propagation (see Figure S2 of Appendix B) [40]. Due to the existence of two opposite chiral struts, both left and right-handed circular polarizations can exist in D-GYR metamaterials.

In order to determine the importance of losses, we first calculated the band structure of lossy D-GYR metamaterials with a damping term, $\Gamma = 2\pi \times 5.79 \times 10^{12}\ Hz$, without consideration of inter-band transitions [37], in the eigensolver approach. The results are shown in Figure S3 of Appendix B and show no significant deviations from the case without losses (note that metallic loss neither affects the band structure nor the energy flux as shown in Figure S3 of Appendix B). Second, calculations were compared for the negative band indicated with an asterisk (*) in Fig. 4.2b using the finite element-based simulator COMSOL [36] for three different metals using experimental data of the dielectric function obtained from the literature: gold [41], silver [41] and aluminum [42]. As depicted in Fig. 4.3a and b, metamaterials with silver and aluminum, respectively, show the same energy flux direction as the Drude metal case. In contrast, strong absorption from inter-band transitions in gold, which is not taken into account in the Drude model, prevents negative refraction to occur in that band (see Fig. 4.3c). A strong frequency dispersion can change the direction of the group velocity [43]. Therefore, our calculations predict that low loss metals like silver need to be employed in the BCP self-assembly directed metamaterials described here to observe negative refraction in the visible range.

One advantage of BCP self-assembly is a facile control of the unit cell size, *a*, which can be achieved by changing BCP molar mass. For BCP D-GYR morphologies *a* typically ranges from *25 nm* to *150 nm* [31]. We calculated the refractive index of a positive refraction (blue in Fig. 4.2f) and a negative refraction (red) band for different unit cell sizes. The band structures are shown in the inset of Fig. 4.2g with varying *a*. Interestingly, the frequency range for the negative refraction barely changes with *a*. This result implies that decreasing the gap between the gyroid metal networks linearly increases the wave vector **k** at a fixed frequency. Physically, stronger coupling between surface plasmon resonances, *i.e.* larger capacitance, induces slower surface plasmon polariton propagation as in 1-dimensional metal/insulator/metal waveguides [30]. This phenomenon sets metallic D-GYR metamaterials apart from their dielectric photonic crystal (PC) counterparts, where the band frequencies scale with *a* and the refractive indices are independent of *a* [32, 44]. The results in Fig. 4.2f and g show that for the D-GYR metamaterials the refractive index is roughly inversely proportional to *a*. Therefore, the refractive index of both positive and negative refraction bands can be controlled through tuning BCP molar mass. Such phenomena originate from the characteristics of the surface plasmon resonances. For this reason, controlling the surface plasmon resonance should be a critical design factor for band structure control at low frequencies.

One can expect that the surface plasmon resonance frequency of D-GYR metamaterials can be governed by the capacitance of the two minority networks. A larger capacitance may lower the frequency range of the negative refraction band by slowing surface plasmon polariton propagation. Intuitively, a smaller gap between the gyroid minority networks is expected to increase the capacitance. One possible block copolymer structure to achieve this is the so-called core-shell D-GYR observed in tri-block terpolymers [45] where the shells surrounding the two equivalent gyroid minority networks (cores) will be replaced by metals. Instead, in the current work, we assumed a conformal metal deposition on both D-GYR minority networks after removal of the majority (matrix) block to ensure a shorter distance between two (hollow) metallic networks. The resulting hollow D-GYR metamaterial shown in the inset of Fig. 4.4a has a smaller metal volume fraction of *0.11*, as compared to *0.34* for the original structure. Fig. 4.4a shows its band structure for a unit cell size $a=100$ *nm*. As expected, negative refraction bands are observed in a lower frequency range (compare Fig. 4.2b and Fig. 4.4a).

Finally, we calculated the band structure of A-GYR metamaterials with $a=50$ *nm*, where only one minority network is converted into a metal as shown in the inset of Fig. 4.4b (note that for the same BCP molar mass, the unit cell size, *a*, of the A-GYR is approximately half the value of the D-GYR). Surprisingly, despite a much lower metallic volume fraction of *0.17*, than that of the D-GYR of *0.34*, such materials exhibit a metallic band gap at low frequencies [46] Due to the lack of a "counter electrode", low frequency light propagation from the coupled surface plasmon resonance observed in the D-GYRs becomes forbidden. In order to see far-field effects, further calculations were performed using COMSOL for an A-GYR slab composed of two unit cells with *a=100 nm* for gold, Drude and silver metals (note that this unit cell is twice as large as the one in Fig. 4.4b). The results of the COMSOL calculations in Fig. 4.3c show a broad peak of electric field polarization rotation below λ=*500 nm*, the frequency range of which coincides with the optically active range of the A-GYR band structure (losses in silver shift the peak and transmission/reflection spectra to longer wavelength as shown Fig. 4.3c and d). Furthermore, as expected in the D-GYR case, the chiral gyroid network in the A-GYR metamaterial induces a circular polarization.

In summary, we calculated the photonic bands of 3D periodic metallic nanomaterials with D-GYR and A-GYR morphologies, which experimentally can be fabricated, *e.g*. using block copolymer self-assembly followed by selective etching and subsequent metal deposition. For the D-GYR structure, coupled surface plasmon resonances induce light propagation at low frequencies. Negative refraction is predicted in the visible and near infrared regime for low loss metals like silver and aluminum but not for gold. Due to the chirality of the gyroid minority networks, circularly polarized light propagation is predicted. The results suggest critical design criteria for controlling photonic properties of such materials. We show that the refractive index and negative refraction frequencies of the resulting metamaterials are controlled by the structural parameters of these morphologies, which in turn can be tuned through the selection of polymer molar mass and block structure. For the A-GYR a surprising metallic band gap is observed at low frequencies. The unusual photonic behavior revealed in this theoretical work is caused by coupled surface plasmon resonances. The results suggest a significant potential for bottom-up type self-assembly toward metamaterials design and synthesis and identify specific design choices for experimental realizations of 3D isotropic negative index materials in the visible range. Cubic bicontinuous block copolymer network structures often have grain sizes of up to hundred micrometers or larger providing access to single crystal type structures for which the phenomena described here should be measurable [47, 48].

Acknowledgement

This publication is based on work supported in part by Award No. KUS-C1-018-02, made by King Abdullah University of Science and Technology (KAUST). The calculations have been performed using computational resources of the Computational Center for Nanotechnology Innovation (CCNI) at Rensselaer Polytechnic Institute. The work was further supported by the National Science Foundation through the Materials World Network grant between the US (DMR-1008125) and Great Britain (Engineering and Physical Sciences Research Council).

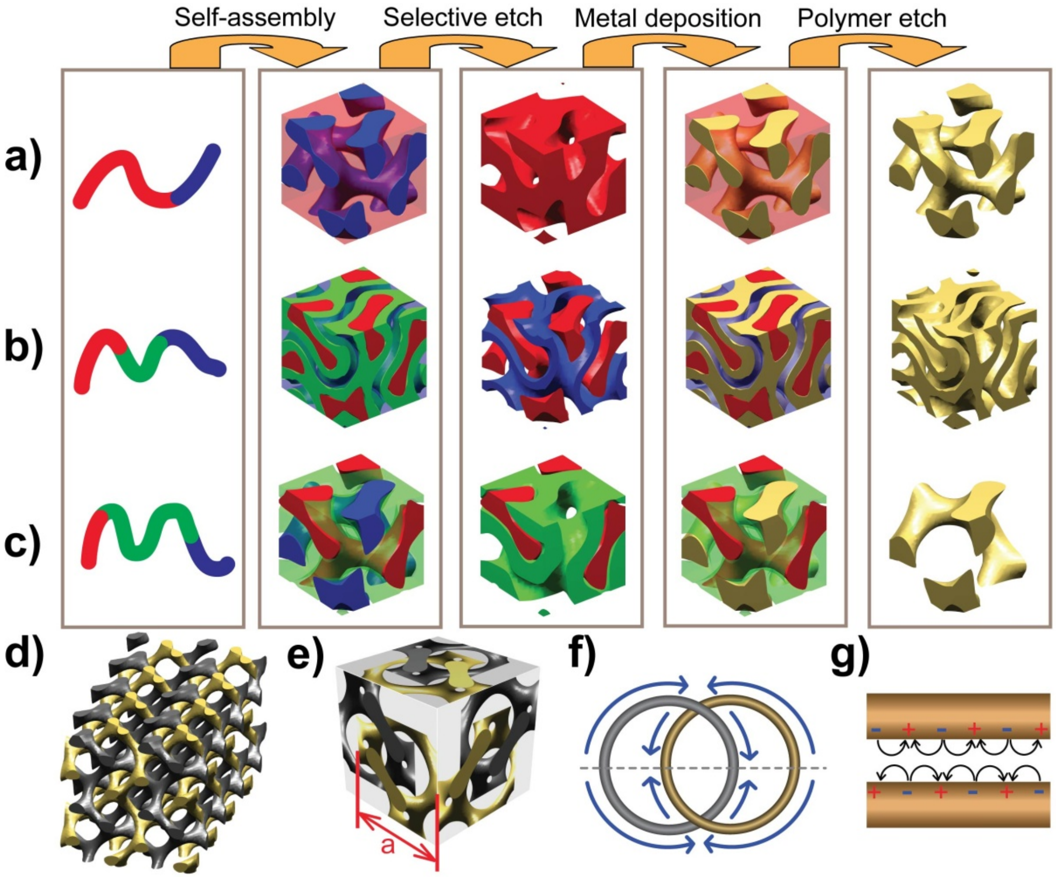

Figure 4.1. Schematic routes to 3-dimensionally co-continuous metamaterials with cubic symmetry and expected optical behavior. a) D-GYR; b) hollow D-GYR; and c) A-GYR metamaterials. For clarity of presentation, specific blocks are represented to be transparent. d) D-GYR metamaterial formed from many unit cells. The two chiral gyroid struts are depicted in different color for clarity. e) Projected images of a D-GYR metamaterial unit cell with unit cell length *a*onto three orthogonal axes. Two struts are cut in different planes for showing full loops. Surface plasmon plaritons (f) oscillate on the closed loop of gyroid networks and (g) on a 1-dimensional metal/insulator/metal wave-guide.

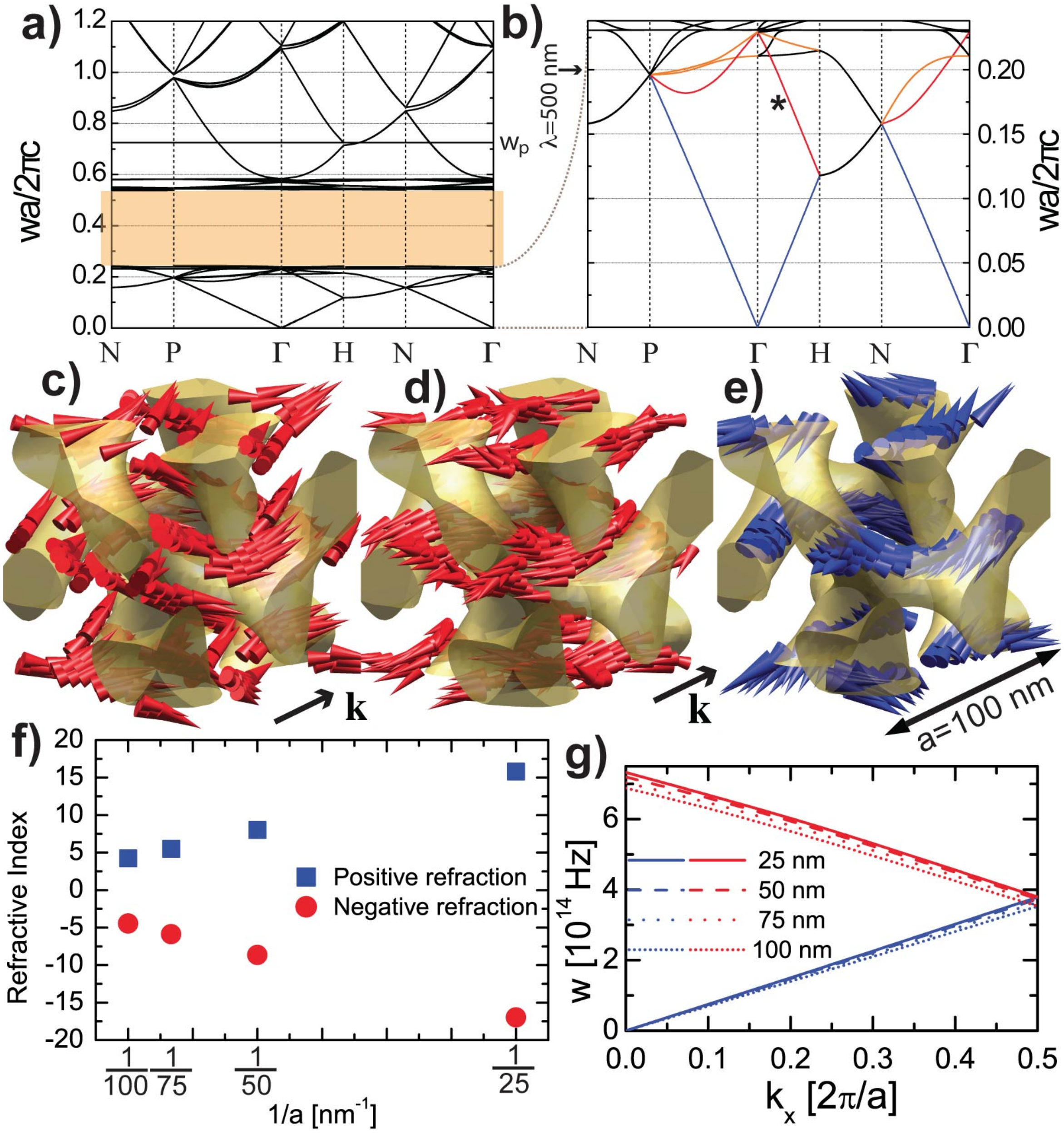
a)
b)
1.2
1.0
0.8
0.6
0.4
0.2
0.0
wa/2πc
w_p
λ=500 nm
0.20
0.15
0.10
0.05
0.00
*
N P Γ H N Γ
N P Γ H N Γ
c)
d)
e)
k
k
a=100 nm
f)
20
15
10
5
0
-5
-10
-15
-20
Refractive Index
Positive refraction
Negative refraction
1/100 1/75 1/50 1/25
1/a [nm^-1]
g)
w [10^14 Hz]
6
4
2
0
25 nm
50 nm
75 nm
100 nm
0.0 0.1 0.2 0.3 0.4 0.5
k_x [2π/a]

Figure 4.2. Results of band structure calculations using an eigensolver approach following Ref. [35] for D-GYR metamaterials made of a Drude metal with $a=100\ nm$ and the plasma frequency of gold, $\omega_p=2\pi\times2.19\times10^{15}\ Hz$ [37] a) Photonic band structure of D-GYR where the shaded region is filled with extremely dense flat bands. b) Expanded view for low frequency bands. Results show low frequency propagation bands including positive refraction (examples highlighted in blue) and negative refraction (examples highlighted in red for fast and in orange for slow bands, respectively). c) Energy flux, **S**, of the positive refraction band (blue) at **k**=[0.1,0,0]. d) **S** of the negative refraction band (asterisk) at **k**=[0.1,0,0]. e) Coupled plasmon resonance, Re[**v**], of the blue band at **k**=[0.1,0,0]. f) Refractive indices of two propagation bands (blue and red in b) obtained from Γ to H are roughly inversely proportional to the unit cell size, *a*. g) The band structure with varying *a*. The first Brillouin zone boundary is defined at Γ=[0,0,0], H=[0.5,0,0], N=[0.5,0.5,0], and P=[0.5,0.5,0.5]. All momentum vectors, **k**, have the unit, $2\pi/a$.

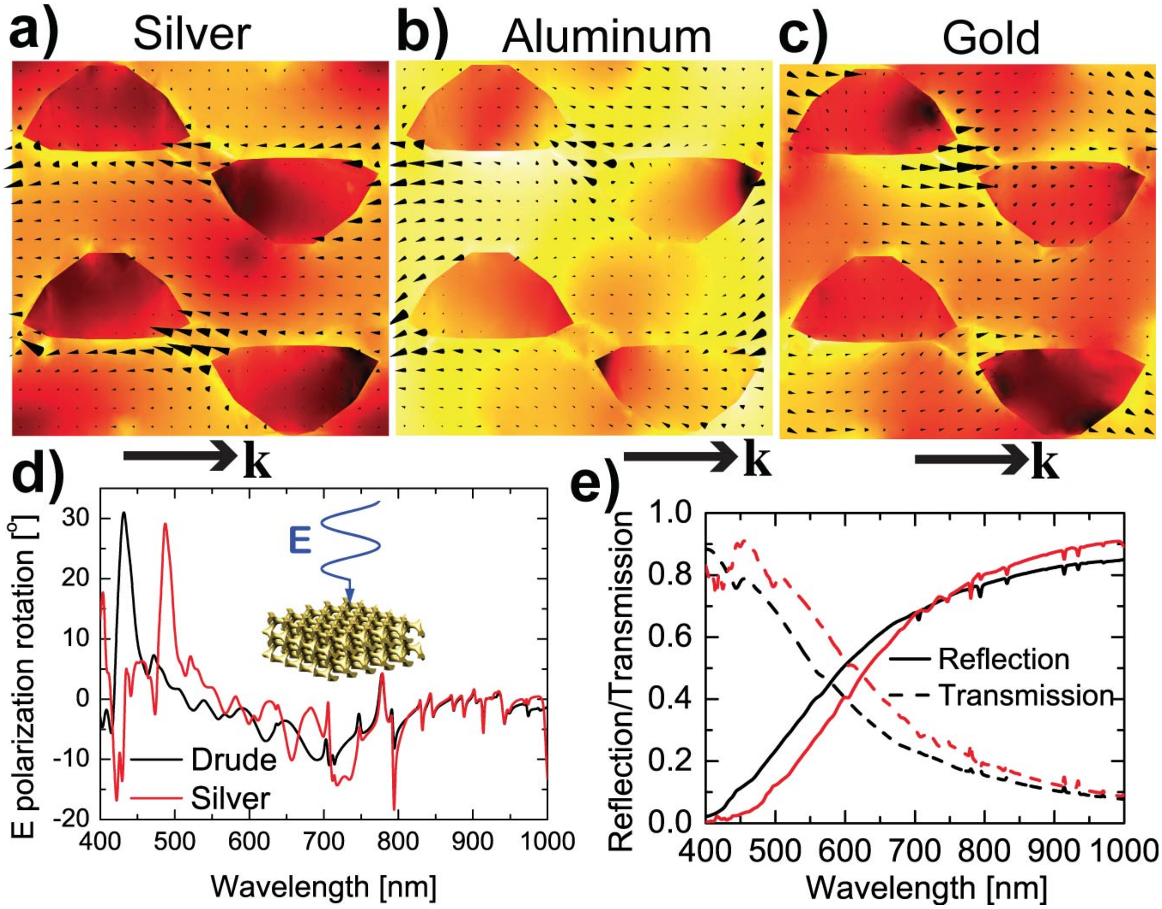

Figure 4.3. Results of finite element-based calculations using COMSOL. **a-c**, Normalized near-field profiles (yellow=1, black=0) and energy flux (arrows), **S**, of the negative band indicated with an asterisk in Fig. 4.2c at **k**=[0.1,0,0] for different metals (dielectric function from experimental data): silver (a), aluminum (b), and gold (c). Silver and aluminum show the same directional behavior of **S** calculated for gold in the Drude model (in which interband losses are not considered), while the direction of **S** in gold is positive due to strong losses from inter-band transitions. d) Far-field simulation results of a A-GYR slab composed of two unit cells with *a=100 nm* demonstrate electric field polarization rotation angle for the Au Drude metal (red) and silver (black). e) Reflectance (solid lines) and transmittance (broken lines) of the slab.

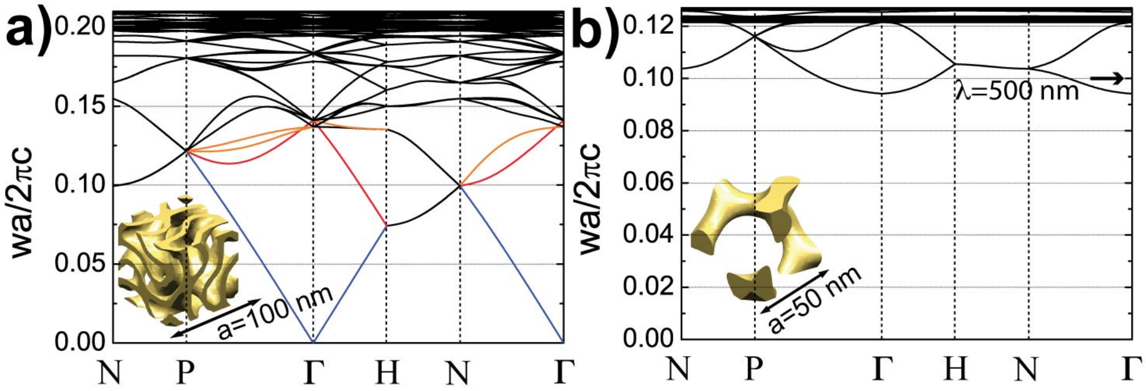

Figure 4.4. a) The photonic band structure of (a) a hollow D-GYR metamaterial with *a=100 nm* shows a lower onset frequency of the negative refraction than D-GYR metamaterials (compare results in **c** with those in Fig. 4.2**c**). The color code for (a) is the same as in Figure 4.2b) The metallic band gap of a A-GYR metamaterial with *a=50 nm* is observed in the photonic band structure up to *ωa/2πc=0.094*. The low frequency propagation bands are missing due to lack of a "counter electrode".

APPENDIX B

Angular dependence of the negative refraction band (red line in Fig. 4.2b). We showed negative refraction along Γ to H at $\mathbf{k}=\left[0.1,0,0\right]$ in Fig. 4.2d. In order to check angular dependence of the negative refraction band, the Poynting vectors $\mathbf{S}=1/2\,\mathrm{Re}\left[\mathbf{E}\times\mathbf{H}^{*}\right]$ for other directions, Γ to N at $\mathbf{k}=\left[0.1,0.1,0\right]$ and Γ to P at $\mathbf{k}=\left[0.1,0.1,0.1\right]$, are shown in Fig. S1a and b of Appendix B, respectively. Consequently, the photonic band (red line in Fig. 4.2b) is an all-angle negative refraction band.

Ciruclar dichroism. Fig. S2 of Appendix B demonstrates the magnetic fields, $\mathrm{Re}\left[\mathbf{H}\,\mathrm{e}^{i\delta}\right]$, of the negative refraction band (red line in Fig. 4.2b) at $\mathbf{k}=\left[0.4,0,0\right]$ for different time steps, δ. The time evolution of magnetic fields demonstrates that each metal gyroid struts allow either left or right circularly polarized light propagation. Therefore, D-GYR metamaterial has both struts and is expected to have no circular dichroism. In contrast, A-GYR metamaterial, which has only one gyroid strut, is expected to have circular dichroism.

Methods

Self-consistent field theory calculations. For the D-GYR, we simulated A-*b*-B di-BCPs with overall volume fraction of block A, $f_A = 0.32$, and product of the Flory-Huggins interaction parameter with the number of monomers along the BCP chain, $\chi N = 40$ [33]. SCFT simulations yield the local volume fractions of all blocks at each position $\mathbf{r}$, $\varphi(\mathbf{r})$. The metallic regions were set from the local volume fraction of block A, $\varphi_A(\mathbf{r})$, with $\varphi_A(\mathbf{r}) \geq 0.5$ for D-GYR and $0.1 \leq \varphi_A(\mathbf{r}) \leq 0.5$ for the hollow D-GYR (note that $\varphi_A(\mathbf{r})$ decreases with moving away from the gyroid cores and thus the hollow D-GYR defined at smaller $\varphi_A(\mathbf{r})$ has a shorter strut-to-strut distance than the D-GYR does). For the A-GYR, we simulated poly(isoprene-*b*-styrene-*b*-ethylene oxide) (ISO) with the overall volume fractions of each blocks, $f_I = 0.28$, $f_S = 0.57$, and $f_O = 0.15$. The other simulation parameters such as χN and the Kuhn lengths are taken from Ref. [45]. The metallic regions were determined from the local volume fraction of the polyethylene oxide block, $\varphi_O(\mathbf{r})$, with $\varphi_O(\mathbf{r}) \geq 0.3$. Other regions were set to be vacuum.

Photonic band calculations. The photonic band structures were calculated from Maxwell's equations for dispersive materials following Ref. [35], with a frequency-dependent dielectric function $\varepsilon(w) = 1 - \frac{w_p^2}{w^2 - iw\Gamma}$. For the metal regions, we used a

Drude metal with the plasma frequency of gold, $w_p = 2\pi \times 2.19 \times 10^{15} Hz$ [37] and initially set the loss term, Γ, to zero. In order to determine the importance of losses, we subsequently calculated the band structure of lossy D-GYR metamaterials with $\Gamma = 2\pi \times 5.79 \times 10^{12} Hz$ [37]. The results are shown in Fig. S3 of Appendix B and show no significant deviations from the case without losses. All simulations were performed using a grid of 32×32×32 points.

Finite element-based calculations. Results were compared with full 3D electrodynamic calculations using finite element-based software COMSOL [36] for a Drude fit to the dielectric function of gold (thus underestimating losses in the visible due to interband transitions) shown in Figure S4 of Appendix B, as well as for the measured dielectric functions [49] for gold [41], silver [41] and aluminum [42]. A maximum mesh step of 1 nm was used across the whole unit cell.

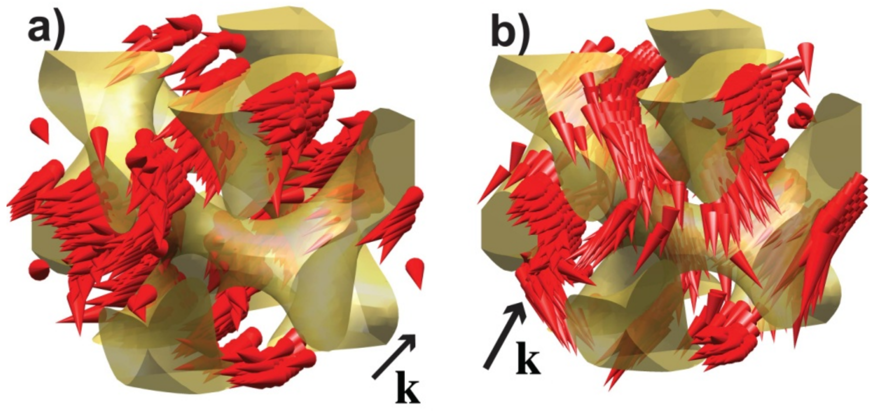

Figure S1. The energy flux, $\mathbf{S} = 1/2\,\mathrm{Re}\left[\mathbf{E}\times\mathbf{H}^*\right]$, of the negative refraction band (red line in Fig. 2b) along a) Γ to N at $\mathbf{k} = \left[0.1, 0.1, 0\right]$ and b) Γ to P at $\mathbf{k} = \left[0.1, 0.1, 0.1\right]$. The energy flux has opposite directions to their momentum vectors. These results clearly show the photonic band is an all-angle negative refraction band.

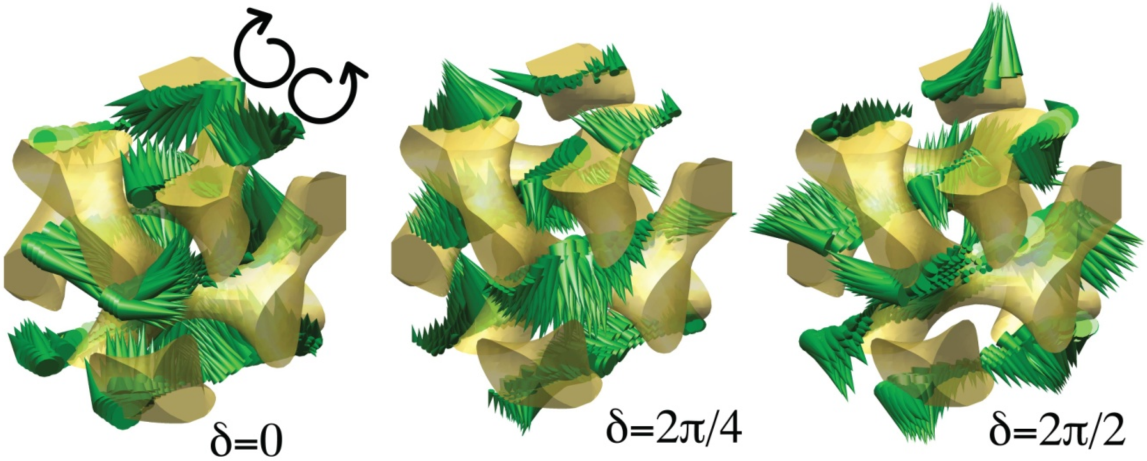

Figure S2. Magnetic fields, $\mathrm{Re}\left[\mathbf{H}\mathrm{e}^{i\delta}\right]$, of the negative refraction band (asterisk) at $\mathbf{k}=\left[0.4,0,0\right]$ in Fig. 2b for different time steps, δ. Each chiral gyroid strut has its own circular polarized light propagation. The magnetic field evolution in time demonstrates left and right circular dichroism for each gyroid struts.

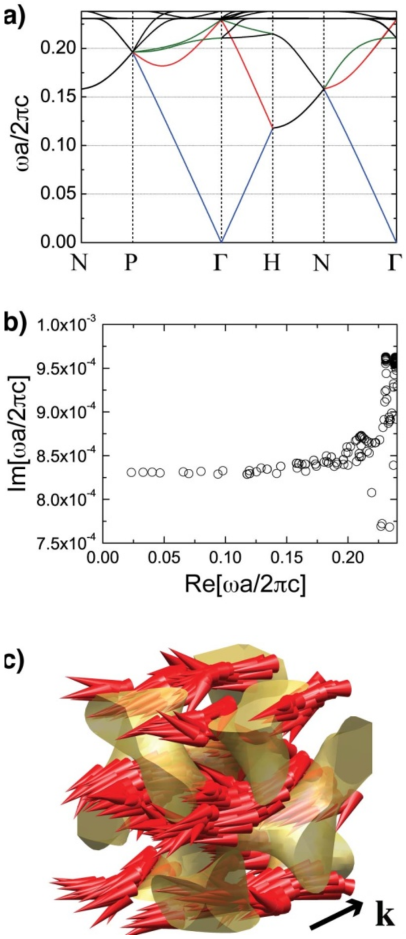

Figure S3. Results of calculations using an eigensolver approach. Lossy D-GYR metamaterials with $a = 100nm$ and $\Gamma = 2\pi \times 5.786 \times 10^{12} Hz$ show the same band structure with lossless D-GYR metamaterials (compare with Fig. 2C). Neither the direction of energy flow $\mathbf{S}$ nor the band diagram is affected by metal loss. The color code for (a) is the same as in Figures 2 and 4. a) Photonic band structure. b) Imaginary part of ω for each frequency ω. Close values are obtained considering the experimental dielectric function of silver. c) Energy flux, $\mathbf{S}$, of the negative refraction band (red) at $\mathbf{k} = \left[0.1, 0, 0\right]$ with the unit, $2\pi / a$. Note that for these modes Im(ω) is very small .

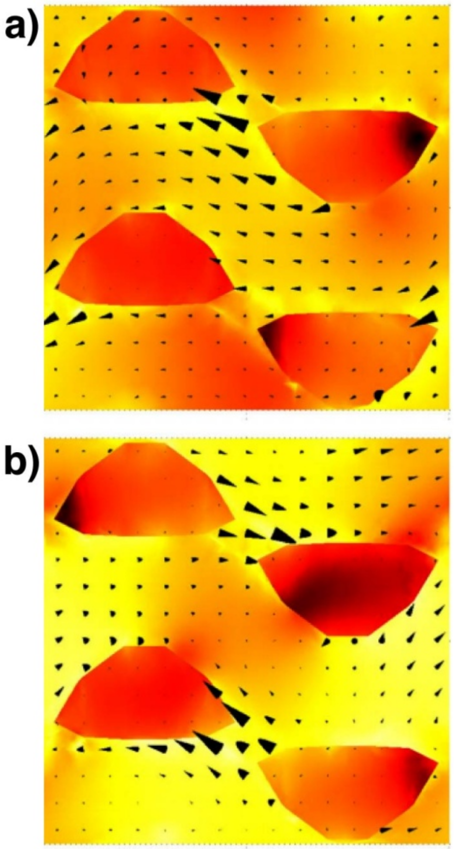

Figure S4. Results of calculations using finite element-based software COMSOL. Normalized near-field profiles (yellow=1, black=0) and Poynting vector (arrows) for a) $\omega=0.21$, where negative refraction can be observed, and b) $\omega=0.36$, case of a flat band that leads to a localized state, at $\mathbf{k}=\left[0.1,0,0\right]$.

REFERENCES

[1] J. B. Pendry, A. J. Holden, D. J. Robbins, W. J. Stewart, Magnetism from conductors and enhanced nonlinear phenomena. *Microwave Theory and Techniques, IEEE Transactions on* **47** (11), 2075-2084 (1999).

[2] D. R. Smith, W. J. Padilla, D. C. Vier, S. C. Nemat-Nasser, S. Schultz, Composite Medium with Simultaneously Negative Permeability and Permittivity. *Phys. Rev. Lett.* **84** (18), 4184 (2000).

[3] R. A. Shelby, D. R. Smith, S. Schultz, Experimental Verification of a Negative Index of Refraction. *Science* **292** (5514), 77-79 (April 6, 2001, 2001).

[4] S. P. Burgos, R. de Waele, A. Polman, H. A. Atwater, A single-layer wide-angle negative-index metamaterial at visible frequencies. *Nat. Mater.* **9** (5), 407-412 (2010).

[5] E. Verhagen, R. de Waele, eacute, L. Kuipers, A. Polman, Three-Dimensional Negative Index of Refraction at Optical Frequencies by Coupling Plasmonic Waveguides. *Phys. Rev. Lett.* **105** (22), 223901 (2010).

[6] N. Liu, H. Giessen, Coupling Effects in Optical Metamaterials. *Angew. Chem. Int. Ed.* **49** (51), 9838-9852 (2010).

[7] V. G. Veselago, THE ELECTRODYNAMICS OF SUBSTANCES WITH SIMULTANEOUSLY NEGATIVE VALUES OF ε AND μ. *Sov. Phys. Usp.* **10** (4), 509 (1968).

[8] J. B. Pendry, Negative Refraction Makes a Perfect Lens. *Phys. Rev. Lett.* **85** (18), 3966 (2000).

[9] J. B. Pendry, D. Schurig, D. R. Smith, Controlling Electromagnetic Fields. *Science* **312** (5781), 1780-1782 (2006).

[10] N. Liu, H. Guo, L. Fu, S. Kaiser, H. Schweizer, H. Giessen, Three-dimensional photonic metamaterials at optical frequencies. *Nat. Mater.* **7** (1), 31-37 (2008).

[11] M. S. Rill, C. Plet, M. Thiel, I. Staude, G. von Freymann, S. Linden, M. Wegener, Photonic metamaterials by direct laser writing and silver chemical vapour deposition. *Nat. Mater.* **7** (7), 543-546 (2008).

[12] K. J. Stebe, E. Lewandowski, M. Ghosh, Oriented Assembly of Metamaterials. *Science* **325** (5937), 159-160 (2009).

[13] N. I. Zheludev, The Road Ahead for Metamaterials. *Science* **328** (5978), 582-583 (2010).

[14] Q. Liu, Y. Cui, D. Gardner, X. Li, S. He, I. I. Smalyukh, Self-Alignment of Plasmonic Gold Nanorods in Reconfigurable Anisotropic Fluids for Tunable Bulk Metamaterial Applications. *Nano Lett.* **10** (4), 1347-1353 (2010).

[15] S. C. Warren, L. C. Messina, L. S. Slaughter, M. Kamperman, Q. Zhou, S. M. Gruner, F. J. DiSalvo, U. Wiesner, Ordered Mesoporous Materials from Metal Nanoparticle-Block Copolymer Self-Assembly. *Science* **320** (5884), 1748-1752 (June 27, 2008, 2008).

[16] M. Kamperman, U. Wiesner, *Bioinspired Block Copolymer-Based Hybrid Materials in "The Supramolecular Chemistry of Organic-Inorganic Hybrid Materials"*. The Supramolecular Chemistry of Organic-Inorganic Hybrid Materials (John Wiley & Sons, Inc., 2010), pp. 599-636.

[17] A. H. Schoen, *Infinite periodic minimal surfaces without self-intersections*. (National Aeronautics and Space Administration; [for sale by the Clearinghouse for Federal Scientific and Technical Information, Springfield, Va.], Washington, 1970).

[18] S. Leoni, I. A. Baburin, On the continuous transformations between genus-3 minimal surfaces approximants. *Z. Kristallogr.* **226** (8), 678-683 (2011/08/01, 2011).

[19] R. E. Newnham, *Properties of materials: anisotropy, symmetry, structure*. (Oxford University Press, 2005).

[20] D. A. Hajduk, P. E. Harper, S. M. Gruner, C. C. Honeker, G. Kim, E. L. Thomas, L. J. Fetters, The Gyroid: A New Equilibrium Morphology in Weakly Segregated Diblock Copolymers. *Macromolecules* **27** (15), 4063-4075 (1994).

[21] V. Z.-H. Chan, J. Hoffman, V. Y. Lee, H. Iatrou, A. Avgeropoulos, N. Hadjichristidis, R. D. Miller, E. L. Thomas, Ordered Bicontinuous Nanoporous and Nanorelief Ceramic Films from Self Assembling Polymer Precursors. *Science* **286** (5445), 1716-1719 (November 26, 1999, 1999).

[22] B.-K. Cho, A. Jain, S. M. Gruner, U. Wiesner, Mesophase Structure-Mechanical and Ionic Transport Correlations in Extended Amphiphilic Dendrons. *Science* **305** (5690), 1598-1601 (September 10, 2004, 2004).

[23] E. J. W. Crossland, M. Kamperman, M. Nedelcu, C. Ducati, U. Wiesner, D. M. Smilgies, G. E. S. Toombes, M. A. Hillmyer, S. Ludwigs, U. Steiner, H. J. Snaith, A Bicontinuous Double Gyroid Hybrid Solar Cell. *Nano Lett.* **9** (8), 2807-2812 (2008).

[24] Y. Grin, U. Wedig, H. G. von Schnering, Hyperbolic Lone Pair Structure in RhBi4. *Angew. Chem. Int. Ed. Engl.* **34** (11), 1204-1206 (1995).

[25] R. Pöttgen, V. Hlukhyy, A. Baranov, Y. Grin, Crystal Structure and Chemical Bonding of Mg3Ru2. *Inorg. Chem.* **47** (13), 6051-6055 (2008).

[26] T. Hahn, H. Wondratschek, U. Müller, International Union of Crystallography., *International tables for crystallography*. (Published for the International Union of Crystallography by Kluwer Academic Publishers, Dordrecht Boston, ed. 5th, 2002), pp. v.

[27] H.-Y. Hsueh, Y.-C. Huang, R.-M. Ho, C.-H. Lai, T. Makida, H. Hasegawa, Nanoporous Gyroid Nickel from Block Copolymer Templates via Electroless Plating. *Adv. Mater. (Weinheim, Ger.)* **23** (27), 3041-3046 (2011).

[28] A. Radke, T. Gissibl, T. Klotzbücher, P. V. Braun, H. Giessen, Three-Dimensional Bichiral Plasmonic Crystals Fabricated by Direct Laser Writing and Electroless Silver Plating. *Adv. Mater. (Weinheim, Ger.)* **23** (27), 3018-3021 (2011).

[29] M. M. Sigalas, C. T. Chan, K. M. Ho, C. M. Soukoulis, Metallic photonic band-gap materials. *Phys. Rev. B* **52** (16), 11744 (1995).

[30] B. Prade, J. Y. Vinet, A. Mysyrowicz, Guided optical waves in planar heterostructures with negative dielectric constant. *Phys. Rev. B* **44** (24), 13556 (1991).

[31] A. J. Meuler, M. A. Hillmyer, F. S. Bates, Ordered Network Mesostructures in Block Polymer Materials. *Macromolecules* **42** (19), 7221-7250 (2009).

[32] M. Maldovan, A. M. Urbas, N. Yufa, W. C. Carter, E. L. Thomas, Photonic properties of bicontinuous cubic microphases. *Phys. Rev. B* **65** (16), 165123 (2002).

[33] M. W. Matsen, M. Schick, Stable and unstable phases of a diblock copolymer melt. *Phys. Rev. Lett.* **72** (16), 2660 (1994).

[34] K. Hur, R. G. Hennig, F. A. Escobedo, U. Wiesner, Mesoscopic structure prediction of nanoparticle assembly and coassembly: Theoretical foundation. *J. Chem. Phys.* **133** (19), 194108-194112 (2010).

[35] A. Raman, S. Fan, Photonic Band Structure of Dispersive Metamaterials Formulated as a Hermitian Eigenvalue Problem. *Phys. Rev. Lett.* **104** (8), 087401 (2010).

[36] http://www.comsol.com.

[37] M. A. Ordal, L. L. Long, R. J. Bell, S. E. Bell, R. R. Bell, J. R. W. Alexander, C. A. Ward, Optical properties of the metals Al, Co, Cu, Au, Fe, Pb, Ni, Pd, Pt, Ag, Ti, and W in the infrared and far infrared. *Applied Optics* **22** (7), 1099-1119 (1983).

[38] J. B. Pendry, Calculating photonic band structure. *J. Phys.: Condens. Matter* **8** (9), 1085 (1996).

[39] J. D. Jackson, *Classical electrodynamics*. (Wiley, New York, ed. 3rd, 1999), pp. xxi, 808 p.

[40] J. K. Gansel, M. Thiel, M. S. Rill, M. Decker, K. Bade, V. Saile, G. von Freymann, S. Linden, M. Wegener, Gold Helix Photonic Metamaterial as

Broadband Circular Polarizer. *Science* **325** (5947), 1513-1515 (September 18, 2009, 2009).

[41] P. B. Johnson, R. W. Christy, Optical Constants of the Noble Metals. *Phys. Rev. B* **6** (12), 4370 (1972).

[42] A. D. Raki, Algorithm for the determination of intrinsic optical constants of metal films: application to aluminum. *Appl. Opt.* **34** (22), 4755-4767 (1995).

[43] G. Dolling, C. Enkrich, M. Wegener, C. M. Soukoulis, S. Linden, Simultaneous Negative Phase and Group Velocity of Light in a Metamaterial. *Science* **312** (5775), 892-894 (May 12, 2006, 2006).

[44] J. D. Joannopoulos, *Photonic crystals : molding the flow of light*. (Princeton University Press, Princeton, ed. 2nd, 2008), pp. xiv, 286 p.

[45] C. A. Tyler, J. Qin, F. S. Bates, D. C. Morse, SCFT Study of Nonfrustrated ABC Triblock Copolymer Melts. *Macromolecules* **40** (13), 4654-4668 (2007).

[46] V. Kuzmiak, A. A. Maradudin, F. Pincemin, Photonic band structures of two-dimensional systems containing metallic components. *Phys. Rev. B* **50** (23), 16835 (1994).

[47] A. C. Finnefrock, R. Ulrich, A. Du Chesne, C. C. Honeker, K. Schumacher, K. K. Unger, S. M. Gruner, U. Wiesner, Metal Oxide Containing Mesoporous Silica with Bicontinuous “Plumber's Nightmare” Morphology from a Block Copolymer–Hybrid Mesophase. *Angew. Chem. Int. Ed.* **40** (7), 1207-1211 (2001).

[48] A. C. Finnefrock, R. Ulrich, G. E. S. Toombes, S. M. Gruner, U. Wiesner, The Plumber's Nightmare:1 A New Morphology in Block Copolymer−Ceramic

Nanocomposites and Mesoporous Aluminosilicates. *J. Am. Chem. Soc.* **125** (43), 13084-13093 (2003).

[49] E. D. Palik, G. Ghosh, *Handbook of optical constants of solids*. (Academic Press, [London], 1998).

CHAPTER 5

Complete surface plasmon band gaps in 3-dimensional hierarchical metamaterials[4]

ABSTRACT

Surface plasmons are collective oscillations of electrons in nanoscale metallic materials. Materials harnessing surface plasmon phenomena enable unusual photonic applications including metamaterials, therapeutics, terahertz computing and solar cells. Due to the complexity of light-matter interactions intuitive insights into the optical behavior particularly of metamaterials are challenging. Utilizing numerical simulations here we studied various continuous and dis-continuous metallic nanomaterials and compared them with their photonic crystal counterparts. Metallic nanomaterials with the diamond cubic symmetry ($Fd\overline{3}m$) display both, complete surface plasmon band gaps as well as negative refraction in 3-dimensions. Results allow in-depth understanding of and provide design criteria for metallic nanomaterials for plasmonic applications.

---

[4] Kahyun Hur, Richard G. Hennig, and Ulrich Wiesner; to be submitted

5.1. Introduction

Explosive growth of nanophotonics research is transforming our understanding of photonics and stimulating research in various scientific communities ranging from the physical sciences to chemistry and biology [1-7]. Recent advances in metamaterials and plasmonics are moving various photonic applications to sub-diffraction-limited scales [1, 3, 5]. A metamaterial is an engineered material that exhibits unusual optical properties that may not be found in nature. One such phenomenon is the negative refractive index of a material, which has attracted much attention as it may enable, e.g., unlimited resolution imaging [1]. Despite such potential of metamaterials for various applications, fundamental understanding of light-mater interactions in nanoscale metallic materials needs to be further developed. For example, both, metamaterials and photonic crystals, may have periodic structures but their photonic behavior is quite distinct [8]. In this work we calculated photonic band structures of various cubic metamaterials and photonic crystals [9], composed of metallic and dielectric materials. Three-dimensional (3D) complete surface plasmon band gaps are identified in continuous metamaterials with the diamond cubic structure, space group Q^{227} ($Fd\overline{3}m$), and a metal/insulator/metal substructure. Furthermore, the materials simultaneously exhibit negative refraction. Differences of light-matter interactions between metamaterials and photonic crystals are studied and design criteria are developed to realize these properties in nanomaterials.

Photonic crystals are materials with a periodic structure composed of two or more materials with differing permittivity [9]. The flow of light is controlled by the modulation of dielectric materials and for some specific structures such as the diamond cubic structure [10] the destructive interference of light waves leads to photonic band gaps in certain frequency ranges where light cannot propagate. A 3-dimensional photonic band gap prohibiting any light propagation along any direction is called a complete photonic band gap. Compared with photonic crystals, metamaterials are similarly periodic but usually composed of metallic materials [11]. In metals, the existence of plasmons, i.e. oscillations of free electron density, leads to fundamentally different light-matter interactions than in photonic crystals [12]. The plasmons in metamaterial enable the manipulation of the propagation of photons with much larger wavelength than the lattice size of the material, while in photonic crystals the photon wavelength and the lattice size should be comparable in size [8]. Therefore, metamaterials have both similarities and dissimilarities with photonic crystals.

To date quantitative comparisons between these two classes of materials, are rare, mostly because different computationally techniques are better suited for each case. In order to minimize computational cost, planewave basis sets have been preferentially used for calculating photonic band structures [13]. Planewave basis sets, however, are not well suited for capturing surface plasmon resonances in metallic materials. Time domain simulations are usually efficient for solving Maxwell's equations [14] but unable to resolve even number degenerate bands [13]. Therefore, here we used a finite difference approach with Yee grids to ensure divergence free behavior, $\nabla \cdot \mathbf{E} = 0$, and ARPACK [15] as an eigenvalue solver for band structure calculations of both metamaterials and photonic crystals. For materials parameters, a Drude metal was assumed for most cases with a plasma frequency, $\omega_p=1.366\times10^{16}$ *Hz*, i.e. the value for silver [16]. The unit cell length of the metamaterials was fixed at *a=400 nm*.

Photonic band structures of various cubic structures obtained from constant mean curvature surfaces have been studied by Maldovan *et al.* [10, 17]. Such cubic structures are very interesting since some of them can be realized by block copolymer self-assembly [18, 19] and colloidal self-assembly [20]. The optical properties of metamaterials with alternating gyroid ($I4_132$) and double gyroid ($Ia\bar{3}d$) structures have also been studied [21]. Since they can be fabricated using bottom-up type block copolymer self-assembly [22], this may enable cost-effective fabrication of 3D metamaterials.

We calculated photonic band structures of metamaterials with the diamond cubic symmetry ($Fd\bar{3}m$). In particular we varied their substructure to observe substructure effects on optical properties (see Appendix C for detailed structure building). Compared to photonic crystals, which have photonic band gaps, metamaterial counterparts exhibit very distinct optical behavior showing surface plasmon bands. Interestingly, the calculated band structures of metamaterials depend strongly on their substructure. For comparison we studied other metamaterials with differing symmetries, e.g. the alternating gyroid structure ($I4_132$), thereby elucidating design criteria to obtain interesting optical properties.

5.2. Results and Discussion

Fig. 5.1 shows the calculated photonic bands of the diamond cubic photonic crystal and metamaterials. The diamond cubic photonic crystal has a complete photonic band gap as predicted by Maldovan *et al.* [10]. Depending on the substructure, i.e. absence of substructure (Fig. 5.1b), coaxial metal/insulator/metal geometry (Fig. 5.1c) or double gyroid network (Fig. 5.1d), the band structure of the metamaterials changes quite dramatically. Without any substructure, the single continuous network has a metallic band gap at lower frequencies as observed earlier in alternating gyroid metamaterials, a single network with Q^{214} space group ($I4_132$) [21]. Such a metallic band gap originates from the electric current conservation in the material (see Appendix C for the proof). Therefore, low frequency bands of 3D continuous metamaterials require two or more networks to form an active band at low frequencies to meet the electric current conservation rule. This criterion is clearly found in other 3D diamond structures that have two continuous networks such as the coaxial and double gyroid network substructures forming a metal/insulator/metal waveguide allowing active acoustic bands at low frequencies. At somewhat higher frequencies, complete band gaps are found in the diamond metamaterials with the coaxial and double gyroid network substructures similar to what is obtained in diamond photonic crystals [10]. In contrast to the photonic band gap of diamond cubic photonic crystals [10], the band gaps in the metamaterials are surface plasmon band gaps, where energy carriers are surface plasmons (see discussions in the next paragraph). While two-dimensional (2D) band gap materials were evidenced experimentally [23], to the best of our knowledge 3D complete surface plasmon band gap materials have not yet been identified neither experimentally nor theoretically. Interestingly, the coaxial and double gyroid substructures yield structurally similar low frequency bands despite very different substructure shapes. Fundamentally, in both structures two independent networks form a surface plasmonic waveguide and electromagnetic waves with large wavelength, i.e. low frequency bands, are not strongly affected by the short-range structures. Therefore, one can expect that, for fixed symmetry, structures forming a metal/insulator/metal waveguide have similar low frequency band structures in different metamaterials. The variation of the waveguide geometry changes surface plasmon propagation velocity, where the double gyroid waveguide induces slower propagation than the coaxial waveguide due to larger surface area thereby forming a larger capacitor. Such slower propagation in a lager capacitance waveguide was also observed in double gyroid metamaterials [21]. Meanwhile, higher frequency bands have different structures. Due to the comparable plasmon wavelength to the substructural length scale in this frequency range, the substructures affect the band structure significantly.

Photonic bands and surface plasmon bands are very distinct due to their different physical origin. Photons have two degrees of freedom with two transverse bands in the divergence free condition, $\nabla \cdot \mathbf{E} = 0$ (note that transverse electric and transverse magnetic bands exist in 2D). In 3D cubic photonic crystals the two bands are degenerate due to the symmetry of materials as indicated in Fig. 5.1a. In contrast, surface plasmon bands are not degenerate (there exists only one acoustic band in Fig. 5.1c and d). In metamaterials, the degeneracy of the photonic band is broken due to the Fano resonance [24] forming two non-degenerate bands in nanometallic materials systems. The low frequency bands in the diamond photonic crystal are split into two sets of the low frequency surface plasmon bands (compare the photonic bands with $\omega a/2\pi c<0.45$ in Fig. 5.1a and the surface plasmon bands with $\omega a/2\pi c<0.45$ in Fig. 5.1c). Surface plasmon bands are intrinsically longitudinal in that surface plasmons exist only on metal/insulator interfaces and electro-magnetic waves propagate along the interfaces, where $\nabla \cdot \mathbf{E} = 0$ is not necessarily zero. The non-degeneracy of surface plasmon bands discriminates them from photonic bands in 3D.

Next we took a detailed look at the photonic energy flows in these materials. Fig. 5.2 shows the energy fluxes for two different bands at $\omega a/2\pi c=0.013$ (positive refraction band) and 0.22 (negative refraction band) of the metamaterial with double gyroid substructure. The majority of the photonic energy flows through the double gyroid networks that form a metal/insulator/metal waveguide. Here the energy carriers are surface plasmons leading to fundamental differences in propagation of light from photonic crystals, where photons are the energy carriers. Since surface plasmons can have much shorter wavelengths than photons at the same frequencies, metallic materials can manipulate light of much larger wavelength than what one might expect from the characteristic structural length scales of the materials. Similar to the case of simple double gyroid metamaterials [21], the present hierarchical metamaterial has negative refraction bands. It acts as a metamaterial in a wavelength regime, $\lambda=1700\sim3100\ nm$, that is larger than the characteristic unit cell size of the cubic gyroid lattice, $a=400\ nm$.

We further studied the near-field characteristics of the photonic and surface plasmon bands. It is known that plasmonic materials have very large scattering cross sections [25]. This is due to surface plasmons interacting with photons. In photonic crystals the photonic energy is concentrated in the higher dielectric material for lower frequency bands and the lower dielectric material for higher frequency bands [9]. In contrast surface plasmons only exist on metallic surfaces and photonic energies are concentrated on the surfaces for metamaterials. Such near-field behavior is shown in Fig. 5.3. The surface plasmon bands generally have high magnetic fields near metallic surfaces compared to the photonic bands (compare the relative strength of magnetic fields in Fig. 5.3 for the diamond metamaterial and photonic crystal). In particular, the highest magnetic fields are found in the metal/insulator/metal waveguide forming a capacitor in the metamaterial (see Fig. 5.3a). The behavior is consistent with the observation that photonic energy flows through the waveguide as shown in Fig. 5.2.

Fixing the space group of the larger length scale lattice to the diamond cubic structure ($Fd\overline{3}m$), the photonic band structures were calculated for hierarchical metamaterials with a disconnected minority double gyroid substructure (see Fig. 5.4c) and a connected majority double gyroid substructure (see Fig. 5.4d), respectively. The acoustic band of the discontinuous diamond structure shown in Fig. 5.4c is doubly degenerate. In contrast, the continuous structure in Fig 5.4d results exclusively in non-degenerate bands. In the disconnected case surface plasmons can no longer propagate due to the missing connectivity of the substructure and photons become the energy carriers. As a result, the optical characteristics of such discontinuous metallic structures are similar to those of photonic crystals.

Losses may change the overall shape of the photonic band structure. In order to consider the effect of losses, photonic band structure of the diamond cubic metamaterial with coaxial geometry was calculated replacing the Drude metal with gold. We utilized optical parameters of gold given by Vial *et al.* that nicely reproduce experimental results of nanoscale gold structures [22]. Overall band shapes at low frequencies did not change, compare results in Figs. 5.1c and 5.5a. Instead, for gold, the frequencies of the photonic bands shifted to lower frequencies.

Having studied hierarchical metamaterials with diamond superstructure, we moved to materials with alternating gyroid superstructure, space group Q^{214} ($I4_132$). An alternating gyroid metamaterial was previously predicted to have a metallic band gap [21] which was experimentally observed [22]. The alternating gyroid metamaterial with a double gyroid substructure shown in Fig. 5.6b has an active surface plasmon band. Therefore, the criterion for 3D continuous metallic materials that more than one network is required to have active bands at low frequencies holds for the hierarchical alternating gyroid case. For the alternating gyroid photonic crystal, a photonic band gap exists as shown in Fig. 5.6a and Ref. [17]. For the case of the metamaterial with the double gyroid substructure, however, no surface plasmon band gap was found. Therefore, not all photonic band gap structures exhibit surface plasmon band gaps in their metamaterial counterparts.

In summary, we calculated the photonic band structures of various metamaterials with cubic symmetries. The diamond cubic metamaterials with coaxial geometry and double gyroid substructure have both, a surface plasmon band gap and negative refractive index. The fundamental differences between surface plasmon bands and photonic bands are identified, where acoustic photonic bands are doubly degenerate in 3D but acoustic surface plasmon bands are not degenerate. Further near-field characteristics are compared between metamaterials and photonic crystals. Compared to photonic crystals, metamaterials have very concentrated energies near metallic surfaces and photonic energy flows through the surfaces in the materials. Losses don't alter the overall band structure but shift bands to lower frequencies for the case of gold. Interestingly, alternating gyroid metamaterials having a metallic band gap at low frequencies without any substructure, exhibit an active acoustic surface plasmon band. We expect that our theoretical work will help better understand the behavior of surface plasmons in nanostructured metallic materials and provide an impetus for future research on metamaterials and nanophotonics.

Acknowledgements

This publication is based on work supported in part by Award No. KUS-C1-018-02, made by King Abdullah University of Science and Technology (KAUST). The work was further supported by the National Science Foundation through the Materials World Network grant between the US (DMR-1008125) and Great Britain (Engineering and Physical Sciences Research Council).

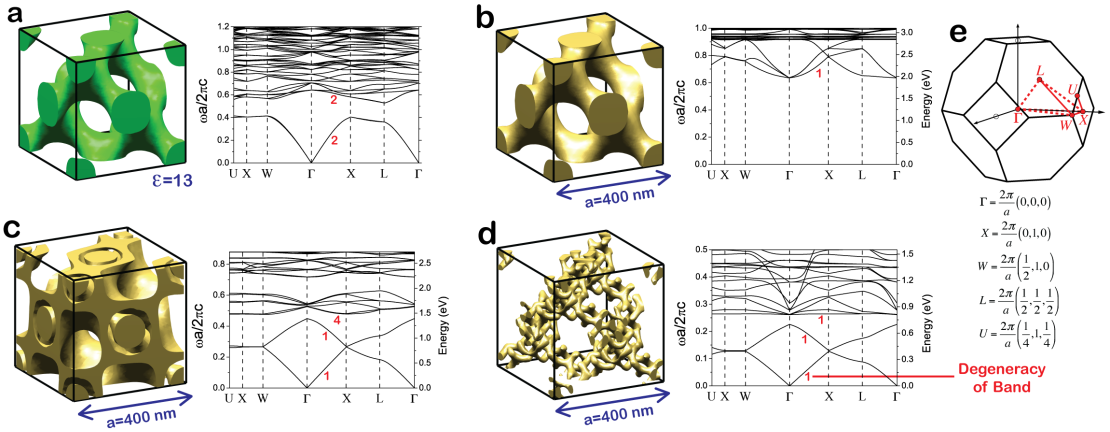

Figure 5.1. Photonic crystal (**a**) and metamaterials (**b-d**) with 3-dimensionally continuous diamond cubic structure, space group Q^{227} ($Fd\overline{3}m$), varying substructure of metamaterials and their photonic band structures: **a**, a photonic crystal with $\varepsilon = 13.0$ for green parts and $\varepsilon = 1.0$ for the rest; **b**, a metamaterial with no internal substructure; **c**, a metal/insulator/metal coaxial substructure; **d**, double gyroid substructure. The first Brillouin zone boundaries are shown in **e**. Degeneracies of low frequency bands are indicated with red numbers.

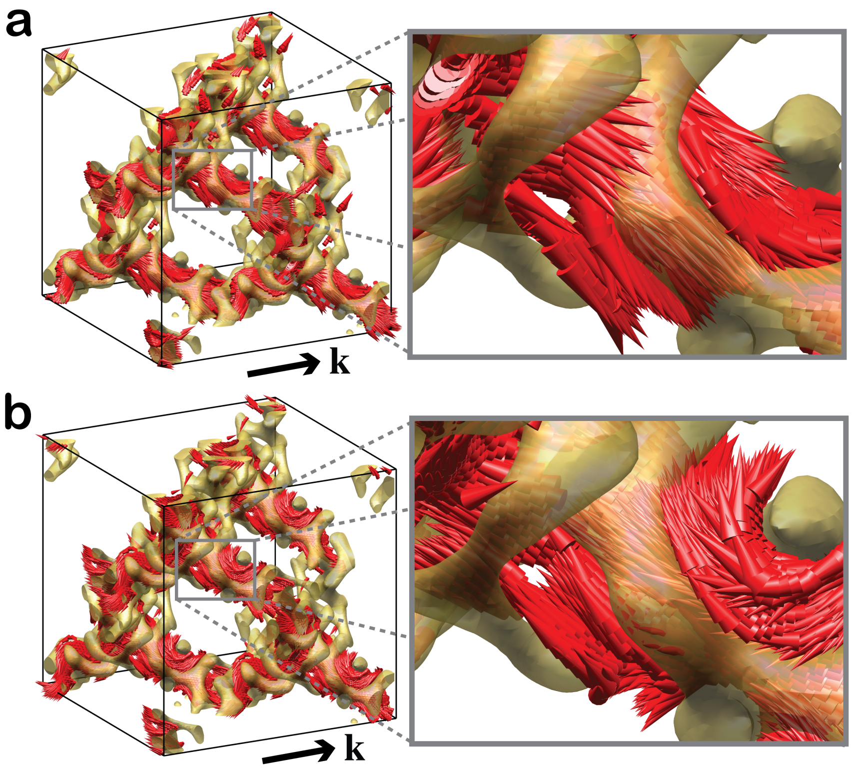

Figure 5.2. Energy flux of **a**, positive (at $\omega a/2\pi c=0.013$) and **b**, negative (at $\omega a/2\pi c=0.22$) refraction bands for the diamond cubic metamaterial with double gyroid substructures. ***k*** represents the momentum vector.

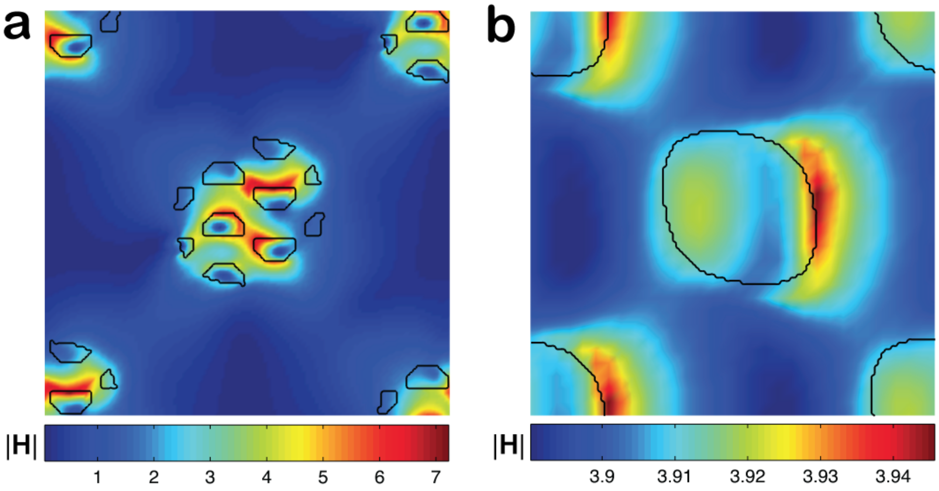

Figure 5.3. At *z=0* magnetic field distributions of the acoustic band in the metamaterial shown in Fig. 5.1d at *ωa/2πc=0.013* (**a**) and the photonic crystal shown in Fig. 5.1a at *ωa/2πc=0.093* (**b**) show distinct field strength differences. The metamaterial exhibits more concentrated magnetic fields near metallic surfaces as compared to the photonic crystal.

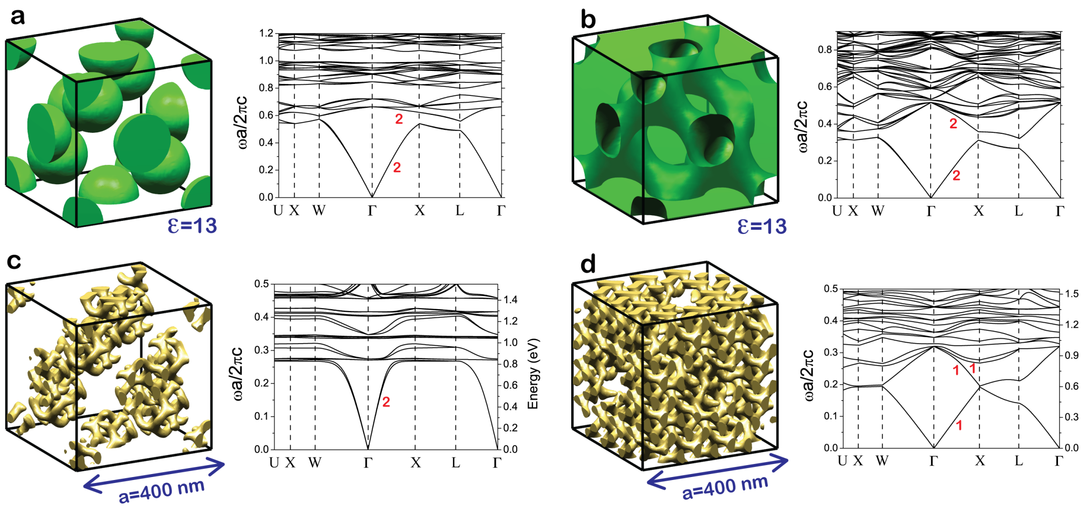

Figure 5.4. Photonic band structures of diamond cubic photonic crystals with *ε =13.0* for green parts and *ε=1.0* for the rest (**a**,**b**) and hierarchical diamond cubic metamaterials with double gyroid substructure (**c**,**d**). The larger scale superstructures are **a**,**c** discontinuous cubic and **b**,**d** continuous majority cubic structures. The acoustic bands of the photonic crystals and the disconnected metamaterial are doubly degenerate in **a-c** but not degenerate in **d** (degeneracies of low frequency bands are indicated with red numbers). The first Brillouin zone boundaries are same as in Fig. 5.1. Therefore discontinuous metamaterials are expected to exhibit similar photonic behavior as photonic crystals since they have degenerate acoustic bands and thus photons are energy carriers in the materials.

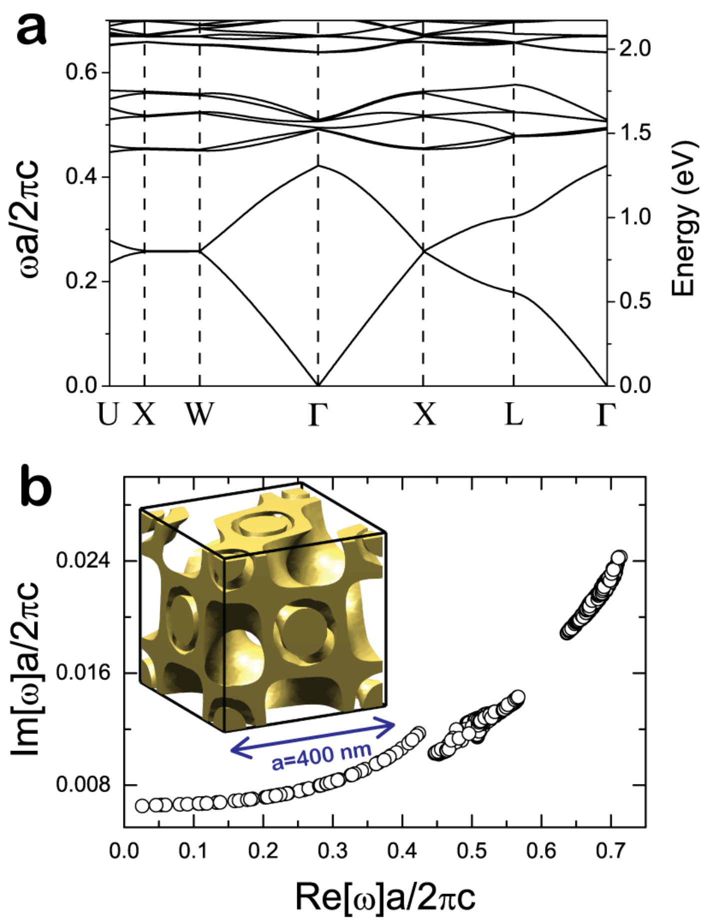

Figure 5.5. a, The photonic band structure of the diamond cubic metamaterial with a coaxial geometry for gold (the same structure as show in Fig. 5.1c) exhibits similar band structure to the Drude metal case. The frequencies of photonic bands shift to lower frequencies compared with the Drude metal case. **b**, Losses, Im[ω], are shown for different frequencies.

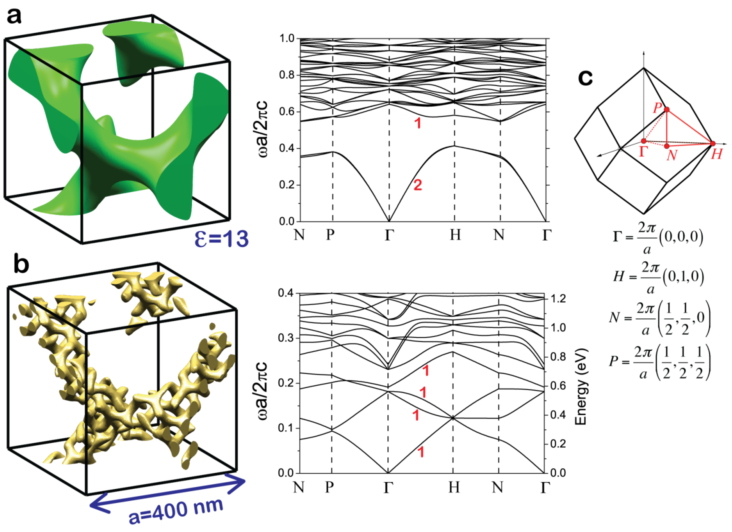

Figure 5.6. Photonic band structures of a photonic crystal (**a**) and a hierarchical metamaterial (**b**) with alternating gyroid, space group Q^{214} ($I4_132$), of which first Brillouin zone boundaries are shown in **c**. The hierarchical alternating gyroid metamaterial has double gyroid substructure. Degeneracies of low frequency bands are indicated with red numbers. While the alternating gyroid photonic crystal has a complete band gap, the metamaterial counterpart has no complete band gaps.

APPENDIX C

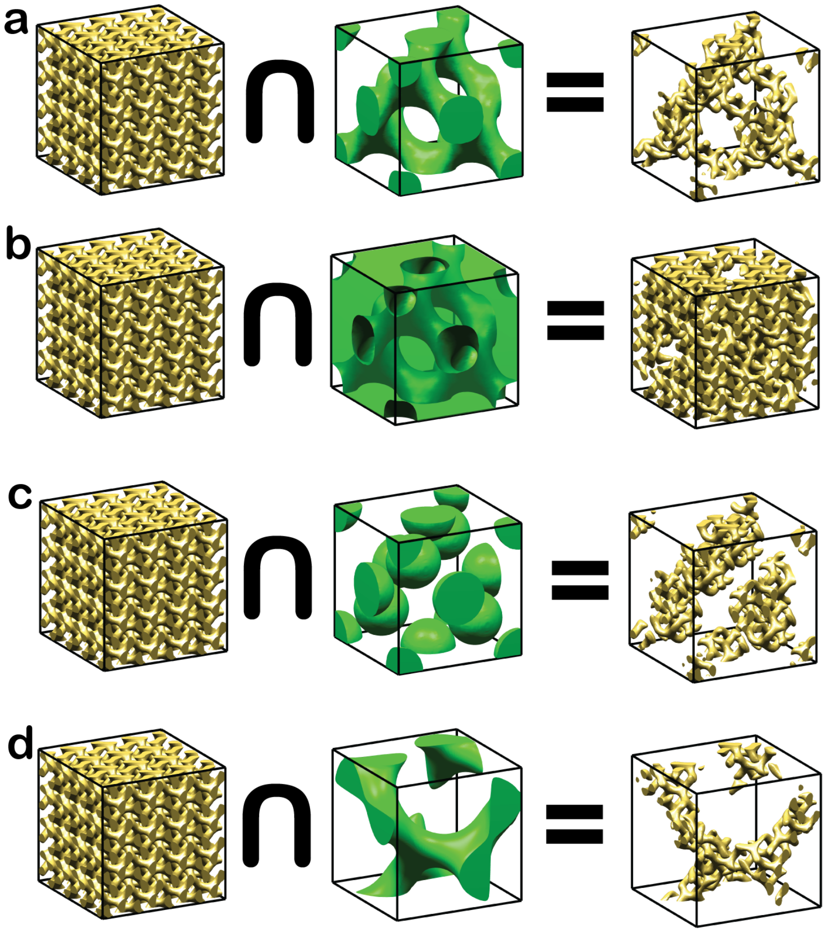

Figure S1. Schematics of building a simulated hierarchical structure: **a**, the continuous minority diamond cubic; **b**, the continuous majority diamond cubic; **c**, the discontinuous diamond cubic and **d**, the alternating gyroid structures. The meet of a 4x4x4 double gyroid super cell (left column) and a larger scale structure (middle column) forms a hierarchical structure (right column).

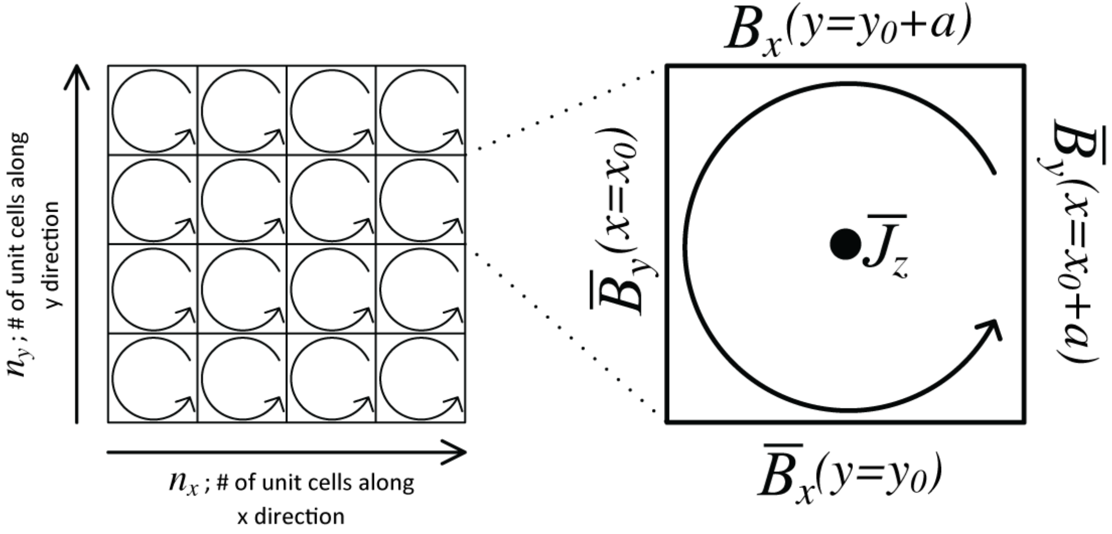

Figure S2. Schematic of magnetic fields and electric currents in metamaterials system for representing the Ampere's law in a discrete representation.

Structure building

The continuous diamond cubic structure ($Fd\overline{3}m$) was obtained by a level set function [26],

$$\begin{aligned} F(x,y,z) = \; & \cos(2\pi x/a+\pi/4)\cos(2\pi y/a+\pi/4)\cos(2\pi z/a+\pi/4)+ \\ & \sin(2\pi x/a+\pi/4)\cos(2\pi y/a+\pi/4)\cos(2\pi z/a+\pi/4)+ \\ & \cos(2\pi x/a+\pi/4)\sin(2\pi y/a+\pi/4)\cos(2\pi z/a+\pi/4)+ \\ & \cos(2\pi x/a+\pi/4)\cos(2\pi y/a+\pi/4)\sin(2\pi z/a+\pi/4) \end{aligned} .$$

For example, the regime, $F(x,y,z) \geq 0.5$, yields a minority continuous network shown in Fig. 5.1a and b with the volume fraction 0.30. For the coaxial geometry shown in Fig. 5.1c, the regime, $-0.1 \leq F(x,y,z) \leq 0.5$ and $F(x,y,z) \geq 0.9$, was chosen yielding the volume fraction 0.37. For the large-scale alternating gyroid structure with 128x128x128 grid points shown in Fig. 5.6 and the double gyroid substructure with 32x32x32, self-consistent field theory (SCFT) was utilized with the same simulation parameters used in our previous work [21]. The double gyroid unit cell obtained by SCFT was repeatedly placed along three directions for making a super cell with 4x4x4 double gyroid unit cells (see Fig. S1). The super cell was further structured with larger geometries as shown in Fig. S1: the continuous minority diamond cubic, the continuous majority diamond cubic, the discontinuous diamond cubic and the alternating gyroid structures (Fig. S1a).

Electric current conservation in a materials system

The metallic band gap of 3D continuous metamaterials in the low frequency regime originates from the requirement of electric current conservation. The proof is straightforward using Ampere's law [14],

$$\oint_{\partial S} \mathbf{B} \cdot d\mathbf{l} = \mu_0 \iint_{S} \left(\mathbf{J} + \varepsilon_0 \frac{\partial \mathbf{E}}{\partial t} \right) \cdot d\mathbf{A} \,,$$

where **B** is magnetic field, **E** electric field and **J** electric current flux through a surface, S. In a discrete case shown in Fig. S2 the equation can be approximated as

$$\oint_{\partial S} \mathbf{B} \cdot d\mathbf{l} \approx a n_x \left(\overline{B}_x^{y=y_0} + \overline{B}_x^{y=y_0+a} \right) + a n_y \left(\overline{B}_y^{x=x_0} + \overline{B}_y^{x=x_0+a} \right)$$

and

$$\mu_0 \iint_S \left(\mathbf{J} + \varepsilon_0 \frac{\partial \mathbf{E}}{\partial t} \right) \cdot d\mathbf{A} \approx a^2 n_x n_y \mu_0 \left(\overline{J}_z + \varepsilon_0 \dot{\overline{E}}_z \right),$$

where the bars represent spatially averaged fields and a, n_x and n_y are lattice dimension, the number of unit cells along x direction and the number of unit cells along y direction respectively. For materials system, n_x and n_y go to infinity and the equality,

$$\lim_{n_x, n_y \to \infty} \left\{ a n_x \left(\overline{B}_x^{y=y_0} + \overline{B}_x^{y=y_0+a} \right) + a n_y \left(\overline{B}_y^{x=x_0} + \overline{B}_y^{x=x_0+a} \right) \right\} \approx \lim_{n_x, n_y \to \infty} a^2 n_x n_y \mu_0 \left(\overline{J}_z + \varepsilon_0 \dot{\overline{E}}_z \right),$$

requires both sides of the equation to be zero since the right hand side of the equation grows more rapidly than the left hand side. At the low frequency regime, much smaller than plasma frequency $\omega << \omega_p$, the right hand side of the equation cannot be zero because

$$\varepsilon_0 \dot{\overline{E}}_z \propto -\frac{\omega^2}{\omega_p^2} \overline{J}_z$$

for Drude metals. Otherwise, if any electric currents, i.e. plasmons, across the surface S exist, the magnetic field strength needs to be infinite and unphysical. However, if there exists a counter electric current that compensates the other electric current, the overall current can become zero. Thus only coupled plasmon resonances conserving electric currents appear at low frequencies. For 3D continuous single network metamaterials, such coupled plasmon resonances are not possible and a metallic band gap is expected where no active photonic bands exist.

REFERENCES

[1] J. B. Pendry, Negative Refraction Makes a Perfect Lens. *Physical Review Letters* **85** (18), 3966 (2000).

[2] N. I. Zheludev, The Road Ahead for Metamaterials. *Science* **328** (5978), 582-583 (2010).

[3] M. A. Noginov, G. Zhu, A. M. Belgrave, R. Bakker, V. M. Shalaev, E. E. Narimanov, S. Stout, E. Herz, T. Suteewong, U. Wiesner, Demonstration of a spaser-based nanolaser. *Nature* **460** (7259), 1110-1112 (2009).

[4] M. I. Stockman, The spaser as a nanoscale quantum generator and ultrafast amplifier. *Journal of Optics* **12** (2), 024004 (2010).

[5] L. Novotny, B. Hecht, *Principles of nano-optics*. (Cambridge University Press, Cambridge, 2006).

[6] H. A. Atwater, A. Polman, Plasmonics for improved photovoltaic devices. *Nat Mater* **9** (3), 205-213 (2010).

[7] D. P. O'Neal, L. R. Hirsch, N. J. Halas, J. D. Payne, J. L. West, Photo-thermal tumor ablation in mice using near infrared-absorbing nanoparticles. *Cancer Letters* **209** (2), 171-176 (2004).

[8] D. R. Smith, J. B. Pendry, M. C. K. Wiltshire, Metamaterials and Negative Refractive Index. *Science* **305** (5685), 788-792 (August 6, 2004, 2004).

[9] J. D. Joannopoulos, *Photonic crystals : molding the flow of light*. (Princeton University Press, Princeton, ed. 2nd, 2008), pp. xiv, 286 p.

[10] M. Maldovan, C. K. Ullal, W. C. Carter, E. L. Thomas, Exploring for 3D photonic bandgap structures in the 11 f.c.c. space groups. *Nat Mater* **2** (10), 664-667 (2003).

[11] R. A. Shelby, D. R. Smith, S. Schultz, Experimental Verification of a Negative Index of Refraction. *Science* **292** (5514), 77-79 (April 6, 2001, 2001).

[12] N. W. Ashcroft, N. D. Mermin, *Solid state physics*. (Holt, New York,, 1976), pp. xxi, 826 p.

[13] S. Johnson, J. Joannopoulos, Block-iterative frequency-domain methods for Maxwell's equations in a planewave basis. *Opt. Express* **8** (3), 173-190 (2001).

[14] J. D. Jackson, *Classical electrodynamics*. (Wiley, New York, ed. 3rd, 1999), pp. xxi, 808 p.

[15] R. B. Lehoucq, D. C. Sorensen, C. Yang, *Arpack Users Guide: Solution of Large Scale Eigenvalue Problems by Implicitly Restarted Arnoldi Methods*. (SIAM, Philadelphia, PA, 1998).

[16] P. B. Johnson, R. W. Christy, Optical Constants of the Noble Metals. *Physical Review B* **6** (12), 4370 (1972).

[17] M. Maldovan, A. M. Urbas, N. Yufa, W. C. Carter, E. L. Thomas, Photonic properties of bicontinuous cubic microphases. *Physical Review B* **65** (16), 165123 (2002).

[18] T. H. Epps, E. W. Cochran, T. S. Bailey, R. S. Waletzko, C. M. Hardy, F. S. Bates, Ordered Network Phases in Linear Poly(isoprene-b-styrene-b-ethylene oxide) Triblock Copolymers. *Macromolecules* **37** (22), 8325-8341 (2004).

[19] A. H. Schoen, *Infinite periodic minimal surfaces without self-intersections*. (National Aeronautics and Space Administration; [for sale by the Clearinghouse for Federal Scientific and Technical Information, Springfield, Va.], Washington, 1970).

[20] V. Astratov, V. Bogomolov, A. Kaplyanskii, A. Prokofiev, L. Samoilovich, S. Samoilovich, Y. Vlasov, Optical spectroscopy of opal matrices with CdS embedded in its pores: Quantum confinement and photonic band gap effects. *Il Nuovo Cimento D* **17** (11), 1349-1354 (1995).

[21] K. Hur, Y. Francescato, V. Giannini, S. A. Maier, R. G. Hennig, U. Wiesner, Three-Dimensionally Isotropic Negative Refractive Index Materials from Block Copolymer Self-Assembled Chiral Gyroid Networks. *Angewandte Chemie International Edition* **50** (50), 11985-11989 (2011).

[22] S. Vignolini, N. A. Yufa, P. S. Cunha, S. Guldin, I. Rushkin, M. Stefik, K. Hur, U. Wiesner, J. J. Baumberg, U. Steiner, A 3D Optical Metamaterial Made by Self-Assembly. *Advanced Materials* **24** (10), OP23-OP27 (2012).

[23] S. C. Kitson, W. L. Barnes, J. R. Sambles, Full Photonic Band Gap for Surface Modes in the Visible. *Physical Review Letters* **77** (13), 2670-2673 (1996).

[24] B. Luk'yanchuk, N. I. Zheludev, S. A. Maier, N. J. Halas, P. Nordlander, H. Giessen, C. T. Chong, The Fano resonance in plasmonic nanostructures and metamaterials. *Nat Mater* **9** (9), 707-715 (2010).

[25] S. A. Maier, *Plasmonics : fundamentals and applications*. (Springer, New York, ed. 1st, 2007), pp. xxiv, 223 p.

[26] M. Wohlgemuth, N. Yufa, J. Hoffman, E. L. Thomas, Triply Periodic Bicontinuous Cubic Microdomain Morphologies by Symmetries. *Macromolecules* **34** (17), 6083-6089 (2001/08/01, 2001).